



Universiteit
Leiden
The Netherlands

The origins of friction and the growth of graphene, investigated at the atomic scale

Baarle, D.W. van

Citation

Baarle, D. W. van. (2016, November 29). *The origins of friction and the growth of graphene, investigated at the atomic scale. Casimir PhD Series*. Retrieved from <https://hdl.handle.net/1887/44539>

Version: Not Applicable (or Unknown)

License: [Licence agreement concerning inclusion of doctoral thesis in the Institutional Repository of the University of Leiden](#)

Downloaded from: <https://hdl.handle.net/1887/44539>

Note: To cite this publication please use the final published version (if applicable).

Cover Page



Universiteit Leiden



The handle <http://hdl.handle.net/1887/44539> holds various files of this Leiden University dissertation.

Author: Baarle, D.W. van

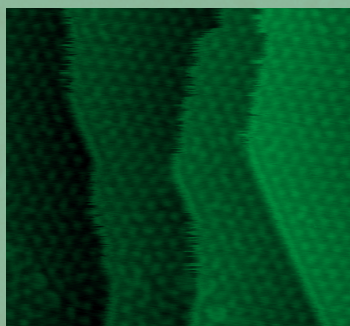
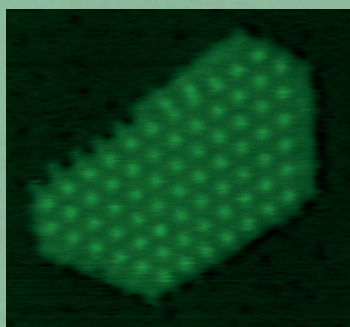
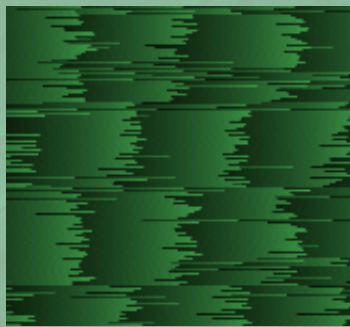
Title: The origins of friction and the growth of graphene, investigated at the atomic scale

Issue Date: 2016-11-29

The origins of friction and the growth of graphene

investigated at the
atomic scale

Dirk W. van Baarle



The origins of friction and the
growth of graphene
investigated at the atomic scale

The origins of friction and the growth of graphene

investigated at the atomic scale

Proefschrift

ter verkrijging van
de graad van Doctor aan de Universiteit Leiden,
op gezag van Rector Magnificus prof. mr. C. J. J. M. Stolker,
volgens besluit van het College voor Promoties
te verdedigen op dinsdag 29 november 2016
klokke 11.15 uur

door

Dirk Willem van Baarle
geboren te Ridderkerk
in 1986

Promotor:

Prof. dr. J. W. M. Frenken
Universiteit Leiden

Leden van de promotiecommissie:

Prof. dr. A. Fasolino
Radboud Universiteit, Nijmegen, Nederland

Prof. dr. T. Michely
Universität zu Köln, Keulen, Duitsland

Prof. dr. E. R. Eliel
Universiteit Leiden

Prof. dr. ir. T. H. Oosterkamp
Universiteit Leiden

ISBN: 978-90-8593-277-2 Casimir PhD series, Delft-Leiden 2016-33
An electronic version of this thesis can be found at <https://openaccess.leidenuniv.nl>

The work presented in this thesis has been performed at the Huygens-Kamerlingh Onnes Laboratory, Leiden Institute of Physics, Leiden University, The Netherlands, and has been financially supported by the European Research Council (ERC) through the Advanced Grant project Science F(r)iction, SciFri, and by the Foundation for Fundamental Research on Matter (FOM) in the framework of the FOM-Program on Fundamental Aspects of Friction, FaF.

General introduction and outline

Two research fields meet

A single glance at the title of this thesis might give rise to questions on the focus and scope of the work reported here. Is this thesis a mere aggregation of two separate studies? What is the relation between research on the origin of friction and on the growth of graphene? Why is a theoretical study combined with experimental work?

The key to the answer to these questions can be found in previously reported work that was performed by Dienwiebel *et al.*[1]. In that work, it was discovered that the incommensurability between rotated graphite layers results in ultralow friction, also known as superlubricity. This effect of ultralow friction, measured at the nanometer scale, invites us to investigate the friction of a nanocontact: which parameters are essential to capture an atomic-scale contact in a simple model? Can we describe, understand and predict the behaviour of friction contacts, based on this model?

The results of Dienwiebel *et al.* invite us to think about a scaled-up version: is it possible to reproduce the low-friction behaviour between rotated layers of graphite at the macroscopic scale?

To perform such a macroscopic low-friction experiment, a first requirement is the availability of surfaces that are characterized by atomically flat and defect-free, macroscopic-sized single crystals of graphite or graphene. Can we realize such surfaces? Are there atomic-scale processes that can assist in the synthesis of perfect, macroscopic-sized graphene-covered surfaces?

Part I: On the origins of friction

The research reported in this thesis deals with the two types of questions outlined above. First, we present our studies into the origins of friction. Our approach is to focus on the dissipation of a single-asperity friction contact.

After an introduction of the subject and a brief overview of the current status of the research field on single-asperity friction in the first chapter, we present a bottom-up estimate of the dissipation of a frictional nanocontact in Chapter 2. The result shows that there is a significant discrepancy between our estimate and the typical values assumed in the literature. In order to solve this discrepancy, we present a more physical, but still rather simple method to describe a single asperity.

In Chapter 3, the numerical method to simulate and evaluate our new description of single-asperity friction is presented.

Chapter 4 contains the results of our computations. These results are discussed and compared with experimental results from the literature. This study brings us to a more fundamental understanding of a friction nanocontact. Additionally, it casts new light on the behaviour of sliding surfaces and invites us to speculate about new ways to control friction by manipulation of the contact geometry.

Part II: Graphene growth on Ir(111)

The second part of this thesis is dedicated to the experimental work performed on the graphene-iridium system. Using our high- and variable-temperature STM we studied the behaviour of graphene at nucleation and growth conditions on the Ir(111) surface.

In Chapter 5, the recent literature is discussed and the most relevant aspects of the experimental setup are described in combination with some methods used in our work.

Chapters 6-8 are dedicated to the results of the experiments, focussing on the nucleation, growth and ripening of graphene on Ir(111). Chapters 9 and 10 present some findings on the closure of a graphene film and on the high-temperature impact of iridium steps on the graphene overlayer.

Contents

I	On the origins of friction	11
1	Introduction and motivation	12
1.1	Hunting for the fundamentals of friction	12
1.2	The Friction Force Microscope	13
1.3	The theoretical model	16
1.4	A first look at 2-mass-2-spring behaviour	19
2	The dissipation of a single-asperity contact: a problematic discrepancy	21
2.1	Background	21
2.2	The friction force on a single atom	22
2.3	The dissipative force on a single asperity	22
2.4	Finding the origin of the discrepancy	24
2.5	Estimating the dynamic mass	25
2.6	Summary	28
3	The refined 2-mass-2-spring model	29
3.1	Introduction	29
3.2	From schematics to Langevin equations	29
3.3	The 2-mass-2-spring model in full detail	31
3.4	Computational architecture	33
3.5	Time-step calculation, thermal-noise generation and data averaging	35
3.6	Summary	37
4	Computational results, their interpretation and implications	38
4.1	Results - a limited regime of atomic resolution	38
4.2	Interpretation - modes of friction	41
4.3	Implications - tuneable friction	42

4.4	A detailed look at FFM experiments and their interpretation	43
4.5	Summarizing conclusions	57
Appendices		58
A	Theoretical description of the Q-factor of the cantilever	58
B	List of symbols	62
II	Graphene growth on Ir(111)	64
5	Introduction, instrumentation and methods	65
5.1	A short introduction to graphene	65
5.2	Instrumentation	68
5.3	Methods	71
6	Graphene nucleation on Ir(111)	77
6.1	Experimental approach	77
6.2	Deposition of ethylene at room temperature	78
6.3	First observation of carbon clusters	80
6.4	Conversion from hydrocarbons to amorphous carbon	82
6.5	Lowest temperature of graphene nucleation	86
6.6	Summarizing conclusions	95
7	Graphene growth	96
7.1	Experimental observation of graphene island evolution	96
7.2	A geometrical interpretation	99
7.3	Conclusions	101
8	Graphene ripening: Ostwald beats Smoluchowski	103
8.1	The live observation of graphene ripening by STM	103
8.2	Discussion	107
8.3	Summary and conclusions	111
9	Graphene film closure: strain and boundary defects	112
9.1	Observation of graphene film closure	112
9.2	Graphene domains locally align by strain	115
9.3	Conclusions	118

10 High-temperature behaviour of graphene-covered iridium	119
10.1 Graphene growth over iridium steps	119
10.2 Iridium step mobility underneath graphene	123
10.3 Fluctuations of graphene-covered iridium steps	126
10.4 Summary	133
Appendices	135
C Image-subtraction procedure	135
D Island-extraction algorithm	138
Bibliography	139
Summary	149
Samenvatting	153
Acknowledgements	158
Curriculum vitae	160

Part I

On the origins of friction

Chapter 1

Introduction and motivation

1.1 Hunting for the fundamentals of friction

1.1.1 A historical note

Friction is an everyday life phenomenon. The first research on friction was performed in the 15th century by Leonardo Da Vinci, resulting in the first friction laws. Da Vinci's unpublished findings have been repeated independently in the 18th century by Amontons and Coulomb[2]. The resulting Amontons-Coulomb law states that the kinetic friction force between two sliding macroscopic objects is given by

$$F = \mu N \tag{1.1}$$

with N being the normal load, i.e. the force with which the two bodies are pressed against each other, and μ the macroscopic friction coefficient. One of the most remarkable aspects of this relation is the absence of both the real or apparent contact area (see Figure 1.1) and the relative velocity between the two sliding objects. The absence of the apparent contact area in Equation 1.1 can be explained by focussing on the real contact between the two bodies. As illustrated in Figure 1.1, the real contact is formed by the ensemble of asperities on the two surfaces that mechanically touch the opposite surface[3]. Plastic and elastic deformations of the asperities under the applied normal load lead to a total contact area that is more or less proportional to that load. If we assume that the friction force, i.e. the lateral force required to make the interface slip, is proportional to the real area of contact, the proportionality between the normal force and the real contact area makes the friction force directly proportional to the loading force, in accordance with Equation 1.1.

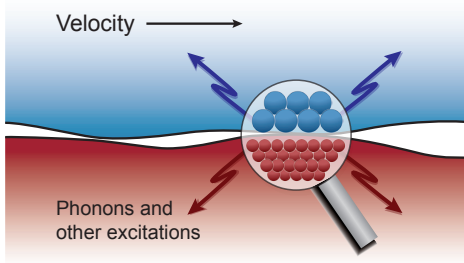


Figure 1.1: Schematic view of the interface between two macroscopic bodies. On the microscale, only a small fraction of the apparent contact area is in genuine, mechanical contact. This real contact area is established by a large number of microscopic asperities.

1.1.2 Experimental studies of a single asperity

When one realizes that a friction contact is formed by an ensemble of small asperities, it is straightforward to study the properties of one single asperity in order to research the origins of friction. The invention of the Atomic Force Microscope (AFM) has resulted in a tool that allows one to study friction at the atomic scale using its tip as a single-asperity contact[4]. This has resulted in the development of a special type of AFM, tailored to investigate atomic-scale friction, known as the Friction Force Microscope (FFM) or Lateral Force Microscope (LFM). A two-dimensionally sensitive LFM has been constructed by our research group[5]. As the experimental data of the FFM was used intensively in our work, this instrument will be discussed here briefly.

1.2 The Friction Force Microscope

The FFM is based on the AFM and typically consists of a cantilever with an almost atomically sharp tip, see Figure 1.2a. This tip is brought into contact with a clean substrate. Under a constant normal load of typically some nN, the tip is scanned over the surface using an XY-piezo stage. This scanning motion forces the tip to bend laterally, until the force built up in the cantilever is sufficient to make the tip slide over the surface. In most FFM instruments, the deflection of the cantilever is probed using a laser which is pointed at and reflected by the cantilever. The deflection is derived from the shift of the reflected light spot on a split photodiode. By using a four-quadrant photodiode, the normal and lateral forces can be followed simultaneously.

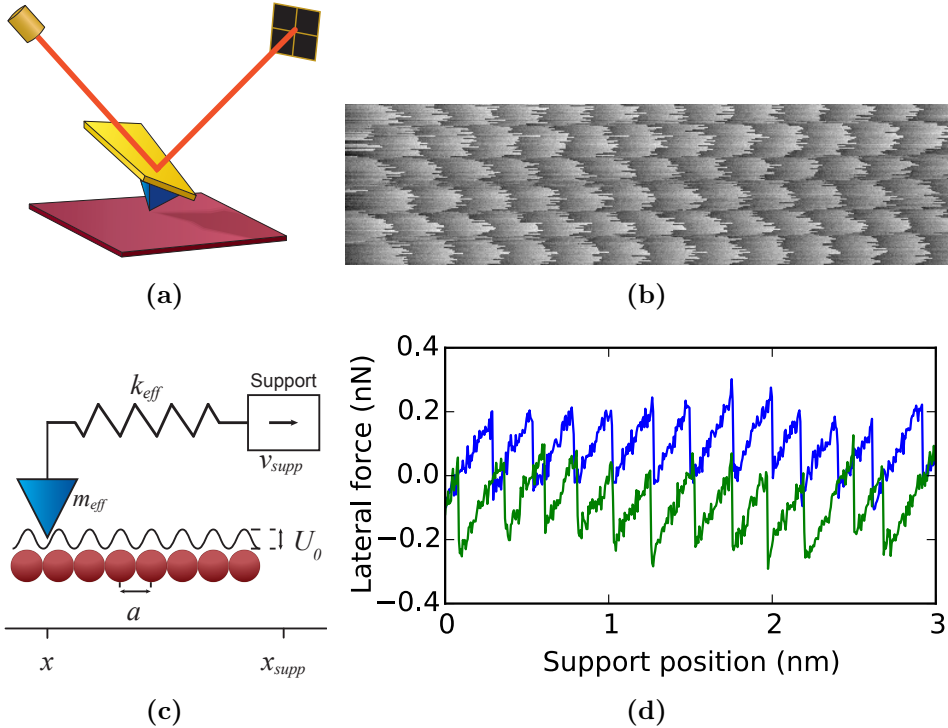


Figure 1.2: (a) Schematic view of a FFM setup. An atomically sharp tip at the end of a cantilever is pulled over a substrate. The relevant forces are obtained via the cantilever deflection which is measured using a laser and a position-sensitive photodiode. (b) Typical lateral force map ($3 \times 0.8 \text{ nm}^2$), obtained by friction force microscopy[6]. In each line, the silicon-tip moves from left to right over the substrate (in this case HOPG). The gray scale indicates the strength of the opposing lateral force. (c) Schematic view of the FFM experiment; a rigid support (white rectangle) is moving at constant velocity and drags the tip (blue triangle) via a spring over the atomically corrugated substrate (red spheres). The extension of the spring is a direct measure of the lateral force experienced by the tip. (d) Lateral force variation during an individual sweep of the tip from left to right (blue curve; center line in panel (b)) and from right to left (green). Panels (b) and (d): data courtesy of Prof. A. Schirmeisen, Justus-Liebig University, Giessen, Germany

The lateral force data recorded during the scan of the tip over the substrate surface can be plotted as function of the support position, set by the piezo-scanner. Hence, a 2D-image can be constructed easily. This procedure is well established and a typical result of such a measurement is shown in Figure 1.2b. The data in this image was provided by A. Schirmeisen[6].

1.2.1 Stick-slip motion

One feature that is typical for high-quality FFM experiments and that is clearly visible in Figure 1.2b, is a periodic saw-tooth-like variation in the lateral force. In a two-dimensional lateral force map, a lattice emerges that perfectly matches the atomic periodicity of the substrate. A single combination of a forward trace (blue), with the tip running from left to right, and a backward, right-to-left trace (green) of this image is presented in Figure 1.2d. The sawtooth character of these traces is formed by the combination of straight sections in which the lateral force builds up linearly, separated by sections where the lateral force drops abruptly. The sections where the lateral force builds up are associated with configurations in which the tip is effectively stuck in an energy minimum on the corrugated substrate. When the lateral force reaches a threshold value, the tip slips over an energy maximum and ends up in the next energy minimum, one atomic distance further along the substrate. This is why this typical sawtooth-like behaviour is called ‘stick-slip motion’.

1.2.2 Modelling a single asperity

Over the years, several theoretical approaches have been constructed to address friction mechanisms. These are ranging from rather simple, mechanical models to more sophisticated concepts, involving phonons[7] or even quantum effects[8]. In spite of all the modelling efforts invested, we are still very remote from having full predictive power with respect to energy dissipation rates and friction coefficients.

The simplest mechanical model, which is extremely popular in the field of nanotribology, is the Prandtl-Tomlinson (PT) model. It is an almost fully deterministic description of a friction contact using a Langevin-type equation of motion[9, 10]. This model appears to be very successful in reproducing experimental data, see e.g. References [6, 11, 12].

1.3 The theoretical model

The core of the PT model is the mass-spring system, as shown in Figure 1.2c. It basically consists of an effective mass, m_{eff} , which is pulled through a corrugated, periodic substrate potential V_{subs} with amplitude U_0 . The effective mass is connected to the scanning support via a spring with an effective spring coefficient k_{eff} . In combination, the periodic lattice and the spring result in a total potential with the shape of a corrugated parabola. When the lattice corrugation is sufficiently large, local wells are present in the potential. The model assumes an instantaneous dissipation of the kinetic energy the tip acquires, which results in the tip to be always in one of the (local) minima present. While the support is moving, the spring potential (the parabola) shifts along the corrugated lattice. This results in an emergence and disappearance of the local minima in the corrugated parabola. As soon as the barrier between two local minima has vanished and the tip is in one of these minima, the system is mechanically instable and the tip slips to the next minimum. The observed stick-slip behaviour as shown in Figure 1.2d is characteristic for this fully deterministic model.

The PT model assumes a instantaneous dissipation of energy. In order to make the description of a single asperity contact more mature, a term containing a characteristic energy dissipation rate can be introduced in the model. This would allow us to study the physical dissipation mechanism, which is typically assumed to be linearly dependent on the velocity of the object executing the stick-slip motion. Automatically, the introduction of a dissipative element will add a noise term related to the exchange of energy of the tip with the substrate.

After the introduction of these two dynamic terms, the system can now be described mathematically by the following Langevin equation:

$$m_{\text{eff}}\ddot{x}_t = -\left.\frac{\partial V_{\text{subs}}(x, y)}{\partial x}\right|_{(x, y)=(x_t, y_t)} - k_{\text{eff}}(x_t - x_{\text{support}}) + \xi - \gamma\dot{x}_t \quad (1.2)$$

where x_t is the position of the tip. This force-equation expresses the acceleration of the tip as function of four elements: (1) the force of the substrate potential on the tip apex, (2) the effect of the effective spring between tip and support, (3) ξ : the thermal noise on the tip and finally (4) the dissipative element causing the loss of energy that results in the friction force. The reader should note that the values of the dissipation rate γ and the amplitude of the noise term ξ are connected to each other via the fluctuation-dissipation theorem[13]. Further details of the elements 1, 2 and 4 are described in detail in Section 3.3.

As noted earlier, the Langevin model just described can reproduce the observed lateral force traces. This invites us to translate the variables used in the model into physical elements that are present in the experimental setup. During the construction of this translation, it is important to compare both schematics in Figure 1.2.

First we focus on the most important variable: x_t : it is the position of the entity which we denote as the tip. According to Eq. 1.2 the tip makes contact with the substrate and at the other hand, the friction force is calculated by $-k_{\text{eff}}(x_t - x_{\text{support}})$. Translating to the experiment, the measured friction force, which is deduced from the cantilever spring deflection, is directly related to the position of the tip and hence the tip position can be estimated experimentally.

The effective mass m_{eff} refers not only to the tip atoms that are in direct contact with the substrate, but comprises also the other atoms that are moving together with the tip, which is usually thought to also include a significant fraction of the (much heavier) cantilever.

Another important ingredient is k_{eff} : the effective spring coefficient. A pragmatic, experimental way to determine the effective spring coefficient is by using the stick-slip motion measured by the FFM, as shown in Figure 1.2d. The slope of the lateral force curve during each stick-phase is a direct estimate of the effective spring in the experiment. Typical values found experimentally are around 2 N/m. These values are significantly lower than the lateral/torsional spring coefficients of the cantilevers used (typically 10 – 200 N/m), indicating that another spring is active in series. There can be several origins of this extra, see Equation 1.3. First, the extra spring can be attributed to the tip, of which the final section is so narrow that it is more flexible than most cantilevers. For an ideally sharp tip, ending in an apex of just a few atoms, we may expect an effective spring coefficient in the order of that of a single interatomic bond, which is indeed in the order of 1 N/m.

A second factor that influences the effective spring coefficient is the tip-substrate interaction (TSI). This interaction results in a force that can be described via a spring coefficient k_{TSI} , which is dependent on many parameters, such as the precise tip apex position and the normal load[14].

A third additional component that affects the effective spring coefficient is the stiffness of the substrate itself, characterized by k_{subs} . As the substrate is a 3-dimensional body consisting of many atoms that are coupled together via atomic bonds, this body is rather stiff. This results in a spring coefficient k_{subs} that will be significantly larger than k_{tip} .

Summarizing, the experimentally observed effective spring coefficient

can be calculated via

$$k_{\text{eff}}^{-1} = k_{\text{cant}}^{-1} + k_{\text{tip}}^{-1} + k_{\text{TSI}}^{-1} + k_{\text{subs}}^{-1} \approx k_{\text{tip}}^{-1} + k_{\text{TSI}}^{-1}. \quad (1.3)$$

As explained above, k_{cant} and k_{subs} are usually significantly larger than k_{tip} , so their impact on the effective spring coefficient will be minimal. The tip-surface interaction can be manipulated in the experiment via the normal load. Relatively high normal loads make k_{TSI} high, which makes k_{eff} approximately equal to k_{tip} . This provides an excellent recipe to estimate the k_{tip} experimentally[14], which is the case we will deal with in the next chapters. Hence, in our work, we can assume that $k_{\text{eff}} \approx k_{\text{tip}}$.

1.3.1 Towards a 2-mass-2-spring model

The need to resort to an effective spring coefficient, described above, indicates that the simple description of the dynamics of a single mass, given by Equation 1.2, falls short of capturing the full dynamics that is at play. Instead of a single mass (tip + part of the cantilever) dragged through the potential energy landscape via a single spring (Figure 1.2c), we are dealing with two springs in series (cf. Equation 1.3) and, hence, also with two masses. One of them, to be associated with the tip, is necessarily small, while the other, associated with (a large part of) the cantilever, must be much larger. We should expect that the massive cantilever will not be able to follow the probably much more rapid dynamics of the tip. Since the force signal in FFM-measurements is obtained from the cantilever deformation, we should expect that much of the actual contact dynamics is not appropriately reflected in the recorded forces.

The need of a more refined description of a friction contact was realized a few years ago, leading to a small number of models with two or more springs. S. Maier et al. reported a nice combination of results from high frequency data sampling experiments with simulations using a two-mass-two-spring model[15]. Their results hint that highly time resolved research is crucial for further understanding the friction contact behaviour. Also the work of Abel et al. indicates that friction is a very dynamic phenomenon asking for attention to extremely rapid evolving processes[16].

In the following chapter, we will critically evaluate the common interpretation and simulations in order to identify a discrepancy which is inherent in most models reported so far. We will be forced to change our understanding of the contact dynamics and the mechanism of energy dissipation.

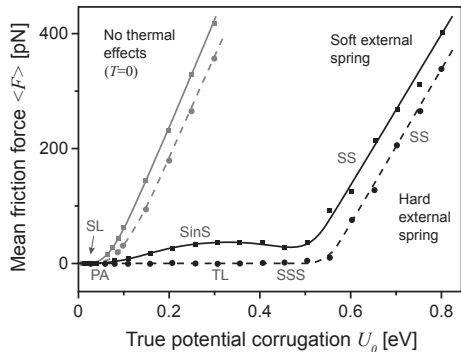


Figure 1.3: The calculated mean friction force as function of the corrugation potential, picture reprinted from [17]. Several friction regimes emerge, depending on the calculation parameters. The open symbols denote calculations without thermal effects ($T = 0$), the external spring is the cantilever spring. The stick-slip (SS), superlubric (SL) and thermolubric (TL) regimes are discussed in the text briefly. The other regimes present are stochastic stick-slip (SSS), stuck in slipperiness (SinS), slipping via an intermediate position (SIP) and ‘passive apex’ (PA). A detailed description of all the friction regimes is given in the original publication.

1.4 A first look at 2-mass-2-spring behaviour

Incorporating a second spring and a second mass into the description of a single-asperity friction contact, introduces a wealth of dynamic phenomena in the combined motion of the cantilever and the tip. This rich dynamics has been explored theoretically intensively, of which a comprehensive overview is present in Reference [17]. Depending on e.g. the lattice constant, the temperature, the masses of tip and cantilever and the two spring coefficients different friction behaviour is observed. A graphical overview of these friction regimes is presented in Figure 1.3, which is reproduced from Reference [17]. This figure shows a surprisingly large number of friction regimes, each indicated by one of the acronyms. Here we briefly mention the three most relevant ones.

Stick-slip (SS) Stick-slip motion is the motion introduced before, in which the tip is periodically trapped in a potential well and is forced to slip through the potential energy landscape, lattice spacing by lattice spacing. This type of motion occurs when the amplitude of the tip-substrate potential is sufficiently high with respect to the effective spring coefficient, when the temperature is sufficiently low, and when the dissipation rate at the

tip-substrate contact is sufficiently high. It is observed in a large fraction of FFM experiments.

Superlubricity (SL) When the amplitude of the tip substrate potential is lowered enough with respect to the effective spring coefficient, sliding proceeds without slip-instabilities and the friction force is reduced nearly to zero. This situation can be realized either by reducing the normal force between tip and substrate, typically requiring one to exert a negative normal force (to compensate part of the tip-substrate attraction)[14], or by shaping the contact in the form of an incommensurate interface between two crystalline lattices[1, 18]. The latter geometry is known under the name ‘superlubricity’[19].

Thermolubricity (TL) Another regime of extremely low friction arises when the corrugation of the tip-substrate interaction potential is sufficiently low with respect to the thermal energy that the tip overcomes the energy barriers between neighbouring energy minima frequently on the timescale of the support motion. This leads to a kind of biased diffusion of the tip with hardly any energy dissipation. This regime of thermally assisted motion has been introduced under the name ‘thermolubricity’[20].

Throughout the first part of this thesis, when needed, specific aspects of the friction regimes will be discussed and characterized in more detail.

1.4.1 Focus of this part of the thesis

The theoretical approaches listed here do reproduce experimental data quite often. However, they still contain subtle assumptions or hidden contradictions. This thesis will first elaborate on the conventional interpretation of FFM-data using the Prandtl-Tomlinson model. We will show that this interpretation hides a fundamental contradiction. Via an estimate of the order of magnitude of the dissipative forces required to produce atomic-scale patterns in the so-called stick-slip motion of a friction nano-contact, we find that the energy dissipation must be dominated by a very small, highly dynamic mass at the very end of the asperity. Based on these findings, a more physical, but still rather simple method to describe the single-asperity contact will be presented. The evaluation of this method casts new light on the behaviour of sliding surfaces and invites us to speculate about new ways to control friction by manipulation of the contact geometry.

Chapter 2

The dissipation of a single-asperity contact: a problematic discrepancy

2.1 Background

In the previous chapter, the PT-model was introduced. This classical model is very successful in capturing many features of atomic-scale friction experiments. However, as was already indicated, there are two ways in which this PT-model does injustice to the physics that is crucial for friction. First of all, dissipation is not instantaneous. It must be governed by a finite dissipation rate that reflects the actual mechanism by which the excess energy is removed from the accelerated slider. Secondly, according to the fluctuation-dissipation theorem, the dissipation couples the slider to the thermal bath of the dissipating medium and, hence, introduces thermal noise.

Introducing these two elements, finite dissipation and noise, leads to an alternative and somewhat more sophisticated version of the PT-model, in the form of the Langevin equation given in Equation 1.2. In this picture, the effective mass represents the tip plus a significant part of the cantilever, which can be viewed as moving together with the tip. It can be estimated easily on the basis of the cantilever dimensions or it can be taken from the readily measured eigenfrequency of the cantilever, in combination with the spring coefficient of the cantilever. The effective spring coefficient differs from the cantilever spring coefficient. It can be measured directly from the ‘stick’-part of a force-versus-displacement curve (cf. Figure 1.2d) and usually is dominated strongly by the flexibility of the tip apex, which acts as a soft spring. Typical values used for these parameters are an effective

mass in the order of 10^{-11} kg and an effective spring coefficient of 2 N/m.

The only free parameter left in Equation 1.2 is the dissipation rate γ , which is therefore used as a kind of fitting parameter in order to reproduce the experimentally observed data. The resulting value for γ is typically around 10^{-6} kg/sec[6, 11, 12, 21]. A more refined two-mass-two-spring model used by Maier [15] was applied using a similarly small ‘tip’-mass of 10^{-12} kg and a dissipation parameter tuned such that the stick-slip patterns were observed. The value for the small mass was varied by a factor 10 and yielded no observable differences in the calculations[15].

Even though the Langevin equation (Equation 1.2) and the related numerical descriptions of the atomic-scale sliding motion seem to reproduce experimental observations successfully, they do not lead to a physical understanding of the friction mechanism: what does the effective mass mean and how do we have to interpret the values of the dissipation rate obtained from the fitting procedures? Actually, as our studies aim to understand the friction parameter, we do not want to use it as a fitting parameter, but prefer to argue its origin and try to predict its value.

2.2 The friction force on a single atom

In order to provide a better basis for understanding the dissipation rate, we will construct a simple, bottom-up description of the dissipation that is easy to quantify. By first studying the friction of a single atom, the dissipation rate of a small friction contact composed out of several atoms can be established. We will use this approach as the quantitative basis for our model calculations.

To get an estimate of the typical time it takes for an atom in the friction contact to lose its excess energy, we resort to related subjects in the field of surface science. Especially both experimental and theoretical studies on atomic and molecular vibrations and studies on diffusion and jumps of atoms and small molecules on surfaces are helpful[22–25]. These show that the motion of atoms and molecules on surfaces is approximately critically damped: the time it takes to dissipate excess momentum is in the order of the natural vibration frequency of the atoms or molecules on the surface, which frequency is in the order of 10^{12} Hz.

2.3 The dissipative force on a single asperity

We now assume that the momentum dissipation rate of an atom, γ_{at} , present at an atomically sharp tip, in contact with a substrate, is of the

same order of magnitude as the dissipation rate of a single atom on a surface. In addition, we assume that, in case the tip apex is not atomically sharp, the total dissipation rate scales linearly with the number of atoms in the tip apex that make contact with the substrate, N_c . This second assumption might seem to be crude and one might argue a sublinear dependence would be more appropriate as the dissipation per atom might degrade when more than one atom is constituting the friction contact. However, as will become clear at the end of our study, the possible overestimation of the total dissipation rate will make our conclusions even stronger.

Finally, we assume that the basic dissipation form in Equation 1.2, in which the dissipative force is proportional to velocity, remains valid. The combination of these three assumptions should enable us to produce a coarse prediction of the friction force on a complete asperity given its contact size, which is what we will perform in the next section.

The above assumptions can be combined into the following equation for the friction force experienced by a tip that has N_c atoms in contact with the substrate and moves over the substrate at a velocity of \dot{x}_t :

$$F_{\text{diss}} = -\gamma_{\text{diss}}\dot{x}_t = -\gamma_{\text{at}}N_c\dot{x}_t \quad (2.1)$$

A subtle difference with typically used descriptions of the friction force, is the absence of the (effective) tip mass. The only (implicit) mass dependence is present in the factor $\gamma_{\text{at}}N_c$. One should note that in the approach presented here, we associate the actual dissipation entirely with the atoms that make up the frictional contact. It is their number and their velocity that count. The resulting dissipation force is independent of the mass of the rest of the tip, even if that moves at the same velocity as the contact atoms. Even though this may seem obvious, this approach is not followed generally.

Already at this stage, an estimate can be made of the dissipation rate γ_{diss} of a single asperity. In reports containing data from FFM-experiments, typically the size of the tip apex (the friction contact) is discussed[26–29]. In these experiments, point defects in the substrate lattice or step edges on crystal terrace were used to estimate the tip size. Typical sizes of the realized FFM friction contacts (N_c) vary from single-atom up to tens of atoms. For this moment, we will assume a contact size of 10 atoms. If tungsten is chosen to be the tip material, the characteristic lattice vibration frequencies are in the order of 10^{12} Hz. Taking these values, the momentum dissipation rate of the friction contact is in the order of 10^{-12} kg/sec.

The value estimated here for the dissipation rate that should be expected for a typical FFM friction contact is extremely much lower than

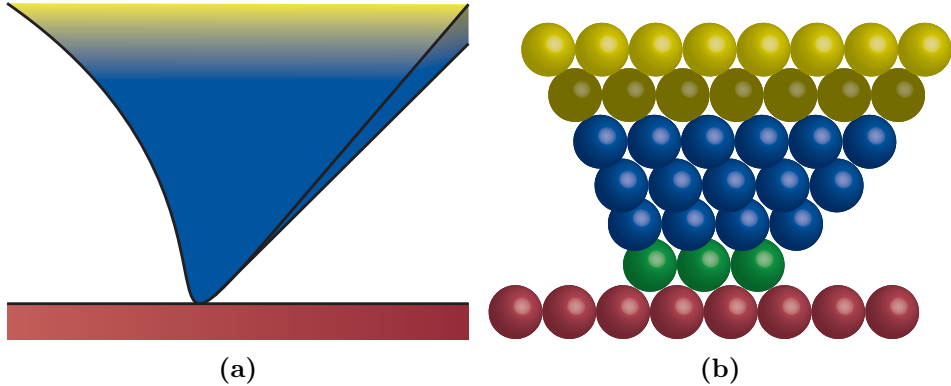


Figure 2.1: A (a) macroscopic and (b) nanoscopic schematic view of the deformation of the tip apex, prior to a slip event. The green tip apex atoms are the N_c atoms that make contact with the red substrate. The blue atoms share most of the lateral displacement of the green atoms. Together with the green atoms, they establish the N_d ‘dynamic’ atoms that will be accelerated most in the upcoming slip event. The lateral displacement of the yellow atoms is so modest, that these atoms are associated with the rigid part of the tip.

the values typically obtained when one uses the dissipation rate as the fitting parameter in the Prandtl-Tomlinson type Langevin equation shown in Equation 1.2 (cf. Section 2.1). The discrepancy is as large as six orders of magnitude. Introducing a sublinear relation between γ_{diss} and N_c , as a further element of sophistication in our description, would make the discrepancy even larger.

Using the low value for the dissipation rate, estimated above, the Langevin equation predicts heavily underdamped motion of the tip, resulting in a high probability for slip events over multiple lattice distances and thereby completely ruining the visibility of the atomic periodicity in the lateral force images.

2.4 Finding the origin of the discrepancy

When we re-inspect the Langevin equation (Equation 1.2), we recognize that the only parameter that is not defined rigorously, is the effective mass m_{eff} . We will now first discuss the character of this mass and then establish a mathematical derivation of this mass.

The effective mass comprises all atoms that move with approximately

the same velocity as the N_c atoms of the contact. This includes the N_c contact atoms and all other atoms that can be regarded as effectively forced to move together with these contact atoms. Typically, this mass is interpreted as being both the tip and a sizeable part of the cantilever, resulting in a value of around 10^{-11} kg. However, the relatively soft effective spring coefficient, by which the contact is connected to the support ($k_{\text{eff}} = 2 \text{ N/m}$), suggests that an alternative choice for this mass could be more appropriate, namely that of a small portion of the tip apex, as schematically shown in Figure 2.1a. In this figure, the tip apex is drawn while it is deformed by the shear force exerted by the substrate. Most of the deformation is concentrated near the very end of the tip.

A more detailed schematic of the tip apex is shown in Figure 2.1b. In this schematic, the tip is atomically resolved. The N_c tip atoms that are in direct contact with the substrate are coloured green. Atoms close to the friction contact, which are part of the deformed tip and hence are part of the effective mass too, are coloured blue. For reasons that will become even more clear later, the amount of atoms taking part of the effective mass (the green and blue atoms in Figure 2.1b) is denoted as N_d , the amount of ‘dynamic’ atoms. We propose to replace the combined effective mass m_{eff} , used in Equation 1.2 to describe the motion of the contact and the resulting dissipation, by the dynamic mass m_d .

2.5 Estimating the dynamic mass

We can easily derive the effect that the dynamic mass has on the experienced dissipation force in the following way. During a slip event, the apex of the tip is accelerated under the combined influence of the spring force that it experiences and the interaction force with the substrate. Over the slip distance this provides the tip apex, i.e. the dynamic mass, with an amount of kinetic energy that is independent of its own mass. The maximum velocity that this kinetic energy corresponds to, is therefore inversely proportional to the square root of m_d . According to Equation 2.1, we should thus expect that:

$$F_{\text{diss}} \propto 1/\sqrt{m_d} \quad (2.2)$$

We see that the combination of the observed, high friction forces with our low expectation value for the microscopic dissipation rate indicates that the dynamic mass is microscopically small. The earlier discrepancy of six orders of magnitude is resolved when we assume a value for m_d of 10^{-23} kg, i.e. twelve orders of magnitude lower than the typical value of 10^{-11} kg for

the tip plus part of the cantilever. This small dynamic mass corresponds to a very modest number of atoms, in full accordance with the notion, introduced above (Figure 2.1), that it is associated with the very end of the tip apex.

The reduction of the dynamic mass to such a small size, means that only the very end of the tip apex is deformed significantly during the stick phase. According to Equation 1.3, the observed effective spring coefficient k_{eff} gives a good estimate of the flexibility associated with the dynamic mass. The typical experimentally found value of k_{eff} (2 N/m) agrees with our picture of a very small, flexible end hence dynamic mass that is performing the SS-motion. For this reason, from here, we will denote the spring coefficient of the dynamic mass by k_d instead of k_{tip} .

An alternative, but equivalent line of argumentation to estimate the size of the dynamic mass, is based on the two typical timescales involved. On the one hand, we have the eigenfrequency of the dynamic mass. This sets the timescale for each slip event in terms of the dynamic mass and the effective spring coefficient, via the following relation:

$$t_{\text{slip}}^{-1} = 2\omega_d = 2\sqrt{\frac{k_d}{m_d}} \quad (2.3)$$

The other timescale is given by the time the friction contact needs to dissipate the excess energy. This timescale is set by a damping rate, denoted by η_{diss} , expressed in [sec^{-1}]. This damping rate is related to the dissipation rate, via

$$t_{\text{diss}}^{-1} = \eta_{\text{diss}} = \gamma_{\text{diss}}/m_d \quad (2.4)$$

where $\gamma_{\text{diss}} = N_c \gamma_{\text{at}}$, as before. We express the atomic dissipation rate γ_{at} as $\gamma_{\text{at}} = m_{\text{at}} \eta_{\text{at}}$, in which η_{at} is that atomic damping rate.

As the motion of single atoms is close to critically damped (see above), the atomic damping rate can be expressed as follows:

$$\eta_{\text{at}} = 2\omega_{\text{at}} = 2\sqrt{\frac{k_{\text{at}}}{m_{\text{at}}}} \quad (2.5)$$

where ω_{at} is the atomic vibration frequency and k_{at} the characteristic atomic bond stiffness. Based on these relations, the damping rate of the contact can be estimated to be

$$t_{\text{diss}}^{-1} = \eta_{\text{diss}} = \frac{\gamma_{\text{diss}}}{m_d} = \frac{N_c}{N_d} \frac{\gamma_{\text{at}}}{m_{\text{at}}} = \frac{N_c}{N_d} \eta_{\text{at}}. \quad (2.6)$$

How are the two timescales, t_{slip} and t_{diss} related? The mere observation in FFM experiments of atomic lattices characterized by stick-slip motion of

the tip apex, indicates that the excess, potential energy that is stored in the effective spring during the stick-phase is released and dissipated fully during the slip-phase of the tip apex. All potential energy is converted to kinetic energy, which is dissipated via the sliding tip. This requires the dissipation time t_{diss} to be smaller than or equal to the slip time t_{slip} . Apparently, the system has to be at least critically damped. This allows us to connect those two timescales explicitly. For convenience, we define the following relative damping rate:

$$D = \frac{\eta_{\text{diss}}}{2\omega_{\text{d}}} = \frac{\gamma_{\text{diss}}}{2\sqrt{m_{\text{d}}k_{\text{d}}}} \quad (2.7)$$

so that $D = 1$ corresponds precisely to the critically damped case. The relative damping rate D can be rewritten in a form that depends only on numbers of atoms:

$$D = \frac{N_{\text{c}}m_{\text{at}}\eta_{\text{at}}}{2\sqrt{N_{\text{d}}m_{\text{at}}k_{\text{d}}}} = \frac{2N_{\text{c}}m_{\text{at}}\omega_{\text{at}}}{2\sqrt{N_{\text{d}}m_{\text{at}}k_{\text{d}}}} = \sqrt{\frac{N_{\text{c}}^2 k_{\text{at}}}{N_{\text{d}} k_{\text{d}}}} \quad (2.8)$$

The condition that the motion of the contact is at least critically damped, can thus be expressed as:

$$N_{\text{d}} \leq \frac{k_{\text{at}}}{k_{\text{d}}} N_{\text{c}}^2 \quad (2.9)$$

This rather simple inequality has a strong implication. As the factor $k_{\text{at}}/k_{\text{d}}$ is close to 1 for typical FFM experiments, the dynamic mass has to be extremely small. This means that for a typical 10-atom contact the dynamic mass consists of at maximum 100 atoms, corresponding to a microscopic mass in the order of 10^{-23} kg. As discussed before, this mass is some twelve orders of magnitude below the effective mass that is typically associated with FFM experiments.

The ultra small size of the dynamic mass that is exploring the substrate lattice continuously and is performing the stick-slip motion, confronts us with a fundamental change of interpretation of its behaviour. Due to its size, its eigenfrequency is in the terahertz regime. As a result, the tip apex is exploring the lattice in trajectories in which it reaches extremely high velocities. This enables the tip apex to dissipate the released slip energies with extreme efficiency.

The estimates and scaling relations, presented above, ask for verification by use of adequate numerical simulations. In order to investigate and interpret this new friction scenario further, a combined 2-mass-2-spring model is necessary in which both the extremely high dynamics of the tip apex and the slow response of the cantilever are taken into account. This new

model is introduced in the next chapter, after which the results and their interpretation are given in Chapter 4.

2.6 Summary

By an estimation of the friction force on a single atom, we were able to calculate the typical dissipation rate of a friction contact. This value was found to be approximately six orders of magnitude lower than values typically used in the literature. The solution of this discrepancy was found in the choice for the mass that is deformed significantly during the stick phase and that moves significantly during the slip phase. We argued that this mass corresponds to a very modest number of atoms that is associated with the very end of the tip apex. The experimentally found value for the effective spring constant agrees with our picture of a very small, flexible and dynamic mass that has a value in the order of 10^{-23} kg. Due to this small mass, the tip apex acquires extremely high velocities, which enables the tip apex to dissipate the released slip energies with extreme efficiency. Our findings are in agreement with the observed SS-behaviour in experiments, that predicted an approximately critically damped system.

Chapter 3

The refined 2-mass-2-spring model

3.1 Introduction

As concluded in the previous chapter, a new calculation method is needed to simulate the behaviour of single-asperity friction in a realistic manner. This chapter will describe the method we constructed to simulate the essential aspects of an FFM experiment, by following the highly dynamic behaviour of the apex of an atomic-scale tip, exploring the interaction potential with the substrate, in combination with the much slower dynamics of the more macroscopic components of the FFM setup, further away from the actual contact. We also pay attention to some caveats and subtle issues.

As the content of the current chapter is rather technical, the reader might prefer to skip to the next chapter that is focussing on the physical outcome of the numerical calculations. However, to fully understand the origin of some phenomena encountered in the next chapter, the present chapter may prove useful.

During the description of the calculation methods, abbreviations and symbols will be used. We remind the reader that a list of symbols is presented in Appendix B, which can be found after Chapter 4.

3.2 From schematics to Langevin equations

Figure 3.1 shows the schematic interpretation of a single asperity friction experiment that is used as the basis for our calculations. The rigid support, which represents the scanner of the FFM, is driven by piezo-motors and scans the surface in a line-by-line mode, as is typical for AFM and STM

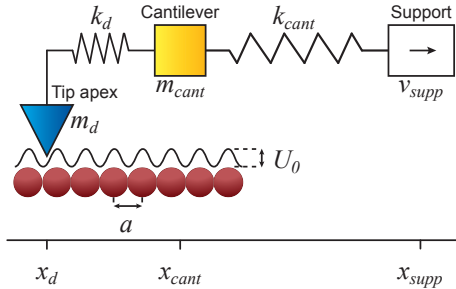


Figure 3.1: Schematics of the tip-cantilever-support combination, casted in the structure of a two-mass-two-spring model. The tip apex (the dynamic mass) is connected to the scanning support via the cantilever and it is experiencing a lattice potential with corrugation U_0 . The support is moving at a constant velocity v_{supp} .

imaging of surfaces (see Figure 10.4). When the tip apex is stuck in the corrugated potential energy landscape, the springs of both the cantilever, k_{cant} , and the tip apex, k_d , are progressively deformed. Here, we replaced the effective spring coefficient k_{eff} by the spring coefficient k_d associated with the dynamic mass m_d . The reason for this is conceptual: k_{eff} is an effective parameter, estimated by measuring the slope of the lateral force curve during the stick-phase. In contrast, k_d represents the real stiffness of the tip apex.

As we have argued in the previous chapter and as we will demonstrate by our computational results, it is essential for a complete understanding of the complex sliding behaviour, that our numerical calculations capture both the rapid dynamics of the tip apex and the slow dynamics of the cantilever. This forces us to solve the motion of two coupled 2-mass-2-spring models, namely one for the x-direction and one for the y-direction. Following the arguments provided in the previous chapter, we concentrate the damping fully in the actual tip-substrate contact.

The two-dimensional 2-mass-2-spring model can be described best with two sets of two Langevin equations: one set of two equations for the cantilever mass (x- and y-direction), and another set for the two directions of motion of the tip apex. These equations form the core of our calculation. For the tip apex, the force equations are given by

$$m_d \ddot{x}_d = - \left. \frac{\partial V_{\text{subs}}(x, y)}{\partial x} \right|_{(x, y) = (x_d, y_d)} - k_d (x_d - x_{\text{cant}}) + \xi_x - \gamma_{\text{diss}} \dot{x}_d \quad (3.1)$$

$$m_d \ddot{y}_d = - \left. \frac{\partial V_{\text{subs}}(x, y)}{\partial y} \right|_{(x,y)=(x_d, y_d)} - k_d(y_d - y_{\text{cant}}) + \xi_y - \gamma_{\text{diss}} \dot{y}_d \quad (3.2)$$

We have already made several choices in these equations. For example, we use a single value of k_d for the x- and the y-direction. This is justified by the axial symmetry of the tip, which makes the tip equally soft along x and y. Similarly, we choose the same dissipation rate γ_{diss} along the two directions. The last term in each of the equations shows how the velocity of the tip apex leads to a dissipative force. The velocity of the tip relative to the cantilever does not appear in these equations. This reflects our notion that energy dissipation takes place exclusively at the sliding interface and not somewhere inside the tip, the cantilever or any of the springs.

The motion of the cantilever is described by two even simpler equations.

$$m_{\text{cant}} \ddot{x}_{\text{cant}} = -k_{\text{cant}}(x_{\text{cant}} - x_{\text{supp}}) - k_d(x_{\text{cant}} - x_d) \quad (3.3)$$

$$m_{\text{cant}} \ddot{y}_{\text{cant}} = -k_{\text{cant}}(y_{\text{cant}} - y_{\text{supp}}) - k_d(y_{\text{cant}} - y_d) \quad (3.4)$$

Note, that, again sticking to our notion that damping is localized in the very tip-substrate contact, there is absolutely no damping in the latter two equations.

The individual components in this model are described in the following paragraphs. After the full description of the model, the computational scheme will be presented. In the final section of the chapter, we will discuss some essential timing issues.

3.3 The 2-mass-2-spring model in full detail

In this section, important details of the model are discussed. Some of these are crucial to allow a proper interpretation, others are relevant in order to understand the results quantitatively or are needed to reproduce our calculations.

3.3.1 The substrate potential

The substrate potential V_{subs} represents the interaction between the substrate and tip apex. In this work, the potential used describes a graphite lattice. In the framework of friction, its mathematical description was first

used by Kerssemakers[30, 31]. Here, the same equation will be used, except for its amplitude.

$$V_{\text{subs}}(x, y) = -\frac{U_0}{4.5} \left[2 \cos\left(\frac{2\pi}{a}x\right) \cos\left(\frac{2\pi}{a\sqrt{3}}y\right) + \cos\left(2\frac{2\pi}{a\sqrt{3}}y\right) \right] \quad (3.5)$$

The factor 4.5 in the denominator ensures that the difference between the maxima and minima of V_{subs} is equal to U_0 .

3.3.2 The spring coefficients

The values of the cantilever and tip apex spring coefficients were chosen to be $k_{\text{cant}} = 30 \text{ N/m}$ and $k_{\text{d}} = 2 \text{ N/m}$, respectively, which are typical values (see e.g. [6, 15]). This results in an effective spring coefficient k_{eff} that is approximately identical to the experimentally estimated value of 2 N/m .

3.3.3 The damping at the contact

In the preceding chapter, we have argued that the dissipation rate γ_{diss} should only depend on the characteristic atomic dissipation rate, γ_{at} , and the number of atoms in the tip that make contact with the substrate directly, N_{c} .

3.3.4 The damping of the cantilever

The energy dissipation rate of a resonator is often expressed via its so-called Q-factor, which is defined as $Q = f_{\text{r}}/\Delta f$, where f_{r} is the resonator frequency and Δf the full width at half maximum of the resonance spectrum. Typically, the Q-factor of an AFM or FFM cantilever, oscillating either in vacuum or in air, is very high, in the order of 10^5 or more. This means that the cantilever motion is extremely underdamped. In the case of our model, this implies that the cantilever dissipation is negligible with respect to the dissipation at the friction contact. For this reason, we have completely left out dissipation terms from the two equations for the motion of the cantilever (Equations 3.3 and 3.4). The only damping that the cantilever experiences is via its connection to the tip apex, which is explicitly damped (Equations 3.1 and 3.2). Note that a drop has been reported in Q-factor of cantilevers, when the tip is brought in contact with the surface[15]. As we will discuss later in this thesis, we ascribe this to a different origin.

3.3.5 The thermal noise

The thermal noise term ξ is a Gaussian distributed, uncorrelated random signal, which is completely determined by the fluctuation-dissipation theorem[13]. This thermal force is defined as

$$\langle \xi(t)\xi(t') \rangle = 2\gamma_{\text{diss}}k_{\text{B}}T\delta(t - t') \quad (3.6)$$

Computational aspects to calculate this term are discussed in Section 3.5.2 of this thesis.

3.4 Computational architecture

In order to explore the complex dynamics emanating from the four coupled Langevin equations (Equations 3.1-3.4), we have developed a tailored, numerical computational scheme. As a programming language, we have used C++. In view of the enormously different characteristic timescales for the motion of the tip apex and that of the cantilever, the calculations necessarily become lengthy. Therefore, we have been forced to pay much attention to the implementation of strategies to optimize the efficiency and speed of the calculations. The main structure of the calculation is presented in Figure 3.2. In the following paragraphs, aspects in the programming code concerning the architecture are discussed. Further details on the numerical generation of thermal noise and on the precise choice of the computational time step are presented in the next section.

At the beginning of the code, the user input variables are defined. In essence, only a few input variables are required: N_{c} , N_{d} , U_0 , k_{d} , k_{cant} and m_{cant} . All other parameters, such as γ_{diss} , were calculated on the basis of the user input.

Next, the time step dt was calculated. This value is the smallest time step in the full calculation loop. It is chosen short enough that the fast dynamics of the tip apex can be modelled correctly. The precise details of this choice are given in the next paragraph.

The thermal noise term requires random numbers that are rather time consuming to generate, as is detailed in the next section. As the number of these random numbers needed during the entire simulation is extremely large, the following method was chosen to optimize for speed. Two long arrays (several gigabyte) were created in the RAM of the computer to store the generated noise values for the x- and y-direction separately. Before the model calculation was started, these arrays were filled with properly scaled random numbers. Then, a separate thread was started that updated

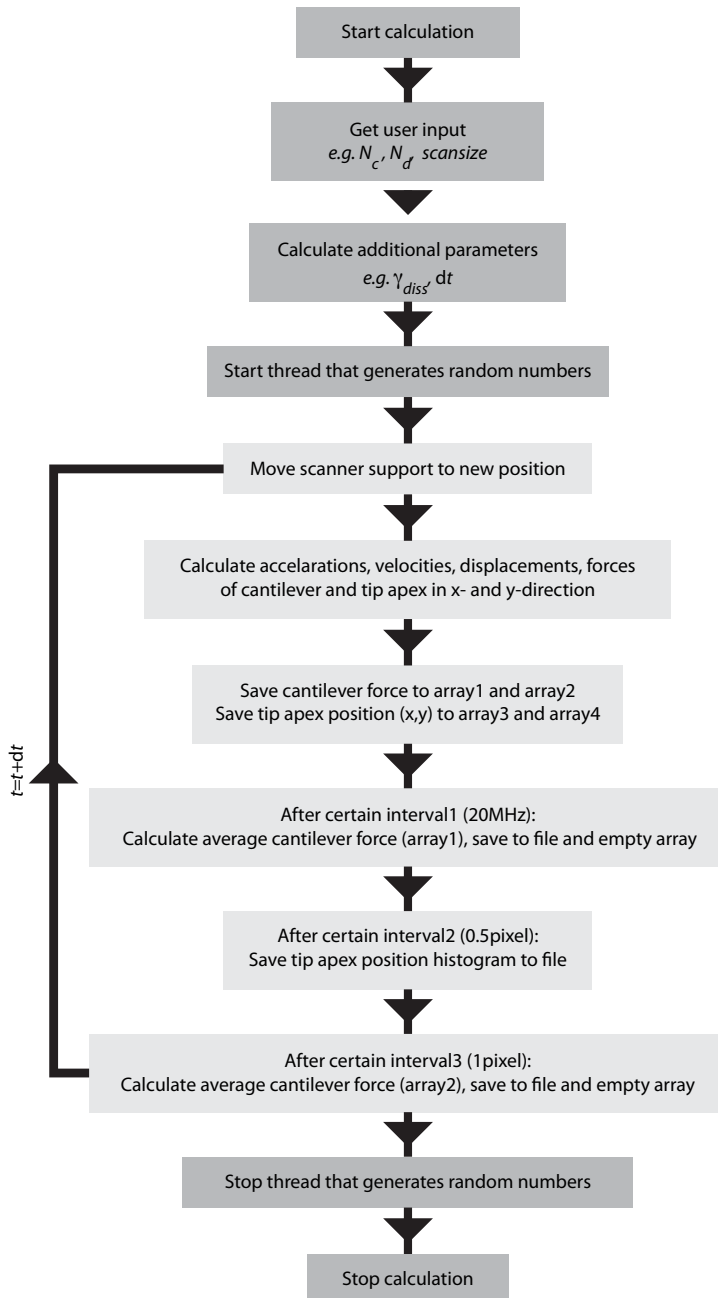


Figure 3.2: Basic structure of the software program designed to perform the model calculations. The structure is discussed in the main text in more detail.

these arrays with random numbers continuously. This thread was kept active until the entire simulation was finished. Meanwhile, the main thread started to perform the numerical calculations of the FFM-motion. During these calculations, the random numbers were taken from the arrays in the computer memory when needed. As each loop of the FFM-simulation required much less time than the update of the random numbers, the produced random numbers were used multiple times. However, as the arrays were refreshed partially before each number was reused, the occurrence of calculation errors caused by periodicities in the random number use, was minimized. This calculation method results in two cpu cores that are being used for 100 % during the simulation: one for the evaluation of the Langevin equations and one for the update of the random numbers.

As will be explained in the next section, data output to a file is not necessary during every cycle of the inner calculation loop, which is devoted to the rapid dynamics of the tip apex. Therefore, during most calculation cycles, the parameters eventually needed for the output, e.g. the lateral cantilever force and the tip apex position, were stored in the RAM. Only after a certain number of cycles, all stored values were processed (if needed) and written to a data file.

After the simulation was finished, the resulting data was processed, analysed and visualised by Python-scripts.

3.5 Time-step calculation, thermal-noise generation and data averaging

For calculation results without significant digitization noise or computational instabilities, attention has to be paid to an appropriate choice of time steps in the numerical calculation. This timing does not only effect the execution time, but also the thermal noise generation and the averaging of data points. These issues are discussed in the next paragraphs.

3.5.1 The smallest time step

An issue that has to be addressed when performing model calculations is the smallest time step required in order to capture the full behaviour of the constructed model. A time step that is too large, might make the calculation diverge and will obscure crucial, dynamic behaviour. On the other hand, a very small time step will make the execution time of the calculation very long. Therefore, an upper limit of the size of the time step has to be found.

In the calculations performed here, the maximum size of the time step is set by two conditions taken from the 2-mass-2-spring model. The first condition derives from the eigenfrequency of the most dynamic element present, i.e. the tip apex. We define one upper limit of the time step as 10% of the shortest vibrational eigenperiod of the tip apex:

$$dt_1 = 0.1 \cdot 2\pi \sqrt{\frac{m_d}{k_d + k_{\text{TSI}}^{\text{max}}}} \quad (3.7)$$

in which $k_{\text{TSI}}^{\text{max}}$ is the maximum effective contribution of the lattice potential to the effective spring coefficient, see Equation 1.3. In this manner, the time step is adapted such that the most dynamic events can be simulated correctly during the calculation.

The second constraint on the time step is taken from the random force, generated by the noise term ξ . In case of high dissipation, the fluctuations deriving from the noise will increase too, as these are coupled to each other via the fluctuation-dissipation theorem. Hence the influence of the noise on the acceleration will increase and thus one has to decrease the time step in order to prevent computational instability. As the noise has a characteristic timescale that is set a.o. by the dissipation rate, a fraction of this timescale is used to set a second upper limit to the time step:

$$dt_2 = 0.2 \cdot \frac{m_d}{\gamma_{\text{diss}}} \quad (3.8)$$

In order to capture all the dynamics in the calculations, the time step used is the shortest of these two upper limits: $dt = \min(dt_1, dt_2)$. In practice, this leads to time steps typically in the order of 10^{-12} sec.

3.5.2 Thermal-noise and random-number generation

The amplitude of thermal force ξ is defined by the fluctuation-dissipation theorem[13]. It is a Gaussian distributed, uncorrelated random noise term. To numerically calculate this element, first a Gaussian distributed random number has to be generated. Subsequently, this number has to be multiplied by a certain standard deviation.

The generation of uncorrelated random numbers that are Gaussian distributed, is done by first using a linear random number generator. The Box-Muller transformation[32], is applied to obtain Gaussian distributed random numbers with a standard deviation of 1.

The standard deviation of the random force, σ_F , is defined as

$$\langle \xi(t)\xi(t') \rangle = \sigma_{F,c}^2 \delta(t - t'), \quad (3.9)$$

where $\delta(t - t')$ is the Dirac delta function of the time difference between t and t' . The discrete version of this definition is

$$\langle \xi(t)\xi(t') \rangle = \sigma_{\text{F,d}}^2 dt \delta_{t,t'}, \quad (3.10)$$

where $\delta_{t,t'}$ is the Kronecker delta function of t and t' . This can be verified by integration/summation of Equations 3.9 and 3.10. Hence, according to the definition of the thermal force as presented in Equation 3.6, the discrete version of the standard deviation, $\sigma_{\text{F,d}}$, is defined as:

$$\sigma_{\text{F,d}} = \sqrt{\frac{2k_{\text{B}}T\gamma_{\text{diss}}}{dt}} \quad (3.11)$$

Summarizing, the standard deviation of the random force is directly dependent on the time step of our calculation. The multiplication of $\sigma_{\text{F,d}}$ with the generated Gaussian distributed random number gives the value of ξ used for the thermal force experienced by the tip apex.

3.5.3 Data averaging

The calculations result in a dataset with a time resolution in the order of 10^{-12} sec. This resolution is not comparable to the time resolution of a typical FFM experiment, which is at best in the order of ms or μ s. Hence, in order to compare the calculation results with experimental data, data averaging has to be performed. As the most detailed experiments reported were carried out using a data acquisition system with a maximum sampling rate of 20 MHz, data averaging was applied in order to realize a simulated sampling rate of 20 MHz.

Further downscaling of the sampling rate in order to match specific representations in literature, was done using additional Python-scripts. The impact of data averaging that results in lower (kHz-regime) sampling rates is discussed in the next chapter.

3.6 Summary

In this chapter we have introduced a 2-mass-2-spring model that describes the coupled motion of the light tip apex and the heavy cantilever in two dimensions by use of four coupled Langevin-type equations. In order to perform numerical calculations, a special C++-code was written. Several aspects of the calculations, e.g. speed optimization and noise generation were discussed. In the next chapter we will discuss the results of computations performed with this 2-mass-2-spring code.

Chapter 4

Computational results, their interpretation and implications

The refined 2-mass-2-spring-model, featuring a very small dynamic mass representing the tip apex, is evaluated extensively by numerical calculations. Several friction regimes were explored systematically. The most striking and elucidating results are presented in this chapter, together with their interpretation. We also highlight the implications of the results of our studies.

4.1 Results - a limited regime of atomic resolution

Following the discussion presented in Chapter 2, the friction behaviour of a friction contact is dependent on (amongst others) the number of atoms in the tip apex that make contact with the substrate, N_c , and the number of tip apex atoms that effectively move together with the contact atoms, N_d . In order to study the impact of these parameters, we performed numerical calculations in which N_c was fixed at a value of 100 (atoms) and N_d was varied from 2500 to 10^8 atoms. The value of 100 atoms for N_c is larger than the number that one should associate with a typical friction contact. The number of contacting atoms in the case of contact-AFM is typically 10. For FFM, we should expect a similar number. We have chosen a higher value for N_c in order to avoid unpractically long calculation times. However, our results should still be considered representative for the stick-slip dynamics in typical FFM experiments. The values for N_d were chosen such that, in according to Equation 2.9, overdamped, critically damped and underdamped

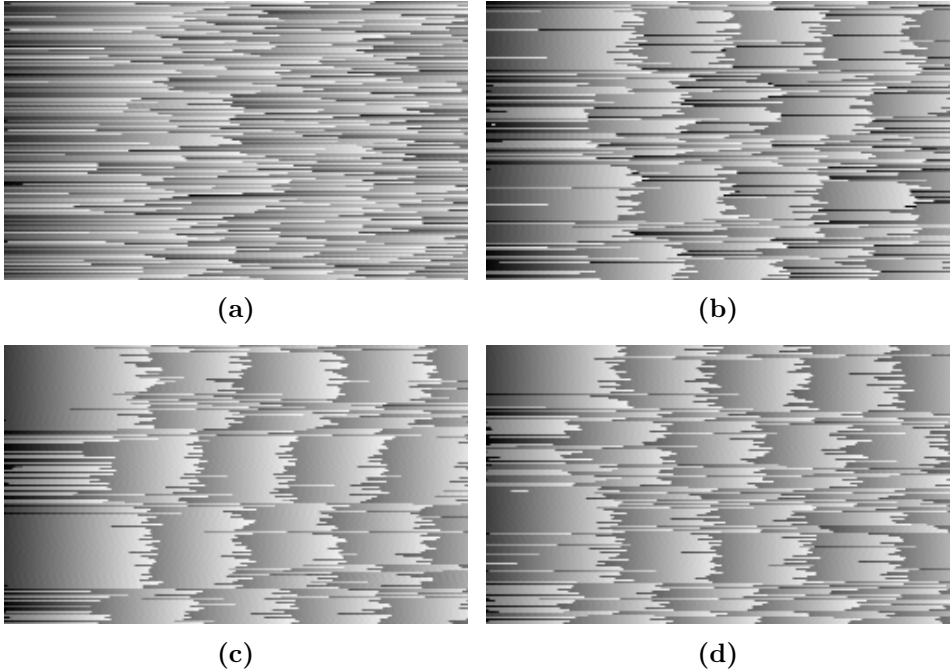


Figure 4.1: Numerically calculated lateral force maps, with the parameters chosen to match those of the FFM-experiments. ($k_{\text{cant}} = 30 \text{ N/m}$, $k_{\text{d}} = 2 \text{ N/m}$, $v_{\text{supp}} = 30 \mu\text{m/sec}$, $m_{\text{at}} = 74 \text{ amu}$, $U_0 = 0.8 \text{ eV}$ (peak-peak), $T = 298 \text{ K}$), and a number of contacting atoms of $N_{\text{c}} = 100$ (see text). The number of dynamic atoms N_{d} was chosen differently for each panel, in order to vary the damping regime. (a) $N_{\text{d}} = 10^8$, corresponding to one-hundredfold underdamped motion. (b) $N_{\text{d}} = 10^6$, $\hat{=}$ tenfold underdamped. (c) $N_{\text{d}} = 4 \times 10^4$, $\hat{=}$ twofold underdamped. (d) $N_{\text{d}} = 2500$, $\hat{=}$ twofold overdamped. Note that the two underdamped cases in (a) and (b) show many occasions with multiple slip events and that the overdamped case shows an increase in the force fluctuations. For lateral force patterns with a well-defined lattice signature, the damping should be close to critical.

situations were realized. Other parameters were chosen to match typical FFM experiments. The calculations resulted in 2-dimensional lateral force maps, of which typical examples are presented in Figure 4.1.

The numerically calculated friction force maps are in agreement with the qualitative damping rate of the friction contact that can be calculated via Equation 2.8. In the regime of a critically damped tip apex (e.g. Figure 4.1c), a regular stick-slip (SS) pattern was observed, which presents itself in a clearly visible atomic periodicity and a minor amount of thermal noise, similar to what was observed in FFM experiments. As expected, all excess kinetic energy that the tip apex acquired during the slip was dissipated rapidly enough to prevent the occurrence of double slips. On the other hand, a heavily underdamped tip apex, which corresponds to Figure 4.1a, led to a nearly complete vanishing of the atomic periodicity in the friction maps. Although the SS-behaviour was still observed, the motion had become very irregular: the precise moment and the length of the slip were unpredictable. Slips with a length of more than one atomic spacing (the so-called multiple slips) occurred frequently, which indicated that the excess kinetic energy of the tip apex was not dissipated in time and the tip apex was able to overcome the next potential barrier. As a direct consequence, the tip was able to slip to the second-next potential well at once.

The result of the calculation in which the tip apex was chosen to be slightly overdamped, is shown in Figure 4.1d. A remarkable observation is the slight degradation of the atomic periodicity in the SS-behaviour. As further overdamping of the tip apex resulted in very long calculation time, no complete 2D-maps of heavily overdamped systems were calculated. However, a quick survey showed that a more overdamped friction contact destroyed the atomic periodicity even more. A close look at the manner in which the atomic periodicities were lost, revealed that it originated in a higher degree of unpredictability of the precise moment a slip was initiated. In contrast to the underdamped situation, the occurrence of multiple slips was negligible. The origin of this stochastic-type of stick-slip can be found easily in the noise term present in the Langevin equations: it is the fluctuation-dissipation theorem that is causing the noise term to increase in a situation of high dissipation. In the overdamped case, the dissipation is relatively high and so is the noise term. These fluctuations dominate the motion of the tip apex, resulting in a loss of atomic periodicity in the friction curves.

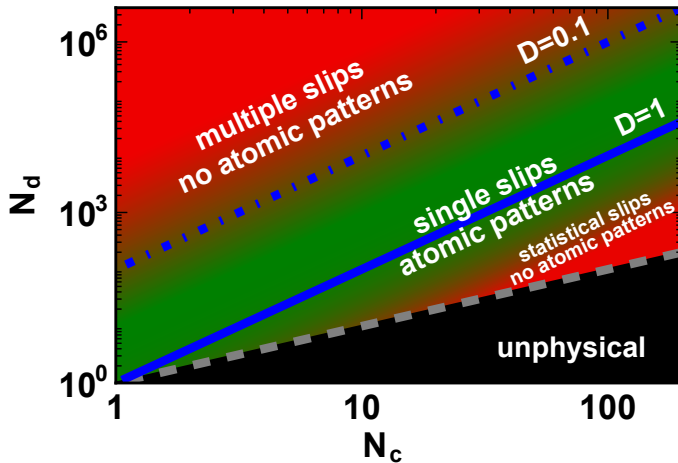


Figure 4.2: Friction ‘phase’ diagram as a function of the number of atoms N_c in the contact and the number of dynamic atoms N_d . The blue, solid line indicates the situation for critical damping of the tip apex motion, $D = N_c^2/N_d = 1$, the blue dash-dotted line indicates a tenfold underdamped system. The colours indicate the quality of the stick-slip patterns. Green corresponds to a clearly recognizable atomic lattice, and red to strongly washed out patterns.

4.2 Interpretation - modes of friction

Our theoretical description of the tip apex, presented in Chapter 2, already predicted friction behaviour of the tip apex that should depend on the tip geometry. The numerical calculations presented here show this dependence too. In case of a close to critically damped tip apex, regular SS-motion is observed. A deviation from the critically damped situation leads to a loss of atomic periodicity in the lateral force signal of the cantilever. Apparently, a limited window exists where the dissipation is high enough to avoid multiple slips and where the statistical fluctuations are not causing irregular slip occurrences.

This friction picture can be summarized and visualized by a ‘phase’ diagram as presented in Figure 4.2. This figure indicates the quality of the atomic patterns as function of the tip geometry. The colour coding is based on the numerical calculations that we performed, the indicated lines are drawn in accordance to Equations 2.8 and 2.9. We see that the friction regimes are characterized by the geometry of the tip, which is defined by N_d and N_c . The lower right, black coloured, area is physically inaccessible as the ensemble of dynamic atoms at least consist of the atoms making up

the friction contact.

In Figure 4.2, just above the unphysical area, a narrow regime is present characterised by a relatively small number of dynamic atoms and a large contact size. This makes the dissipation rate of the friction contact relatively high, resulting in overdamped behaviour. The high dissipation increases the noise on the contact behaviour, which explains that this regime is characterised by statistically initiated jumps (c.f. Figure 4.1d). The blue solid line in Figure 4.2 indicates the case of a critically damped friction contact, $D = 1$. The area around this line represents a regime in which regular SS-motion of a tip of an FFM will yield the typically observed atomic lattices in the 2D lateral force maps.

In case of a slightly underdamped tip geometry, e.g. $D = 0.1$ indicated by the dashed blue line in Figure 4.2, multiple slips occur. These slips degrade the atomic patterns in the 2D force maps, as can be seen in Figure 4.1b, where the tip geometry realized a damping factor $D = 0.1$. An even further underdamped scenario, having a damping factor of $D = 0.01$, yields a complete vanishing of atomic periodicities in the observations, see Figure 4.1a. This situation belongs to the red area in the top-left corner of the friction phase diagram shown in Figure 4.2.

4.3 Implications - tuneable friction

In view of the strict conditions on the tip geometry for obtaining atomic patterns by an FFM, visualized by the green area in the phase diagram in Figure 4.2, one might wonder why so many FFM-experiments yield regular SS-motion that results in the typically observed atomic periodicities. The answer to this question is surprisingly natural: most tips used in AFM- and FFM-experiments have geometries that make the tip apex naturally fall in the green area of the phase diagram. As a result, a typical AFM probe has a tip apex that will realise an approximately critically damped friction contact. But, on the other hand, in case we would use a completely rigid tip in an FFM, which one might regard as the optimal configuration, we would never observe regular SS-motion. Namely, this would make the dynamic mass very high, which would bring us to the upper-left, red area in the friction phase diagram: a heavily underdamped situation that destroys the observation of atomic patterns.

Our characterisation of single asperities and the narrow window of tip geometries that lead to regular SS-motion allows us to think about new strategies to control friction. For example, although the red areas in Figure 4.2 indicate a loss of regular SS, friction contacts that fall in the upper-left

red zone will result in a reduction of the average friction force experienced. The further away from the critically damped scenario, the more delocalized the single asperities will be. We regard this as a novel and attractive way to achieve low-friction contacts. Based on this approach, we can not only think of individual ‘designer’ asperities, combining a specific tip apex geometry and stiffness. The concept can be used on a macroscopic scale by an appropriate patterning of the entire surface into an ensemble of such low-friction contacts, thus generating a macroscopic, low-friction interface.

4.4 A detailed look at FFM experiments and their interpretation

Experimental reports that can be used to verify our theoretical work are rather scarce as highly time-resolved experiments are required. One of the most suited reports in the literature is the work performed by S. Maier et al.[15]. In their work, the focus was on fluctuations and jump dynamics in atomic friction experiments. Using a FFM equipped with a high-speed data acquisition system, single-asperity friction on graphite and KBr(100) was studied with a 20 MHz sampling rate. Here we will evaluate the experimental data reported in Reference [15] in the light of our work and based on this we present an alternative interpretation of their findings. The results obtained by our numerical calculations will be used to study and discuss both the tip apex behaviour and the impact of this behaviour on the observed lateral deflection of the cantilever. Consequently, the validity and strength of our numerical approach will emerge.

4.4.1 Data averaging

Both in numerical calculations and in experiments, the acquired data is often averaged in order to cancel high-frequency noise. Extra attention has to be paid in case the data rate after averaging is approaching the frequency of relevant components in the original signal within one order of magnitude. The impact of data averaging on the amplitudes of harmonics in the original signal can be evaluated by calculating the transfer function of such a digital process. In our case, data averaging of a sine function $f_0(t) = A \sin(\omega_0 t)$ over a certain time interval T_{ave} can be described mathematically as follows:

$$\langle f_0(t) \rangle_{T_{\text{ave}}} = \frac{1}{T_{\text{ave}}} \int_{t-T_{\text{ave}}/2}^{t+T_{\text{ave}}/2} f_0(t') dt'. \quad (4.1)$$

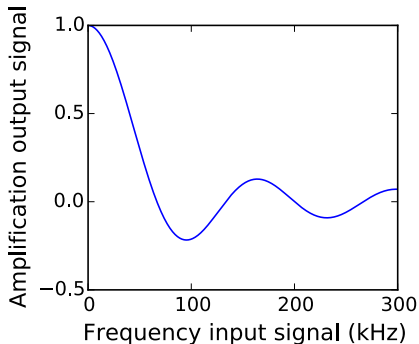


Figure 4.3: Transfer function of typical digital data averaging of an input signal towards a 66 kHz sampling rate as function of the input frequency. The graph shows that even at a frequency as high as 300 kHz signals are not completely suppressed by the low sampling rate and that at intermediate frequencies the undersampling can even lead to sign reversals of the filtered signal.

For simplicity, we show the operation in continuum space. Performing the integration and using the product-to-sum identities, leads to

$$\langle f_0(t) \rangle_{T_{\text{ave}}} = \frac{2}{\omega_0 T_{\text{ave}}} f_0(t) \sin\left(\frac{1}{2}\omega_0 T_{\text{ave}}\right), \quad (4.2)$$

which can be rewritten into

$$\langle f_0(t) \rangle_{T_{\text{ave}}} = f_0(t) \text{sinc}\left(\frac{1}{2}\omega_0 T_{\text{ave}}\right). \quad (4.3)$$

This means that data averaging over a time interval T_{ave} affects the amplitude of a harmonic with frequency ω_0 with a factor $\text{sinc}(0.5\omega_0 T_{\text{ave}})$.

In case of a $15 \mu\text{s}$ time resolution (as used in the work in Reference [15], which was the result of averaging over 50 data points of data recorded with 3.3 MHz sampling frequency), the transfer function of the data averaging applied in their situation is plotted in Figure 4.3. This figure shows the ratio between the output and input amplitudes of a harmonic signal, as function of the frequency of the harmonics in the input signal.

In order to let the calculations performed in our work match with the work done in Reference [15], we configured our filtering such that it matched with the filtering performed in Reference [15] as closely as possible. Since the eigenfrequency of the modelled cantilever was not precisely identical to that of the cantilever in the experiment, we adjusted the filter frequency

accordingly. In practice, the data for the modelled cantilever (which was stored to a file with a sampling rate of 20 MHz) was averaged over 600 data points.

As a side remark, we note that the impact of data averaging on thermal noise is such that the high-frequency part of the noise (roughly > 0.5 MHz) is removed completely and hence the observed noise band is reduced.

The residual noise band Maier et al. observed after data averaging, had an amplitude of 0.7 nN. The primary origin of this noise cannot be thermal fluctuations, as a quick calculation shows that unfiltered thermal noise on the cantilever would result in a noise force with an amplitude less than 0.3 nN. Additional data averaging would reduce this amplitude even further by nearly one order of magnitude. Hence we assume that the noise band reported in Reference [15] has its major origin in electronic noise generated by the photodiode.

4.4.2 A close look at the motion of the tip apex

The calculations performed in our studies take into account the full dynamics of both the cantilever and the tip. This detailed study allows us to zoom in on the motion of the tip apex and on the occurrences of slips and allows us to follow the reaction of the cantilever.

In order to compare the cantilever behaviour and the tip apex dynamics, one has to bridge a gap of timescales (kHz vs THz). For this, histograms were made of the tip apex positions. Every single calculation cycle (THz-scale), the x- and y-coordinates of the tip apex were stored internally. Then (on the MHz-scale) a histogram was constructed out of all tip-apex-position-data-points. This histogram was written to a file. After the calculations were finished, a Python-script imported all these histograms and plotted them as function of time (e.g. see the upper panel of Figure 4.4). In this way, a 2-dimensional map was created, which clearly shows the most frequently occurring tip apex positions along a single direction (e.g. x), over time. These maps, plotted together with the lateral force on the cantilever, enable us to look at the origin of the typically measured friction traces and to analyse the interplay between tip apex and cantilever.

A typical example of this interplay is shown in Figure 4.4. This figure is based on a simulation in which a tip was scanning a graphite lattice. In the upper panel, a histogram of the x-coordinate of the tip apex position is shown as function of time. Each individual histogram is plotted along the vertical axis and shows a distribution of the x-positions of the tip apex during a certain time interval. This map shows that the tip has performed effectively four slips during the calculations. However, an accurate look at

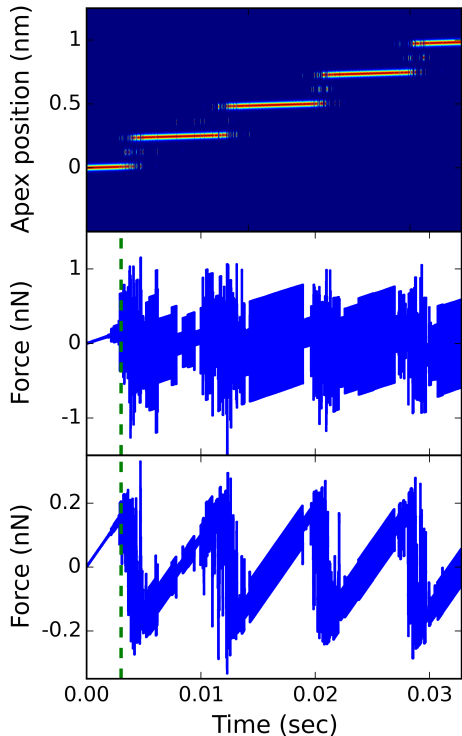


Figure 4.4: (Upper panel) Statistical representation of the x-coordinate of the tip-apex plotted as function of time. Each vertical column of pixels originates from one histogram. The colours run from blue (zero probability) via yellow (intermediate) to red (maximum probability). (Center panel) Unfiltered, 20 MHz data representing the lateral force on the cantilever. (Bottom panel) Lateral force data, originating from the cantilever, averaged in order to simulate experimental conditions in Reference [15], as detailed in the text. A zoom in of the data at the position that is indicated by the green, dashed line is presented in Figure 4.5. The calculation was performed on a graphite lattice, using the following parameters: $U_0 = 0.45 \text{ eV}_{\text{pp}}$, $m_{\text{cant}} = 10^{-10} \text{ kg}$, $m_{\text{d}} = 10^{-20} \text{ kg}$, $v_{\text{supp}} = 30 \text{ nm/sec}$, and $T = 298 \text{ K}$.

each of these four slip events reveals that at each slip the tip apex jumps multiple times at high frequency forward and backward from one lattice well to the next.

The second panel presented in Figure 4.4 shows the lateral force on the cantilever. The data sampling rate was 20 MHz. The third panel also presents the lateral force on the cantilever, but in this panel the data points were averaged over 600 points in order to effectively create the same conditions as realized in the experiments in Reference [15]. The impact of data averaging is clearly visible from the difference between the lower two panels of Figure 4.4: the SS-signature is much more pronounced after data averaging. The effect of data averaging is identical to the one reported in Reference [15]. Our focus on the tip apex position in combination with the force on the cantilever forms an additional tool that allows us to study the interaction between the tip and cantilever in more detail using our calculation model.

The next sections focus on the interpretation of the dynamics of both the cantilever and the tip apex. The experimentally inaccessible timescale, at which the tip apex moves, will be accessed by our calculations. Based on the experimental support of the results of our calculations, we reveal the behaviour of the apex of a friction contact.

4.4.3 Cantilever oscillation

The impact of a single slip-event of the tip apex on the cantilever can be studied when we compare the non-averaged (20 MHz) lateral-force data of the cantilever with the history of the tip apex position. In Figure 4.5, a zoom-in is presented of the first part of the first slip-event shown in Figure 4.4. The upper panel shows that the tip apex jumps forward and backward between lattice wells multiple times at a high frequency. The influence of each slip event of the tip apex on the cantilever is visible in the lower panel of Figure 4.5. In this figure we see that the lateral force on the cantilever oscillates. The force oscillation occurs with the cantilever eigenfrequency and is a direct consequence of the oscillatory motion of the cantilever. The amplitude and phase of the cantilever oscillation are both changed abruptly each time that the tip apex jumps.

A comparison of the middle and bottom panels of Figure 4.4 with the bottom panel of Figure 4.5 enables us to explain the complex motion of the cantilever in Figure 4.4. Especially the middle panel in Figure 4.4 shows a noisy, scattered set of data points during episodes where the tip apex jumps forward and backward many times between its current and its next lattice position. The abrupt changes in the amplitude and phase of the

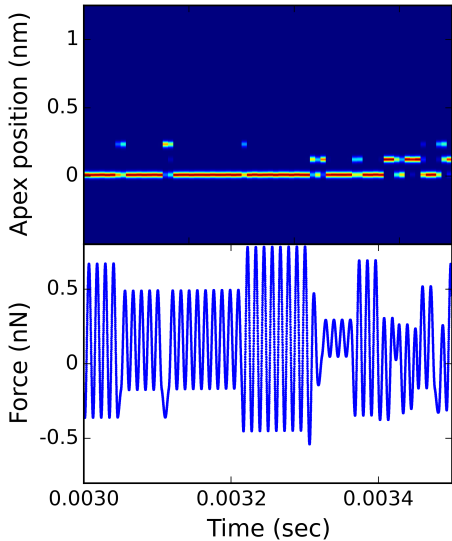


Figure 4.5: Zoom in of Figure 4.4 at the position indicated by the green, dashed line in Figure 4.4. Both the tip apex position (upper panel) and the non-averaged lateral force on the cantilever (lower panel) are plotted.

cantilever oscillation at each tip apex jump results in very complex and erratic cantilever behaviour. On the other hand, during episodes in which the tip apex is localized in a certain lattice well, a well-defined, broad band is visible in the middle panel of Figure 4.4, which means that the oscillation of the cantilever is not disturbed.

The insight in the influence of a tip-apex jump on the cantilever motion brings us to a new level of understanding of single-asperity friction. First, as the cantilever is not damped significantly (in our calculations it is even completely undamped), the energy inserted into the complete 2-mass-2-spring system by the moving support, has to be dissipated exclusively via the tip-surface contact eventually. So all energy present in the cantilever oscillation will finally reach the friction contact, although energy can be stored in the cantilever motion temporarily. The coupling of the cantilever to the tip apex is rather weak ($m_d/m_{\text{cant}} < 10^{-10}$). Therefore, direct dissipation of the cantilever's kinetic energy via the resulting, forced motion of the tip apex is negligible, as can be recognized in the second panel of Figure 4.4, where the amplitude of the cantilever oscillation remains nearly constant between subsequent jumps of the tip apex. The only way for the cantilever to lose energy efficiently, is by a sudden loss of potential energy as the direct consequence of a sudden change in the equilibrium

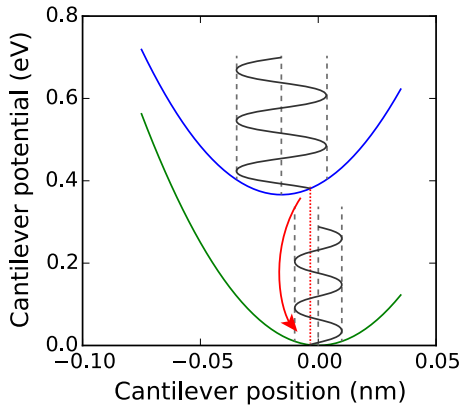


Figure 4.6: A schematic view of the change of the cantilever potential due to a jump of the tip apex. The situations before and after the jump are indicated by the blue and green curves respectively. The two curves indicate the full potential experienced by the cantilever, as a result of its connections to both the support and the tip apex. The oscillatory motion of the cantilever is indicated by the sine function. During the rapid jump of the dynamic tip apex, the position of the cantilever is not changed. The precise position and velocity of the cantilever at the moment of the tip apex jump determines its new amplitude and phase.

position of the cantilever. The equilibrium position of the cantilever is determined by the positions of the support and the tip apex (and their spring coefficients). The position of the support can be considered to remain unchanged on the timescale of a slip event. However, a jump of the tip apex from one lattice well to another takes place at a timescale characterized by the eigenfrequency of the tip apex, which is in the THz-regime. As a consequence, each time the tip apex jumps, both the equilibrium position of the cantilever and the potential energy stored in the tip-cantilever spring are changed. As the cantilever moves very slowly with respect to the tip apex, the cantilever experiences instantaneously a different force after a sudden jump of the tip apex. This results in abrupt changes of both the amplitude and phase of the cantilever oscillation. Basically, the position of the cantilever at the moment the tip-apex jumps, is crucial for its future motion. A schematic view of the change of the cantilever potential and its motion before and after a tip apex jump is shown in Figure 4.6. Note, that the change in potential energy of the cantilever goes hand in hand with an opposite change in kinetic energy of the tip apex, which is accelerated or decelerated due to the force exerted by the cantilever. This forms a highly efficient pathway for the exchange of energy between cantilever and tip apex, as is illustrated by the strong variations in the cantilever's oscillation amplitude in Figures 4.4, 4.5 and 4.6.

4.4.4 Slip duration, intermediate tip positions

Most of the highly time-resolved experiments presented in Reference [15] were performed on a KBr(100)-lattice. In order to check the influence of the substrate, we also performed numerical calculations using a lattice potential corresponding to the KBr(100)-lattice. The result of a calculation using a lattice corrugation of 0.45 eV (peak-peak) is shown in Figure 4.7. The scanning support of the cantilever was moved over 5 lattice constants, comparable to the calculations for graphite. The upper panel of Figure 4.7 shows the distribution of the x-coordinate of the tip apex as function of time. A pronounced difference with respect to the calculations performed on a graphite lattice, is the alternating long and short residence time of the tip apex in lattice wells. In the calculations shown in the upper panel, 11 locations are visible at which the tip apex resided (including the starting position). One might have expected to observe only 4-5 tip apex jumps, as the support moves over 5 lattice spacings. However, intermediate jumps are present. These are sideways jumps of the tip apex to the most easily accessible wells. In other words, the apex jumps not purely in the x-direction in which the motion of the support takes place, but it follows a minimum-

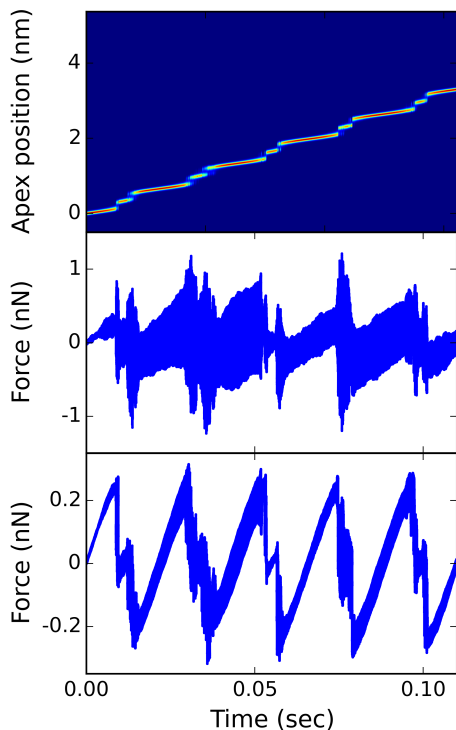


Figure 4.7: (Upper panel) Distribution of the x-coordinate of the tip-apex plotted as function of time. Each vertical column of pixels originates from one histogram. (Center panel) Unfiltered, 20 MHz data representing the lateral force on the cantilever. (Bottom panel) Lateral force data averaged in order to simulate experimental conditions (as applied in Reference [15]). The calculation was performed on a KBr(100)-lattice, using the following parameters: $U_0 = 0.45 \text{ eV}_{\text{pp}}$, $m_{\text{cant}} = 10^{-10} \text{ kg}$, $m_{\text{d}} = 10^{-18} \text{ kg}$, $v_{\text{supp}} = 30 \text{ nm/sec}$, and $T = 298 \text{ K}$.

energy zig-zag trajectory over the surface, in which it passes through other energy wells at intermediate x-coordinates. The y-motion of the tip apex, recorded in our calculations, supports this interpretation.

A detailed look at the tip apex behaviour on graphite, as shown in Figure 4.5, reveals that also in that case the tip performs jumps with a length of half a lattice distance in the x-direction. Also on graphite, the tip performs jumps in the sideways directions. However, the position of the tip apex in those sideways-positioned lattice wells is energetically not very favoured, which leads to negligibly short residence times of the tip apex in these positions.

The dynamic behaviour of the tip apex jumping between lattice wells results in a very specific behaviour of the cantilever deflection, especially after data-averaging. This can be seen most clearly in the lower panels in Figures 4.4 and 4.7. On the KBr(100)-lattice, the stable, intermediate positions of the tip apex result in an extra level in the lateral force curves. On graphite, the jumpiness of the tip apex shows up differently in the friction force data. After averaging of the tip apex x-position over many individual jumps, a gradual slope emerges. This is the result of the statistical average of the amount of time the tip resides in the discrete lattice wells. So the rapid dynamics of the tip apex, which jumps between well-defined, discrete positions is obscured in the experiment by the both the relatively slow cantilever and the subsequent data averaging.

In short, in the experiment, the slips may appear like very slow events, however, in reality, each individual slip duration is more or less identical (characterized by the eigenfrequency of the tip apex) and the apparent slip duration is a consequence data averaging carried out on the deflection signal of the ‘slow’ cantilever. This new insight explains most of the data observed in Reference [15] and yields a more fundamental interpretation of their experiments, based on the dynamic behaviour of the friction contact.

4.4.5 The Q-factor of the cantilever

In Section 3.3.4 the damping of the cantilever was described by its Q-factor. As we show in Appendix A, the Q-factor of the cantilever can be expressed as follows.

$$Q = \frac{1}{2D} \left(1 + \frac{4\pi^2 U_0}{k_d a^2} \right)^2 \sqrt{\frac{m_{\text{cant}}}{m_d} \frac{k_{\text{cant}}}{k_d}} = \frac{1}{2D} \left(1 + \frac{k_{\text{TSI}}}{k_d} \right)^2 \sqrt{\frac{m_{\text{cant}}}{m_d} \frac{k_{\text{cant}}}{k_d}}. \quad (4.4)$$

In this equation, not only the influence of the connection of the cantilever to the support and to the dynamic mass, but also the influence of the

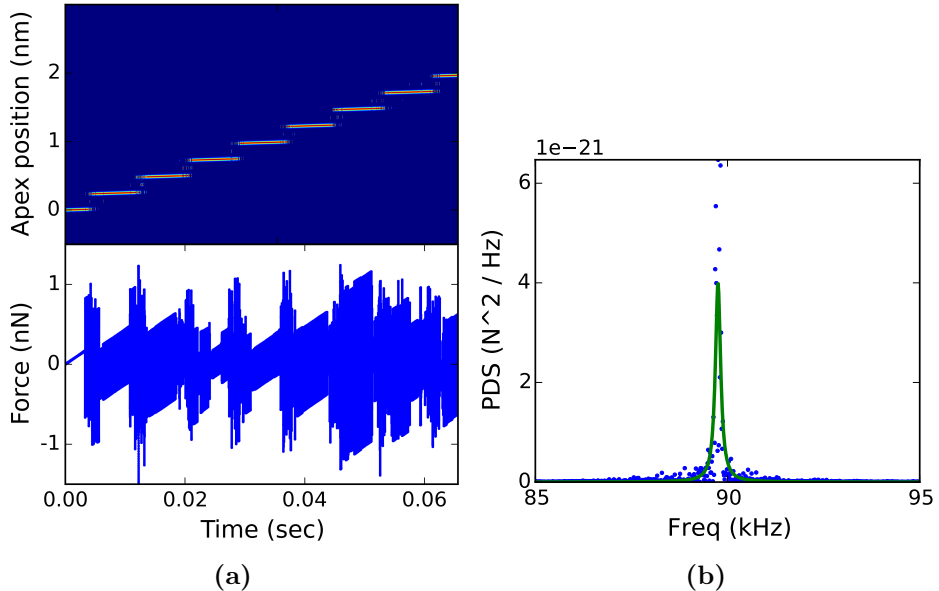


Figure 4.8: Result of a numerical calculation of a tip scanning over graphite at room temperature. (a) Distribution of the x-coordinate of the tip apex (top) and the non-averaged lateral force on the cantilever (bottom) during a typical SS-motion on graphite. (b) Fourier spectrum of the lateral force on the cantilever. The estimation of the Q-factor is indicated by the green fit, which is characterised by the following parameters: $FWHM = 83.1$ Hz, $Center = 89.8$ kHz, $Q = 540$.

tip-substrate interaction is taken into account.

The Q-factor of the cantilever is known to decrease many orders of magnitude when the tip is brought in contact with a substrate, although the origin of this effect is not fully understood yet [15]. Our numerical calculations present a suitable tool to investigate the effect of the tip-substrate interaction on the Q-factor of the cantilever. First, a calculation was done in which a typical FFM experiment was simulated. The cantilever and tip were dragged by the support moving at a velocity of 30 nm/sec over the graphene lattice potential with a corrugation of 0.4 eV, at room temperature. The Q-factor was determined by a Fast Fourier Transformation (FFT) and found to be approximately 540, see Figure 4.8. Second, a situation was created that was intended to realize a ‘delocalized’ tip that is jumping forward and backward between two lattice wells. To realise this, the support was fixed at a position just in between two lattice wells in the tip-substrate interaction potential, maximizing the enharmonic contribution of the inter-

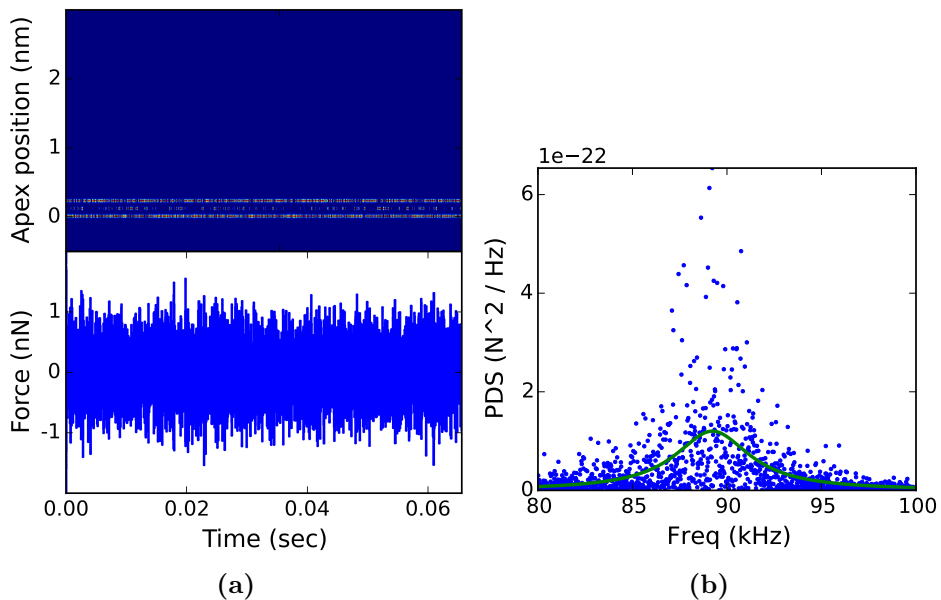


Figure 4.9: Result of a numerical calculation at room temperature of a tip-cantilever system, while the support is positioned right in between two minima, i.e. above a local maximum, of the interaction potential between the tip apex and the graphite substrate. (a) Distribution of the x-coordinate of the tip apex (top) and the non-averaged lateral force on the cantilever (bottom) during a typical SS-motion on graphite. (b) Fourier spectrum of the lateral force on the cantilever. The estimation of the Q-factor is indicated by the green fit, which is characterised by the following parameters: $FWHM = 2.41$ kHz, $Center = 89.2$ kHz, $Q = 18.5$.

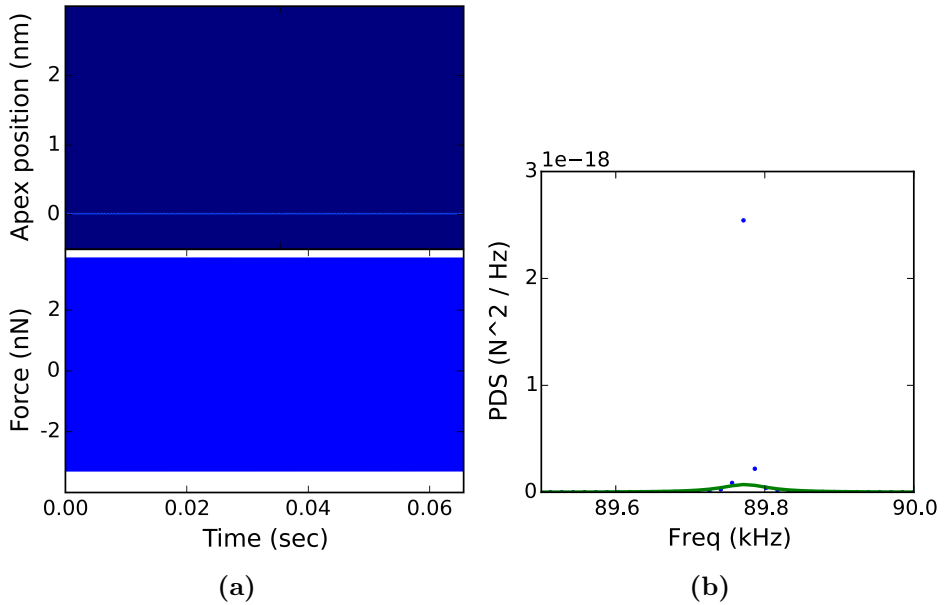


Figure 4.10: Result of a numerical calculation of a tip-cantilever system, while the support is positioned right in between two minima, i.e. above a local maximum, of the interaction potential between the tip apex and the graphite substrate. The temperature was set to 0 K in order to prevent thermally activated jumps of the tip apex. (a) Distribution of the x-coordinate of the tip apex (top) and the non-averaged lateral force on the cantilever (bottom) during a typical SS-motion on graphite. (b) Fourier spectrum of the lateral force on the cantilever. The estimation of the Q-factor is indicated by the green fit, which is characterised by the following parameters: $FWHM = 38.5$ Hz, $Center = 89.8$ kHz, $Q = 1170$.

action potential. The thermal fluctuations cause the tip to jump between the minima in the interaction potential many times, as can be seen in the results of the calculations that are presented in Figure 4.9. The Q-factor of the lateral force signal from the cantilever has dropped significantly to a value of 18.5. In order to verify that thermal fluctuations have been solely responsible for this strong reduction of the Q-factor, we have repeated the calculation for precisely the same configuration, i.e. with the support positioned precisely between two neighbouring potential wells, but now at zero temperature. As can be seen in Figure 4.10, the absence of fluctuations resulted in a very ‘localized’ tip. The Q-factor has increased to a value of at least 1170. In fact, this value should be regarded as a lower estimate of the Q-factor, as a result of the finite resolution of the calculation.

These numerical calculations reveal a dramatic impact of the tip-substrate dynamics on the measured Q-factor. As demonstrated in Figures 4.8-4.10, the mere presence of the lattice does not explain the deterioration of the Q-factor. In Section 4.4.3 we demonstrated that a delocalized tip apex that is jumping forward and backward, has a major impact on the amplitude and the phase of the oscillating motion of the cantilever. As a direct result, the cantilever motion can no longer be described properly by a single resonance frequency and the FFT acquires a significant width, as is illustrated dramatically in Figure 4.9. The impact of this noise on the Q-factor is in the order of several orders of magnitude. Summarizing we can state that the Q-factor is affected significantly by the dynamics of the tip apex.

Our findings are supported fully by the experimental results presented in Reference [15]. In that report, it can be recognized that the ‘noisy’ FFT-spectrum measured using a sharp tip on an $\text{Al}_2\text{O}_3(0001)$ -substrate is fully consistent with the analysis and interpretation presented here. In addition, the spectra reported in Reference [15] that are recorded using micrometer-scale spherical tips do not exhibit the discussed ‘noise’, which is not a surprise as these tips are not expected to create a single-asperity contact with the substrate. As a consequence, the recorded lateral forces originate from an averaged behaviour of all individual nanocontacts of the blunt tip with the substrate.

Using the interpretation presented here, both the qualitative nature of the lateral force spectra and the quantitative behaviour of the Q-factor is explained. The origin of the behaviour of the measured cantilever deflection is rooted in the extremely dynamic behaviour of the tip apex. Although the cantilever is much heavier than the tip apex, every single high-frequency slip of the tip apex affects the cantilever motion, resulting in a significant

impact on the Q-factor of the cantilever.

4.5 Summarizing conclusions

Numerical calculations using the refined 2-mass-2-spring model resulted in friction force maps that contained a limited regime in which atomic periodicities are clearly observed. This regime is characterised by a specific ratio between the number of atoms present in the contact and in the dynamic mass. When this ratio led to a critically damped tip apex, regular SS-patterns were observed. In other scenarios, either the underdamped tip apex led to multiple slips or the overdamped tip apex resulted in a stochastic-type of stick slip.

Our numerical model allowed us to zoom in on the motion of the tip apex and on the reaction of the cantilever on slip events of the tip apex. Based on the experimental support of the results of our calculations, we revealed the behaviour of the tip apex of a friction contact. The typical observations of the lateral deflection of the cantilever was explained and further insight in special behaviour of the tip apex was achieved.

Also, we concentrated on the Q-factor of the cantilever. The absence of explicit damping on the cantilever and the marginal damping of the cantilever via the small tip apex could not explain the drop in the A-factor that is typically reported in literature. We showed that the SS-behaviour of the tip apex as a significant influence on the determined Q-factor of the cantilever.

Based on our theoretical model of a friction contact and on the calculational results, we constructed a friction ‘phase’ diagram. As most tips used in AFM- and FFM-experiments have geometries that make the tip apex naturally critically damped, regular SS-motion is readily observed. Deliberate construction of asperities with a geometry that would lead to low friction contacts, opens a way to predict and tune the friction of maybe even macroscopic surfaces.

Appendix A

Theoretical description of the Q-factor of the cantilever

In Chapter 4, the Q-factor of the cantilever was discussed. The Q-factor was estimated via the frequency spectrum of the lateral force on the cantilever. At the very beginning of the discussion, a theoretical expression of the Q-factor was given in Equation 4.4. Here, we will derive this equation. But first, we motivate the need for an alternative expression with respect to known versions present in the literature.

A.1 Motivation

In Reference [15], a derivation of the Q-factor was made by Maier et al. in an attempt to explain the Q-factors that were estimated based on their experiments. One of the assumptions made in this derivation, was that the tip apex followed the motion of the cantilever. The results of our numerical calculations do not justify this assumption: we have shown that the tip apex is oscillating most of its time in the lower part of the substrate potential wells. At the same time, the stiff cantilever oscillates with its own characteristic frequency. The relatively soft spring between the cantilever and the tip apex makes the tip apex significantly decoupled from the cantilever.

Our alternative derivation is meant to incorporate the effect of the presence of the substrate potential and the effect of the decoupling between the tip apex and the cantilever.

A.2 Derivation of Equation 4.4

The Q-factor of the cantilever is defined as

$$Q = 2\pi \frac{E}{\Delta E}, \quad (\text{A.1})$$

where E is the energy stored in the oscillator, and ΔE is the energy loss per oscillation cycle of the cantilever. Here, we are interested in the case where the cantilever is coupled to the flexible tip apex, which turns our system into a 2-mass-2-spring system.

For the sake of simplicity, we treat the symmetric case, in which the equilibrium positions of the support, the cantilever and the tip apex are coinciding with a local minimum in the substrate potential.

We will calculate the energy loss per oscillation cycle of the cantilever ΔE , under the following assumption:

Assumption 1: We assume that the intrinsic damping of the cantilever is so weak that it can be ignored completely.

This assumption simplifies our derivation of ΔE , as the energy dissipation is now only concentrated in the tip apex:

$$\frac{dE}{dt} = -\gamma_{\text{diss}}(\dot{x}_{\text{d}}(t))^2. \quad (\text{A.2})$$

Now, we have to establish a relation between the motion of the cantilever and that of the tip apex. First, we define the motion of the cantilever as follows:

$$x_{\text{cant}}(t) = A_{\text{cant}} \sin(\omega_{\text{cant}} t). \quad (\text{A.3})$$

The motion of the tip apex, x_{d} , is coupled to the time-dependent position of the cantilever and to the substrate. This coupling can be made explicit via the combined potential that is experienced by the tip apex:

$$V_{\text{d}}(x_{\text{d}}(t)) = \frac{1}{2}k_{\text{d}}(x_{\text{d}}(t) - x_{\text{cant}}(t))^2 - U_0 \cos\left(\frac{2\pi}{a}x_{\text{d}}(t)\right), \quad (\text{A.4})$$

in which the two terms on the right-hand side represent the tip-cantilever spring potential and the tip-substrate interaction potential, respectively. As the tip apex is a very dynamic element, especially with respect to the much heavier cantilever, we can describe its motion as a rapid oscillation around the time-dependent minimum x_{d}^* of V_{d} . The position of this minimum is given by

$$x_{\text{d}}^*(t) = x_{\text{cant}}(t) - \frac{2\pi U_0}{k_{\text{d}} a} \sin\left(\frac{2\pi}{a}x_{\text{d}}^*(t)\right). \quad (\text{A.5})$$

Assumption 2: As the amplitude of the tip apex oscillation is small with respect to width of the substrate potential wells, we can approximate the shape of the substrate potential by a parabola, so that $\sin(ax) \approx ax$.

This assumption simplifies Equation A.5 to:

$$x_d^*(t) = \left(1 + \frac{4\pi^2 U_0}{k_d a^2}\right)^{-1} x_{\text{cant}}(t) = \varepsilon x_{\text{cant}}(t). \quad (\text{A.6})$$

We can describe the motion of the tip apex as a rapid oscillation around this time-dependent potential energy minimum:

$$x_d(t) = A_d \sin(\omega_d t) + \varepsilon A_{\text{cant}} \sin(\omega_{\text{cant}} t). \quad (\text{A.7})$$

From this we obtain the velocity of the tip apex:

$$\dot{x}_d(t) = A_d \omega_d \cos(\omega_d t) + \varepsilon A_{\text{cant}} \omega_{\text{cant}} \cos(\omega_{\text{cant}} t). \quad (\text{A.8})$$

This can be used to calculate the energy dissipation rate at the tip apex:

$$\begin{aligned} \frac{dE}{dt} &= -\gamma_{\text{diss}} \dot{x}_d^2 \\ &= -\gamma_{\text{diss}} (A_d^2 \omega_d^2 \cos^2(\omega_d t) \\ &\quad + \varepsilon^2 A_{\text{cant}}^2 \omega_{\text{cant}}^2 \cos^2(\omega_{\text{cant}} t) \\ &\quad + 2\varepsilon A_d A_{\text{cant}} \omega_d \omega_{\text{cant}} \cos(\omega_d t) \cos(\omega_{\text{cant}} t)). \end{aligned} \quad (\text{A.9})$$

If we integrate this over one full oscillation period of the cantilever, we obtain the total energy loss per cycle:

$$\Delta E = \left(\frac{\pi}{\omega_{\text{cant}}}\right) \gamma_{\text{diss}} (A_d^2 \omega_d^2 + \varepsilon^2 A_{\text{cant}}^2 \omega_{\text{cant}}^2). \quad (\text{A.10})$$

In the integration, the cross term in dE/dt leads to a zero contribution. The two remaining terms can be associated with the dissipation due to the separate contributions from the rapid tip apex motion and the much slower motion of the tip apex's equilibrium position due to the cantilever oscillation. It is the latter term that we associate with the modest dissipation of the cantilever motion via the tip apex. This is the cantilever energy loss per oscillation cycle that we need to determine:

$$\Delta E = \pi \gamma_{\text{diss}} \omega_{\text{cant}} \varepsilon^2 A_{\text{cant}}^2. \quad (\text{A.11})$$

The energy of the cantilever oscillation is equal to:

$$E = \frac{1}{2} m_{\text{cant}} \omega_{\text{cant}}^2 A_{\text{cant}}^2 \quad (\text{A.12})$$

Using these expressions for E and ΔE , we can now calculate the corresponding Q-factor to be:

$$Q = \frac{m_{\text{cant}}\omega_{\text{cant}}}{\gamma_{\text{diss}}\varepsilon^2} \quad (\text{A.13})$$

Using Equation 2.7, which stated that $\gamma_{\text{diss}} = 2\sqrt{m_{\text{d}}k_{\text{d}}}D$, we can rewrite Equation A.13 as

$$Q = \frac{1}{2D\varepsilon^2} \frac{m_{\text{cant}}\omega_{\text{cant}}}{\sqrt{m_{\text{d}}k_{\text{d}}}}. \quad (\text{A.14})$$

This relation can be further simplified, which results in the expression of the Q-factor given in Equation 4.4:

$$Q = \frac{1}{2D} \left(1 + \frac{4\pi^2 U_0}{k_{\text{d}}a^2}\right)^2 \sqrt{\frac{m_{\text{cant}}}{m_{\text{d}}} \frac{k_{\text{cant}}}{k_{\text{d}}}} = \frac{1}{2D} \left(1 + \frac{k_{\text{TSI}}}{k_{\text{d}}}\right)^2 \sqrt{\frac{m_{\text{cant}}}{m_{\text{d}}} \frac{k_{\text{cant}}}{k_{\text{d}}}}. \quad (\text{A.15})$$

What the equation shows is that the mass ratio between the cantilever and the tip apex makes the damping of the cantilever motion via the forced motion of the tip apex extremely inefficient. In addition it shows that the effectiveness of this weak dissipation channel depends strongly on the amplitude of the tip-substrate interaction potential.

The form derived here for the Q-factor was tested by numerical calculations that comprised ringdown tests using our 2-mass-2-spring model with various, realistic amplitudes of the graphite substrate potential, including the extreme case of a flat potential. The Q-factor in these calculations, that was estimated via the decay of the cantilever oscillation amplitude, was (within the statistical error margin of the calculations) identical to the Q-factor calculated via Equation 4.4.

Appendix B

List of symbols

List of all symbols used in the first part of this thesis. The symbols are put in alphabetical order. Greek symbols are put at the end of the list.

a	lattice constant of the substrate
D	relative damping rate of the friction contact, $D = 1$ corresponds to the critically damped case
F_{diss}	the dissipative force on the dynamic mass m_{d}
k_{at}	spring constant associated with each of the atomic bonds in the tip
k_{B}	Boltzmann's constant
k_{cant}	(torsional) cantilever spring constant
k_{d}	spring constant with which the dynamic tip mass m_{d} is connected to the rigid remainder of the tip plus the cantilever
k_{eff}	effective spring constant of the entire system (from support to substrate)
k_{subs}	spring constant associated with the stiffness of the substrate
k_{tip}	spring constant of the tip
k_{TSI}	spring constant associated with the tip-substrate interaction
m_{at}	atomic mass of the atoms in the tip
m_{cant}	effective mass of cantilever
m_{d}	dynamic mass, i.e. the mass associated with the N_{d} dynamic atoms
m_{eff}	effective mass present in the 1-mass-1-spring model, which is pulled through the substrate potential

N_c	number of atoms making physical contact with the substrate
N_d	number of dynamic atoms, i.e. the effective number of atoms moving at same speed as the N_c contact atoms
Q	quality factor of an oscillator, which is in our work the cantilever
T	the temperature of the system
t_{diss}	timescale set by the damping rate η_{diss}
t_{slip}	timescale for a slip event of the dynamic mass
U_0	corrugation amplitude of the periodic substrate potential V_{subs}
V_{subs}	substrate potential
v_{supp}	velocity of the support
x_{cant}	x-coordinate of the cantilever
x_d	x-coordinate of the dynamic mass
x_{supp}	x-coordinate of the support
x_t	x-coordinate of the tip apex

Greek symbols

γ	dissipation rate [kg/sec]
γ_{at}	dissipation rate of one single atom in the contact [kg/sec]
γ_{diss}	dissipation rate of the entire contact [kg/sec]
η_{at}	damping rate of one single atom in the contact [sec^{-1}]
η_{diss}	damping rate of the dynamic mass [sec^{-1}]
μ	macroscopic friction coefficient
ξ	Gaussian distributed random noise term
σ_F	standard deviation of the random force
ω_{at}	typical (angular) frequency for vibrations of an atom in the tip
ω_d	(angular) eigenfrequency for vibrations of the dynamic mass

Part II

Graphene growth on Ir(111)

Chapter 5

Introduction, instrumentation and methods

5.1 A short introduction to graphene

5.1.1 The need for reliable graphene production methods

After the experimental discovery of graphene by Geim et al. in 2004[33], this material has obtained enormous attention as many of the extraordinary properties that have been predicted theoretically, have been confirmed by scientific experiments. The uniqueness of graphene is in its internal structure. Graphene is the thinnest possible material, with a thickness of a single atom. It is a 2-dimensional network of carbon atoms solely, which are ordered in a honeycomb lattice. All carbon atoms are connected to each other via sp^2 -bonds, which make it mechanically the strongest material known. Although graphene sheets can be stacked, for example to form graphite, the VanderWaals interactions between the sheets are weak with respect to the strong, in-plane bonds.

The rather simple internal structure of graphene makes it attractive both theoretically and experimentally. For example, research has shown that graphene is resistant to many chemical environments, putting graphene forward as a candidate for protective coatings[34]. Its electronics properties make graphene promising for future electronics, for example for photonics, high-frequency and energy storage applications[35–37]. In addition to this, the strength and the 2-dimensional nature of graphene can be used to apply graphene on surfaces in order to reduce friction at interfaces[1].

For industrial applications and all other forms of large-scale use of graphene, e.g. in research, methods are required for mass production of high-quality graphene. The first samples of graphene were obtained via mechanical exfoliation of graphite[38]. Using Scotch tape, natural graphite was cleaved repeatedly until one layer of graphite (i.e. graphene) was left. This method is sufficient for many laboratory purposes, but does not satisfy industrial requirements of scalability and controlled quality. Currently, well-known ways to synthesize graphene applicable for mass production are the growth from silicon carbide (SiC) and the chemical vapor deposition (CVD) of graphene from a carbon containing gas on a transition metal[35].

It has turned out to be far from straightforward to synthesize graphene with a quality, e.g. defect density, as good as graphene obtained by mechanical exfoliation. Nevertheless, graphene production recipes are being developed delivering material of steadily improving quality[39, 40]. However, the graphene sheets produced nowadays still suffer from various issues, such as defects in the form of domain boundaries[41], contaminations and wrinkles that originate from the growth method or from used transfer methods[42, 43].

The most promising and most widely used method to synthesize graphene is the growth via CVD. In this process, typically hydrocarbons are deposited on a transition metal. At a certain temperature, the hydrocarbon molecules decompose and leave carbon on the substrate. When appropriate conditions are applied (e.g. gas pressure, substrate temperature) the carbon atoms will form graphene nuclei and growth of graphene can be realized by further addition of carbon.

A complete understanding of the complex CVD-process is required in order to manage it such, that one can prevent the creation of defects and suppress other processes that degrade graphene. Once all stages of the graphene growth process are fully under control, a process flow can be designed such that nearly perfect, macroscopically sized layers of graphene can be synthesized. This should result in a reliable recipe to produce graphene on an industrial scale.

5.1.2 Graphene growth on Ir(111)

To study thin film growth, typically single crystals are used. The crystal surfaces are used as model systems and allow systematic research of the synthesis of e.g. graphene. A popular substrate surface used to grow graphene, is the Cu(111) surface. As the solubility of carbon in copper is relatively low, this substrate allows for self-limiting growth of monolayer graphene.

The growth of graphene on copper takes place at a temperature of approximately 1325 K. At this temperature, the vapor pressure of copper is so high, that copper is leaving the surface at a rate of approximately 200 monolayers per second[44]. This effect would make it hard to scan the surface with the STM for long periods of time as the surface level is retracting itself over time. In addition, we find that the scanning of a copper surface with the STM at 1325 K immediately leads to the formation of a ‘neck’ between the surface and the STM tip, like reported before in the case of scanning of Pb surfaces with an STM tip at a temperature of 318 K[45]. Summarizing, the growth of graphene on copper cannot be studied by STM *in situ* at the appropriate, high CVD temperature.

In order to use STM imaging to obtain atomic-scale insight in CVD growth of graphene on metal surfaces, we are forced to take refuge in alternative metals. One of the metal surface that we have employed for this purpose is Rh(111). Studies on this surface, performed in our research group, showed that the substantial solubility of carbon in rhodium cannot be neglected during growth of graphene[46]. Carbon that is dissolved into the rhodium bulk during the CVD process and that segregates to the surface of the rhodium crystal when the rhodium is cooled down to room temperature, subsequently, was found to affect the growth of graphene and to complicate the recipe to grow graphene with a minimal density of grain boundaries.

A metal that has both a low vapor pressure and a negligible carbon solubility is iridium. Ir(111) has been used already to study the growth of graphene, which revealed that the iridium surface is well suited for studying the growth of monolayer graphene in an ultrahigh vacuum (UHV) environment, even at high temperatures. Like several of the other metal surfaces, the lattice mismatch between Ir(111) and graphene leads to the formation of a superstructure, a moiré pattern, that enables one to study properties of graphene growth at the atomic scale, without necessarily having atomic resolution with the STM. For these reasons, Ir(111) was chosen as the substrate for our experiments.

The nucleation and growth of graphene on Ir(111) have been studied before using different techniques. Examples are: room-temperature investigation at the atomic scale by STM in UHV after temperature-programmed growth (TPG)[47]; real-time, *in situ* investigation by carbon evaporation in high vacuum by Low Energy Electron Microscopy (LEEM)[48] and real-time, *in situ* investigation of the thermal evolution of room-temperature deposited ethylene by high-energy-resolution, fast X-ray photoelectron spectroscopy[49]. These experimental approaches have improved significantly

the understanding of the growth mechanism of graphene on Ir(111). However, a direct observation of the nucleation, ripening and growth of graphene at the nanoscale is still lacking. A technique that would allow us to perform such observations might answer several fundamental questions on graphene synthesis.

A promising instrument to provide these nanoscale observations is the variable-temperature STM (VT-STM) in a UHV system[50]. This STM setup combines both the nanoscale resolution and the well-defined, variable- and high-temperature environment to study the nucleation and growth of graphene *in situ*. In our research group, such a microscope was developed and built-up several years ago. More details on this equipment can be found in the next section. In this part of the thesis, we present the experimental results on the graphene-iridium system, obtained using this home-built VT-STM.

5.2 Instrumentation

All experiments reported in this part of the thesis were performed in the UHV system that is described in more detail in the PhD thesis of M.J. Rost[51]. The system was located in the Huygens-Kamerlingh Onnes Laboratory of Leiden University. In this section we mention the most relevant components of this setup, with an emphasis on the parts that have been modified for the present work.

5.2.1 Vibration isolation

In order to reduce the influence of external vibrations, several measures were taken to minimize the sensitivity to these vibrations. First, the system is resting on a floor segment with separate foundation. Second, the vacuum system is put on four Newport[52] Laminar Flow Stabilizers. Next, the STM is suspended by a set of springs and finally an eddy current damping system is installed.

5.2.2 Vacuum system

The setup currently consists of four chambers, two of them containing a variable-temperature STM. These two chambers are connected to each other via a transfer chamber with a loadlock system attached to it.

The loadlock system

The loadlock system allows the users to load and unload both samples and STM scanheads/tips without venting the STM and transfer chambers. A Pfeiffer[53] TCM 180 magnetically levitated turbopump is used to pump down the loadlock compartment. Eurotherm[54] programmable temperature controllers and heating tapes are used to bake the loadlock system. In case a quick check or repair of either a sample or an STM scanner is needed, baking is not required: quick heating of the open loadlock unit in air using a heat gun, prior to pumpdown is sufficient.

The transfer chamber

The transfer chamber contains a mechanism to distribute samples or STM scanheads inside the whole vacuum system. This mechanism exists of a tape drive, which can be operated via two rotary feedthroughs. Using those feedthroughs, a tape with a carrier attached to its very end can be driven over a rails into the desired UHV chamber. Then, wobble sticks can be used to (un)load samples or scanners on the carrier. A Riber[55] ion pump is used to maintain the vacuum in the transfer chamber. Three pneumatic gate valves are located in between the transfer chamber and the other chambers (i.e. the loadlock system and the two STM chambers). Typically, the pressure in the transfer chamber is 1×10^{-8} mbar.

A new component added to the transfer chamber in the course of these studies, is a tip-sputtering system. This system consists of a Riber[55] sputter gun, which is used to sputter the STM tip with argon ions along the axial direction. A wobble stick is installed to pick up the STM scanner from the transfer system and to put it in front of the sputter gun. The sputter gun is aligned such that the 5 mm diameter ion beam hits the tip from the front. This method is used to clean the tip mildly, typically after experiments involving gas exposure.

The main STM chamber

The main chamber of the setup is equipped with a number of components that are listed in the PhD thesis of M.J. Rost[51]. Here, we list the most important components and those that have been added or modified during the work described in this thesis.

The base pressure of the chamber was most of the time below 1×10^{-11} mbar.

Turbomolecular pump A Pfeiffer[53] TCM 180 magnetically levitated 170 l/s pump is used to reach high vacuum and to pump during gas exposure. When high-resolution is aimed for, it is possible to turn off the pump without venting it.

Ion pump A 4101/s Varian[56] Starr Cell ion pump is used especially for the low-pressure range and during high-temperature experiments.

Pressure Gauge The Varian[56] Bayard-Alpert Ion Gauge is now equipped with a UHV-24p, able to record pressures down to 7×10^{-12} mbar. The pressures listed in this thesis are not corrected for specific sensitivities to different gasses.

Sputter gun A differentially-pumped ion sputter gun from Specs[57] (IQE 12/38) is used in combination with a Wien filter to bombard the sample with 800 eV Ar^+ ions perpendicularly. The sputter gun is programmed to scan a square grid in order to optimally sputter the sample with a focussed beam. A typical sputter current measured through the sample was 220 nA.

As a transfer and loadlock system are used to exchange samples and STM scanheads, almost no reasons are left to vent the STM chamber. During the experimental work reported in this thesis, the STM chamber was vented and baked-out only once.

An additional, small STM chamber

A new vacuum chamber was added to the transfer chamber, which contains a second programmable temperature STM. It will contain only an STM, an ion sputter gun and an electron gun. The design of this chamber is kept very simple, which makes that this part of the system is expected to be even more stable and easier to use.

Gasses

The main source for the graphene synthesis in our experiments was ethylene gas. A 3.5 N purity high pressure gas bottle was purchased from Aldrich[58]. In order to grow the graphene by CVD, the substrate was exposed to ethylene via a leak valve.

Other gasses used for sputtering and annealing were 5.0 N Argon, 5.0 N Hydrogen and 5.0 N Oxygen bought from Messer[59] and packed in 1 L, 12 bar CANgas bottles.

5.2.3 The high- and variable-temperature STM

The STM that was used for the work reported here is the improved programmable temperature STM, which was also used by M.J. Rost, K. Schoots and G. Dong; its properties are discussed elsewhere, properties such as its high-temperature performance[50] and its high-speed capabilities[60]. This STM is situated in the largest vacuum chamber of the setup, which also has ion sputtering, mass spectrometry, Low Energy Electron Diffraction (LEED) and Auger electron spectroscopy facilities. Also, in this vacuum chamber, the sample can be exposed to precursor gasses, such as ethylene, in order to grow graphene by CVD. The uniqueness of the STM is its capability to allow the user to keep a specific area of the substrate in view during a substantial temperature variation of up to hundreds of Kelvin. In the work reported here, the STM was used in a temperature range from 298 to 1250 K. Typically, during an experiment, the STM was scanning the surface while the temperature was being increased. In this way, properties like the mobility and decomposition of deposits on the iridium substrate surface could be studied as a function of temperature.

An additional, special feature of the STM is its possibility to scan fast. This allowed us not only to scan at video rate (not used in the work reported here) but especially to realize high tip speeds and data rates. The core of this facility is in the analog scan generation combined with fast feedback control. We used a home-built pre-amplifier with a bandwidth of 50 kHz. All these components together allow the user to scan large areas at relatively high frame rates. For example, typically a $500 \times 500 \text{ nm}^2$ surface area was scanned in 512×512 pixels in only 30 s.

The temperature of the substrate was measured via a K-type thermocouple that was welded directly to the surface using a laser spot welding technique. In this way, the true temperature of the substrate was measured and a systematic error in the temperature reading was minimized.

5.3 Methods

5.3.1 The substrate: Ir(111)

Although copper is the most popular substrate for large-scale production of graphene, in our work this material was not chosen. The main reason for this choice is that the vapor pressure of copper is too high: at a typical temperature for graphene synthesis (1325 K) copper atoms are leaving the substrate at a rate of approximately 200 monolayers per second[44]. This condition makes it impossible to scan at.

A good alternative is an iridium substrate. Like copper, it is a transition metal that catalyses the cracking of hydrocarbons into smaller components. Another property that both copper and iridium share is the low carbon solubility: this is a useful property for uniform monolayer growth of graphene layers. Unlike rhodium and ruthenium, no attention has to be paid to carbon segregation from the bulk e.g. when cooling down from graphene synthesis conditions[46, 61, 62]. Finally, the system graphene on iridium exhibits a superstructure that is visible at the nanometer scale. This so-called moiré pattern relaxes the requirement of atomic resolution. Atomic-scale defects in the graphene lattice are directly visible in the moiré pattern. More information on the moiré pattern is given further on in this chapter.

For the substrate, an Ir(111) crystal was purchased from Surface Preparation laboratory[63]. It had been aligned within 0.1° of the (111) orientation (using Laue and $\theta - 2\theta$ X-ray diffraction) and cut in the right shape to fit in our STM sample holder ($4.8 \times 4.8 \times 1 \text{ mm}^3$). Finally, it was polished mechanically. Halfway the experimental period, the sample has been re-polished due to thermocouple material that was found to be present on the crystal surface. This contamination was caused by an accidental exposure of the sample to a very high temperature ($> 1300 \text{ K}$) that allowed the thermocouple material to distribute itself partially over the iridium surface.

5.3.2 Sample preparation

The iridium single crystal was cleaned by cycles of argon sputtering, annealing in oxygen and hydrogen and finally flashing to high temperature in UHV. These steps will quickly be discussed here.

Argon ion sputtering was performed for about 50 min. This resulted in the removal of approximately 5 ML (assuming a sputter yield of 1). Sputtering was mainly used to remove surface contaminants and to damage graphene islands after a graphene-growth experiment. The latter is necessary in order to facilitate the removal of carbon during the oxygen and hydrogen treatments.

In case large amounts of carbon were expected to be present, the system was exposed to oxygen. However, iridium reacts with oxygen more strongly than e.g. rhodium. In the temperature range of $870 - 1000 \text{ K}$, iridium is known to be converted to $\text{IrO}_2(\text{s})$ when oxygen is present[64–66]. Around 1370 K , the IrO_2 present on the surface will decompose or gaseous IrO_3 might form. This means that one should be careful when oxygen is brought into contact with iridium at high temperatures.

In our work, we exposed the surface to oxygen at room temperature

(typical exposure of 10 L), followed by a slow, 10-minute temperature ramp to 870 K in oxygen. In order to prevent the heating filament to break, the oxygen partial pressure was limited to 5×10^{-8} mbar during high temperature exposures.

The removal of residual hydrocarbons and oxides was performed by a hydrogen gas treatment after the oxygen exposure. This should result in the removal of both residual contaminants. We typically exposed our iridium sample to a 5×10^{-8} mbar partial pressure of hydrogen at a temperature of 1200 K for 10 min.

Each cleaning cycle was completed by a short (1 min) flashing of the sample to 1400 K in UHV. The pressure typically stayed below 1×10^{-9} mbar during this treatment. The high temperature was applied in order to remove residual oxide and argon that was implanted in the sample (see below). Additionally, the iridium surface was smoothed by the high-temperature step, resulting in wide terraces and clean, straight steps.

Before each experiment, the condition of the Ir(111) surface was checked by STM at room temperature. Special attention was paid to iridium terrace edges, as contaminants typically accumulate there and affect edge shapes. Cleaning was continued when contaminants and pinning sites were observed at the steps.

As a consequence of the normal-incidence bombardment of the surface with Ar^+ ions, a fraction of the argon can be implanted in the near-surface region. Indeed, sometimes residual subsurface argon was left after cleaning. This showed up in the STM images as local protrusions of the surface, as argon inclusions deformed the lattice[67]. The possible impact of the argon bubbles on our experiments was checked every time. Although the argon bubbles can act as nucleation sites, their density was sufficiently low (< 1 bubble/900 nm²), that a significant influence on our analysis can be excluded.

5.3.3 Tip preparation

STM-tips were etched electrochemically from a 0.25 mm diameter tungsten wire. After etching, the tip was cleaned in an ultrasonic bath in acetone, ethanol and iso-propanol and then dried with nitrogen gas. In the loadlock system the scanner and the tip were baked out at a temperature of approximately 150 °C. Then the scanner was transferred from the loadlock chamber, via the transfer chamber to the STM chamber, where it was positioned over the sample, with the tip positioned over a corner of the sample with a few tens of micrometers distance in between tip and sample. In this configuration, the tip was cleaned in argon by a self-sputtering tech-

nique[68]. If desired, the tip was mildly cleaned by a head-on sputter gun, placed in the transfer chamber (see Section 5.2.2). This last step was typically applied after STM experiments involving exposure to hydrocarbons.

5.3.4 Imaging graphene on Ir(111) by an STM

In general, through the tunnelling current, the STM probes the local density of electronic states (LDOS) rather than a geometrical height of the features directly below the tip. As a consequence, the apparent height recorded by an STM in constant-current mode cannot be interpreted as a mere topography map of the surface in case the LDOS is not uniform over the imaged surface. The tunnelling properties and, hence, the imaging can also be affected strongly when the very end of tip apex has changed in composition, e.g. by a molecule that was picked up from the surface. In the current case of an iridium surface with carbon or graphene on it, the LDOS is indeed not uniform[69, 70]. Hence the apparent height and the contrast in the moiré structure are sensitive to the tunnelling voltage. Due to this effect, a direct interpretation of the images in terms of geometrical height contours would not be justified. In our work, the effects that might be caused by a differences in the LDOS or the tunnelling voltage are mentioned every time, in case they might influence our analysis. Typically, we have avoided to base our interpretation on absolute heights of the observed nanolayers measured in different experiments. For example, the interpretation of the analysis presented Figure 6.8 is based on the change of distribution of apparent heights of clusters imaged in one image, which is not dependent on the absolute heights of the observed clusters.

5.3.5 Interpretation of moiré patterns

The lattice mismatch between graphene and the Ir(111) surface results in a so-called moiré pattern[69]. These patterns, which typically have a lattice parameter of around 2.5 nm, have both a physical and a chemical origin due to the binding of graphene to the iridium substrate[70]. As a consequence, they are easily observable by STM. A major advantage of these patterns is that they provide us indirectly with atomic resolution on the graphene overlayer, also in cases where noise or poor tip quality would prevent true atomic resolution.

In our research group, work was done previously on the appearance of the moiré patterns by Dong[71]. As that work contained a minor, yet essential inconsistency in the labelling, a compact derivation of the moiré rotation angle and its lattice constant is given here for the case of graphene

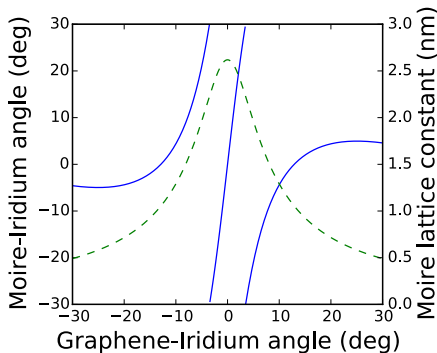


Figure 5.1: Two properties of the moiré pattern plotted as function of the angle between the graphene and iridium lattices. The solid, blue line represents the angle between the moiré pattern and the iridium substrate, calculated via Eq. 5.2. The dashed, green curve represents the lattice parameter of the moiré pattern, calculated via Eq. 5.3.

on Ir(111).

One of the primitive reciprocal lattice vectors of the moiré pattern, \vec{k}_m , can be computed directly from primitive reciprocal lattice vectors of both the graphene overlayer, \vec{k}_{gr} , and the iridium substrate, \vec{k}_{ir} :

$$\vec{k}_m = \vec{k}_{gr} - \vec{k}_{ir} \quad (5.1)$$

Using this construction, we can calculate several observables based on the geometrical situation. For this, we introduce the angle between graphene and iridium, α_{gr} , the angle between the moiré pattern and the iridium substrate, α_m and the lattice parameters of graphene, d_{gr} , iridium, d_{ir} and the moiré pattern, d_m . Following the derivation in the thesis of Dong, but now with correct labels, the angle between the iridium and the moiré pattern is obtained via

$$\alpha_m = \arcsin \frac{d_{gr} \sin \alpha_{gr}}{\sqrt{d_{gr}^2 + d_{ir}^2 - 2d_{gr}d_{ir} \cos \alpha_{gr}}} \quad (5.2)$$

and the moiré lattice parameter is

$$d_m = \frac{d_{gr}d_{ir}}{\sqrt{d_{gr}^2 + d_{ir}^2 - 2d_{gr}d_{ir} \cos \alpha_{gr}}}. \quad (5.3)$$

As the graphene-iridium system is six-fold symmetric, the parameters of the moiré pattern are fully described by plotting them as a function

of the graphene-iridium angle over an interval from -30° to 30° . The result is presented in Figure 5.1. An analogous treatment for the case of graphene on rhodium results in a qualitatively almost identical graph, with only minor quantitative differences due to the small difference in lattice constant between iridium and rhodium.

Chapter 6

Graphene nucleation on Ir(111)

In the process of graphene synthesis, knowledge on the precise conversion of hydrocarbons into graphene is crucial not only for understanding but also for optimizing the synthesis mechanism. Real-time studies focussing on the growth of graphene are required to reveal the critical parameters for the growth of a perfect nanolayer of graphene. In the work reported here, our variable-temperature STM was used to study the evolution of an Ir(111) surface that was exposed to ethylene. While the temperature was increased, the surface was followed at the nanoscale in order to characterize the behaviour and appearance of the deposited hydrocarbons until they converted into graphene. The results show that graphene nucleates from carbon-containing clusters preferably at iridium steps. In spite of the observed graphene formation, we don't observe significant mobility of the primary carbon clusters. This suggests that the required rearrangements of the carbon layer are taking place on an even smaller scale, possibly atom by atom. The majority of the graphene islands is aligned with the substrate very well. Based on the graphene island shapes, we conclude that the smallest stable graphene unit is half of a unit cell of the moiré pattern.

6.1 Experimental approach

As the variable-temperature STM used in this research is capable of following the iridium substrate surface during the full temperature sweep from room temperature up to 1300 K, the conversion of hydrocarbons into graphene can be studied in detail. The experimental data reported in this chapter were all acquired during a similar kind of experiment: first hydro-

carbons (ethylene) were deposited at room temperature and subsequently the substrate was heated slowly in ultrahigh vacuum up to 1000 K or higher, while the substrate was scanned by the STM. In this manner, not only the initial and final structures were observed, but also the intermediate stages of carbon clustering and further rearrangements of the deposit. During these studies no additional carbon was added from the gas phase (except for possible deposition from the residual gas, which was at a pressure below 10^{-10} mbar during the high-temperature stage of the experiment). Further relevant experimental details are provided at the beginning of the following sections.

6.2 Deposition of ethylene at room temperature

In this section the behaviour of ethylene on iridium at room temperature is studied. We pay attention to the possibility of clustering of the ethylene molecules or other rearrangements, since these might be relevant for the nucleation of graphene, at higher temperatures.

After sputtering and annealing, the cleaned iridium surface was inspected by STM. After this characterisation, the surface was exposed to approximately 0.5 L of ethylene gas (1.0×10^{-8} mbar during 50 sec), while the STM tip was retracted (to prevent tip effects). Next, the substrate was studied by STM to analyse the ethylene-on-iridium system at room temperature.

In Figures 6.1a and 6.1b, STM images of the iridium substrate are presented that were recorded before and after the exposure to ethylene, respectively. From these images, it is clear that the exposure to ethylene has no significant influence on the surface topography. In addition to some residual contaminants, a few broad 5 – 10 nm-sized protrusions are visible, which are attributed to argon bubbles, as discussed in Section 5.3.2. No decoration of steps or argon bubbles was observed after the surface was exposed to ethylene. Apparently the deposited hydrocarbons do not cluster and they are too mobile to be imaged. A more careful inspection reveals that both the tunnelling current and the height contours on the terraces exhibit an extra component of high-frequency noise, as a result of the exposure to ethylene. This is illustrated by the two height profiles in Figures 6.1c and 6.1d. This behaviour was observed systematically and can be interpreted as the result of mobile structures on the iridium surface that are incidentally ‘imaged’ when they move precisely underneath the tip.

The tunnelling microscopy results presented here suggest that ethylene deposited at room temperature on Ir(111) results in mobile structures that

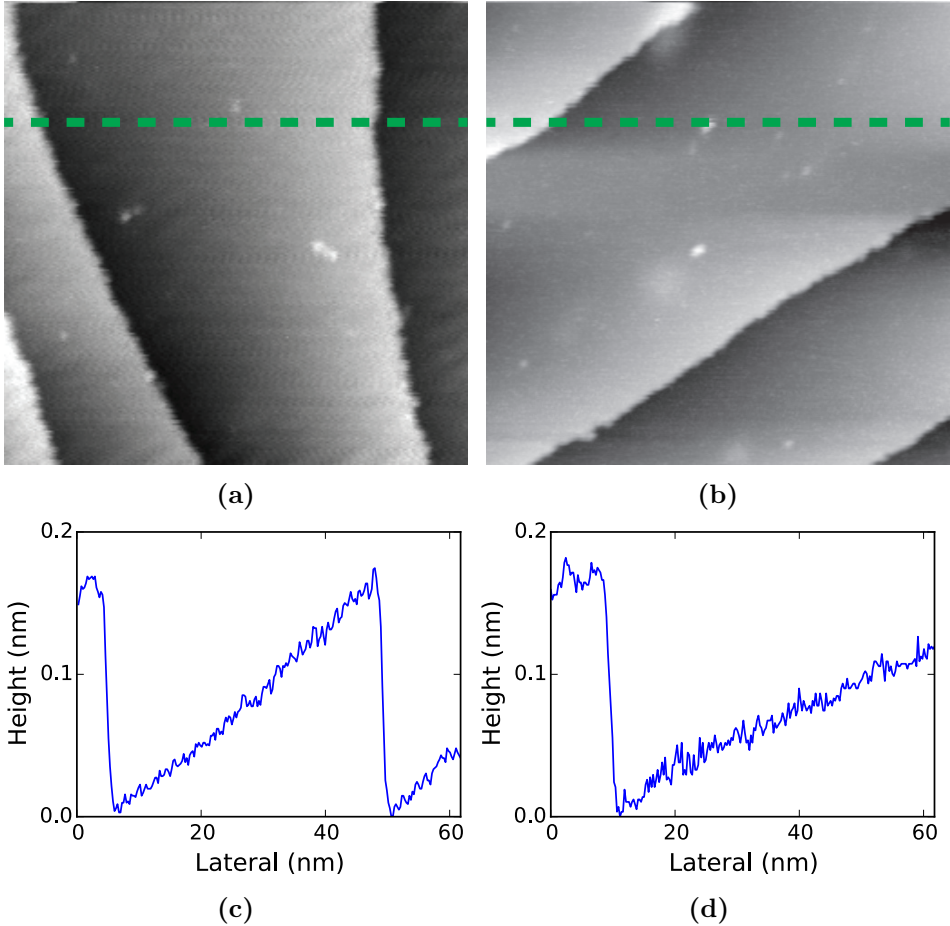


Figure 6.1: The Ir(111) surface imaged at room temperature (a) before and (b) after exposure to 0.5 L of ethylene gas at room temperature. Image size $62 \times 62 \text{ nm}^2$, z-scale 0.25 nm. Sample voltages -0.1 and -0.7 V respectively, tunnelling current 0.1 nA. FFT filtering was performed on the data shown in panel (a) in order to remove a low-frequency vibration. Panels (c) and (d) present height profiles taken at the positions indicated by the dashed, green lines in Panels (a) and (b).

move too fast to be observed by STM. No specific decoration of the iridium terrace edges was observed. Our observations are consistent with the XPS data of Lizzit[49] that seemed to indicate that at room temperature, the ethylene-exposed iridium surface is covered with small (chemisorbed) hydrocarbons, containing only a small (one or two) number of carbon atoms. These species do not cluster at room temperature.

6.3 First observation of carbon clusters

After deposition of ethylene, the iridium substrate was heated up slowly while it was scanned by the STM. In this section we report the first observation of cluster formation on the iridium surface during this temperature ramp.

First, the clean iridium substrate was exposed to 3L of ethylene gas at room temperature. STM images were acquired subsequently, while the iridium substrate was heated at a rate of 0.1 K/sec to a temperature of 800 K. The background pressure was below 1×10^{-10} mbar throughout the entire temperature ramp.

In Figures 6.2a, 6.2b and 6.2c, topographic images of precisely the same area of the iridium surface are shown, recorded at a temperature of 415 K (panel (a)) and 458 K (panels (b) and (c)). Up to a temperature of 415 K, the observed surface is similar to the situation at room temperature (c.f. Figure 6.1b). Apart from the height noise that was discussed already, the images contain no signs of adsorbates on either the terraces or the steps.

At a temperature of 458 K, the entire iridium surface was covered with small, nanometer-sized clusters that each consisted of a small number of sub-units (see Figure 6.2b). As the surface had been exposed to ethylene at room temperature and the pressure in the vacuum chamber remained in the 10^{-11} mbar regime throughout the entire temperature ramp, these clusters can only originate from the hydrocarbons present on the iridium surface due to the ethylene exposure. The clusters were distributed uniformly over the entire surface, indicating that the nucleation of these clusters is not taking place on ‘special’ sites on the iridium surface, such as steps, kinks or point defects on the terraces.

An analysis of the height of the adsorbates shows that the particles have a typical height of 0.12 ± 0.01 nm. This uniformity suggests that most of the clusters consist of sub-units that have an identical internal structure.

In order to explore whether the cluster configuration was stationary, we compare two subsequent STM images. Figure 6.2c shows the same region on the iridium surface as recorded in Figure 6.2b, 9 sec earlier. These two

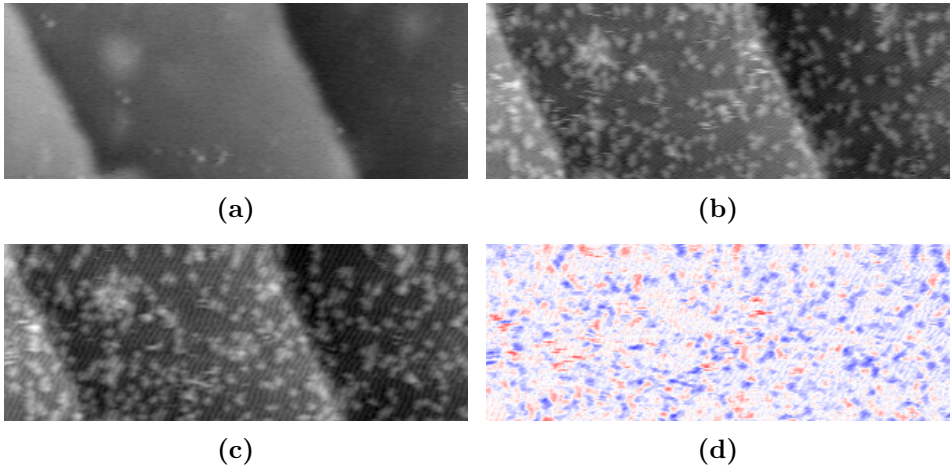


Figure 6.2: (a), (b) and (c): STM topography images of precisely the same iridium surface, recorded at elevated temperature after deposition of 3L ethylene at room temperature. The temperature during the image acquisition was 415 K for image (a) and 458 K for both images (b) and (c). The images (b) and (c) were recorded subsequently with a frame acquisition time of 9 sec/frame. Image size $77 \times 29 \text{ nm}^2$, z-scale 0.52 nm, sample voltage -0.74 V , tunnelling current 0.1 nA. Figure 6.2d: result of subtraction of image (c) from image (b). The blue colour indicates added, the red colour removed material; colour scale (blue-white-red): 0.52 nm.

images are aligned and subtracted from each other using the procedure reported in Appendix C. The result is shown in Figure 6.2d, where the blue areas indicate a positive height change and the red areas a negative change. The colour scale (from full red to full blue) is the same as that for the grey scale of Figures 6.2a, 6.2b and 6.2c, namely 0.52 nm. The resulting map clearly indicates that a significant fraction of the small clusters has changed, indicating that the cluster configuration was dynamic on the timescale of 9 sec, at this temperature. In spite of the mobility that is revealed by Figure 6.2d, the clusters clearly do not merge beyond the level of Figures 6.2b and 6.2c at this temperature. The typical length scales of the observed configurations did not evolve beyond 2 nm. This behaviour suggests that the clusters and their sub-units do not yet have the structure and composition of graphene, but that they rather form diffusion-limited aggregates of molecules that still contain a high concentration of hydrogen.

Summarizing, when the ethylene-exposed iridium surface is warmed up above room temperature, we observe clustering of the deposit at temperatures between 415 and 458 K. We interpret these clusters as aggregates of small hydrocarbon molecules, presumably ethynyl. Even though these molecules are somewhat mobile, they do not merge into larger molecules or into graphene at this temperature.

6.4 Conversion from hydrocarbons to amorphous carbon

In this section we concentrate on the final rearrangements in the overlayer, prior to the formation of graphene. This covers STM observations in the temperature range from 458 to 865 K. The STM image acquisition rate was set to 9 sec per image in the temperature window up to 800 K. Above this temperature, the acquisition rate was 17 sec per image. In order to approach the regime of graphene formation slowly, the temperature ramp was kept at 0.1 K/sec. During the full high-temperature experiment, the background pressure remained below 10^{-10} mbar, which ensured that no significant amount of carbon was added during the experiment.

The mobility of the adsorbates was followed during the entire temperature ramp. At a temperature of 760 K, the images indicate that the clusters were no longer mobile, as can be seen in Figure 6.3. As done for the data shown in the previous section (see Figure 6.2), two subsequent STM images were subtracted from each other. At the same timescale of 9 sec, almost no change of the surface was found. This disappearance of mobility of the adsorbates at a higher temperature of 760 K is attributed to a change in

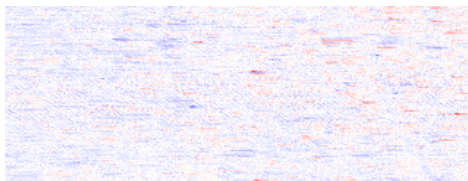


Figure 6.3: Result of the subtraction of two subsequent STM images (time difference of 9 sec) recorded in the same experiment as in Figure 6.2, at a temperature of 760 K. The blue colour indicates added, the red colour removed material; the z-scale (red-white-blue) is 0.52 nm. Image size $77 \times 29 \text{ nm}^2$. The STM images were recorded with a sample voltage of -0.74 V , a high frequency noise component was removed by FFT filtering.

the internal structure of the adsorbates.

A more detailed investigation of the surface was performed at a temperature of 865 K. The STM snapshot presented in Figure 6.4 shows that at that temperature the iridium surface is still covered with a high density of small particles. At this temperature, the clusters do not have one specific height. They are still uniformly distributed and do not cluster significantly. It can be observed that a significant fraction of the step is decorated with particles, although no clear depletion of particles close to the iridium steps is present.

Also at a temperature of 865 K, the mobility of the visible adsorbates was inspected by subtracting two STM images of the same area taken at different times. A set of STM observations is presented in the two upper panels of Figure 6.5. These two observations were done with a 53 sec time period in between. The difference between these two images is shown in Figure 6.5. A clear signal in the differential data is to be expected in case carbon species have moved or disappeared within a timescale of 53 sec. As can be concluded from the two images and from the difference map, the changes are very modest. In particular, they are much smaller than the differences observed on a much shorter timescale at a much lower temperature of 458 K (Figure 6.2). From this we conclude that the clusters observed at 865 K must have a different nature, i.e. a different structure and composition, than those found at lower temperatures.

In addition to the subtraction analysis, another observation that gives information on the mobility of surface structures is their distribution over the surface. In Figure 6.4 no clear clustering of particles can be seen except the almost complete decoration of the iridium steps. This observation suggests that the mobile units have a preference to attach to these steps. The

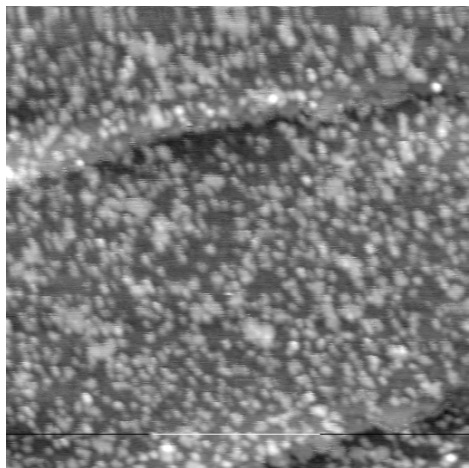


Figure 6.4: STM image of the iridium surface at a temperature of 865 K. Before heating, the surface had been exposed to 3 L of ethylene at room temperature. Image size $125 \times 125 \text{ nm}^2$, z-scale 0.35 nm, sample voltage 3.01 V, tunnelling current 0.1 nA.

observation of non-decorated parts of the steps suggest that the mobility has been too low to completely execute this preferential-attachment behaviour. The absence of a depletion of adislands in the vicinity of iridium steps might indicate that the displacement of the adsorbed material has not been diffusion-, but attachment-limited. Note that this should apply to a lower temperature than 865 K, as the clusters observed at 865 K are completely immobile.

It is instructive to view our results in the light of the high-resolution XPS observations of Lizzit et al.[49]. These results indicated that the ethylene-exposed iridium surface forms ethynyl (C_2H) species above 400 K. Additionally, together with other studies focussing on hydrocarbons on Ir(111), they conclude that hydrocarbons are completely dehydrogenated at a temperature of approximately 800 K[72, 73].

Our STM observations do not only agree with the literature, but also provide new insight in the nature of the adsorbates. Based on the XPS data of Lizzit et al., we expect the adsorbates on the iridium surface at a temperature of 458 K to be mainly ethynyl molecules. Our data shows that clusters of these molecules are mobile and do not merge significantly. This behaviour fits to ethynyl molecules as they are individual compounds with saturated bonds. Hence, a chemical driving force for the molecules to cluster strongly is not expected to dominate.

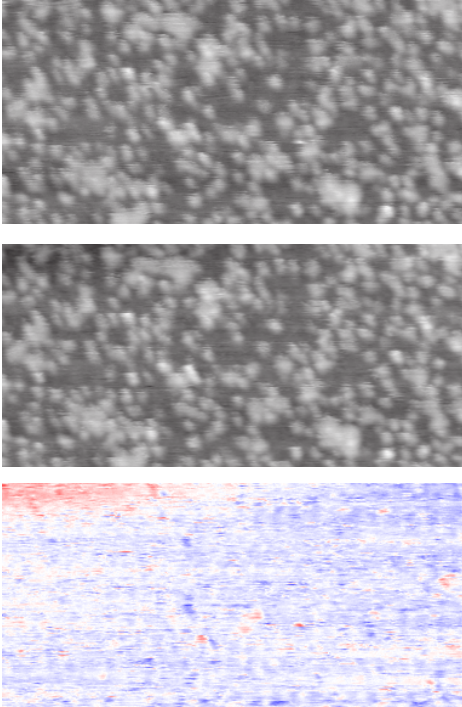


Figure 6.5: Two STM images recorded at the same position on the iridium surface at the same temperature of 865 K with a time period of 53 sec in between. The particles on the surface originate from room-temperature deposited ethylene. The third panel shows the result of image subtraction of the upper two snapshots. Image size $95 \times 45 \text{ nm}^2$, z-scale 0.35 nm, sample voltage 3.01 V, tunnelling current 0.1 nA. In the lower panel, the blue colour indicates added, the red colour removed material; the z-scale (red-white-blue) is 0.35 nm.

In addition, the data we present here, shows that at a sufficiently high temperature of 760 K, the clusters have lost their mobility nearly completely. Correspondingly, the data of refs. [49, 72] and [73] seem to indicate that at that temperature all carbon atoms are completely dehydrogenated and only amorphous carbon compounds are present at the iridium surface.

Summarizing, our results demonstrate that the evolution of the overlayer slows down nearly completely between 458 and 865 K, in spite of the increase in temperature. This is accompanied by a widening of the distribution of heights of the clusters. These observations suggest very strongly that in this temperature interval the composition of the clusters is changing. This conclusion is supported by the high-temperature XPS data of ref. [49] that indicate that at 865 K the overlayer is completely dehydrogenated. We propose that the high-temperature clusters consist of amorphous carbon. We ascribe the reduction in mobility to the increase in interaction between the clusters and the substrate, when the clusters lose their hydrogen.

In the light of high-quality graphene growth, the observed situation on the iridium surface at a temperature of 865 K is not very positive. In case the observed high density of small clusters does not evolve to a few large clusters, and in case the graphene into which the observed clusters might convert does not have a uniform orientation, the resulting graphene overlayer will contain a high density of domain boundaries. Instead of room-temperature exposure of the iridium surface to ethylene, high-temperature deposition of hydrocarbons might result in higher-quality graphene. This procedure was suggested already by previous studies of graphene on rhodium, performed in our research group[46].

6.5 Lowest temperature of graphene nucleation

The first conversion events from carbon clusters into graphene islands on iridium was followed in *real time* by STM while the substrate temperature was increased slowly (< 0.1 K/sec) from 865 to 1001 K. The slow temperature ramp allowed us to study both the lowest graphene nucleation temperature and the kinetics involved. The design of our STM is such that even over the enormous temperature ramp, the surface could be imaged continuously without interruption. However, residual drift especially in the lateral direction still does have a minimal distortional effect on the imaging quality, e.g. causing straight steps to show up curved in the image and circular islands to show up as curved ellipses. As this lateral drift changes on the timescale of seconds, it makes both a detailed, quantitative analysis of individual images and an analysis by comparing several images recorded

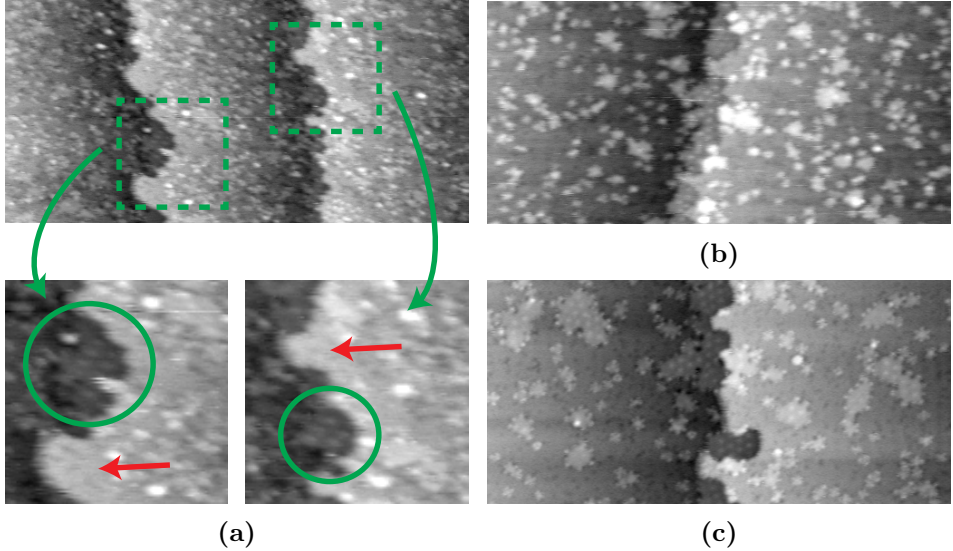


Figure 6.6: STM images of iridium recorded at (a) 967 K, (b) 995 K and (c) 1001 K, after exposure to 3 L of ethylene at room temperature. Two close-ups of the first image are presented to highlight the moiré patterns present (green circles) and to indicate areas without clusters at the iridium steps (red arrows). Image size $125 \times 60 \text{ nm}^2$, z-scale 0.26 nm, sample voltage 3.06 V for images (a) and (b), 2.73 V for image (c), tunnelling current 0.1 nA.

during a temperature ramp rather complicated. Nevertheless, as drift in the z-direction can be corrected using line-by-line linear background subtraction and the iridium surface can be used as a reference, we can perform detailed data analysis based on the recorded heights of the clusters on top of the iridium.

In the following paragraphs, the conversion of the clusters into graphene is discussed based on the observations made by our STM. The structure of the discussion is based on the temperatures at which clear changes in the adsorbates were observed.

$T = 967 \text{ K}$ Figure 6.6a presents the situation at the iridium surface at a temperature of 967 K. Although the image contains some in-plane drift, clear structure changes with respect to the observation at $T = 865 \text{ K}$ can be noticed. These changes are concentrated at the iridium steps. In order to help the reader, two areas are magnified and presented in Figure 6.6a. Two cases are highlighted in these panels: the red arrows indicate protruding

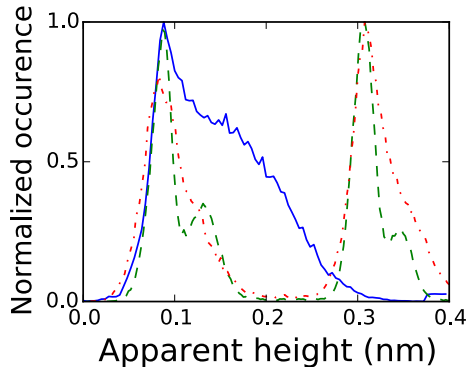


Figure 6.7: Distributions of the apparent heights of the STM images recorded at different temperatures. The blue, solid line corresponds to the STM image shown in Figure 6.5 (upper panel), recorded at a temperature of 865 K. The red, dash-dotted curve represents the data of the STM image shown in Figure 6.6a recorded at a temperature of 967 K and the green, dashed curve corresponds to the STM image presented in Figure 6.6c, recorded at a temperature of 1001 K. The data was corrected by a local plane fit in order to level the terraces.

iridium steps that do not have carbon clusters on top; the green circles indicate patches attached to the lower side of a step with a clear moiré pattern. The presence of the moiré pattern in a patch is direct evidence that the deposit has adopted the structure of graphene: the pattern is a result of the two incommensurate hexagonal lattices of iridium and graphene on top of each other. This gives direct evidence for the presence of the first graphene nuclei to have formed at or below a temperature of 967 K.

In order to characterize the clusters more, a distribution of the heights measured by the STM is presented in Figure 6.7. In this graph, the red dotted curve represents the distribution of the apparent heights of all pixels of the image shown in Figure 6.6a. For comparison, the distribution belonging to the observation recorded at a temperature of 865 K (see the upper panel of Figure 6.5) is shown by the blue, solid line. As the bias voltage of those two observations differs by merely 0.05 V, we attribute the change in the width of the distribution of heights to a change in composition of a significant fraction of the clusters present on the iridium surface. In spite of this change in the distribution, it is not possible to characterize the clusters present at the surface by a specific apparent height. Nevertheless, the upper limit of this height has reduced from 0.2 ± 0.02 nm to 0.06 ± 0.02 nm.

$T = 995 \text{ K}$ A further increase of the temperature up to 995 K leads to evident changes at the steps, as can be seen in Figure 6.6b. The elapsed time between the data presented in the Figures 6.6a and 6.6b is 929 sec. A first, remarkable change is that almost the complete iridium step is decorated with a rim of material. Closer inspection shows that this material exhibits moiré patterns, which indicates that this material is graphene. Second, even though the rim clearly indicates that carbon has accumulated near the iridium steps, we observe no depletion of the clusters on the terraces near the steps. This proves that the carbon material that has been added to the graphene at the iridium steps originates not only from the nearby carbon islands, but from all over the iridium terrace. From this, we can conclude that the redistribution of carbon must rather be an attachment-limited process[74].

$T = 1001 \text{ K}$ After a modest, further temperature increase to 1001 K and a relatively long waiting time of 2079 sec after the last image recorded at 995 K, the appearance of the carbon patches has changed significantly as can be seen in the STM-image in Figure 6.6c. In this image, almost all clusters that lie on the substrate have acquired an identical edge structure and most of the smaller islands have adopted a triangular or hexagonal shape. Also, almost all larger clusters exhibit a clear moiré pattern.

The distribution of heights of the STM image shows a remarkable change, as can be clearly observed in Figure 6.7. The red, dash-dotted curve represents the heights observed in Figure 6.6c. At each terrace, the distribution has split into two peaks, one corresponding to the iridium terrace, and the other to the clusters present at the terrace. Apparently the height of all clusters has become identical, namely $0.045 \pm 0.005 \text{ nm}$, which suggests that they consist out of one specific structure. These observations indicate that at a temperature close to 1000 K all carbon clusters have transformed into well-defined graphene patches, some of which form extended rims along steps on the iridium surface. In the next chapters we will inspect the properties of the graphene that is forming on the iridium substrate, such as its mobility and its island size distribution. Here we concentrate further on the nucleation stage.

The observations presented in Figure 6.6 show a clear preference of graphene to nucleate at a substrate step prior to forming out of carbon clusters on the iridium terrace. This preference can be explained in two ways: first, the carbon atom concentration at steps is higher because of the reduced coordination of atoms at a step, which directly results in a reduction of the free energy of the atoms that get trapped at such a step.

Second, the iridium step might act as a template (in the in-plane direction) for graphene nucleation. The first effect increases the attempt frequency of carbon atoms to nucleate into graphene. The second effect reduces the barrier to form a graphene island at an iridium step with respect to the formation of an island on a terrace.

The absence of a depletion zone of carbon close to the graphene-decorated iridium step shows that there is a net transport of carbon atoms to the iridium step from all over the terrace. This behaviour indicates that the growth of the graphene islands is not limited by carbon diffusion over the terraces, but by the rate of carbon atoms/building units attaching to the graphene. Further investigation of the diffusion and attachment of carbon units in the graphene-iridium system is discussed in Chapter 8.

6.5.1 Analysis - graphene nucleation at terraces

In the previous section, the observation by STM of the conversion of carbon clusters into graphene was presented. Most of the data was discussed in qualitative terms and the discussion was focussed mainly on the iridium steps. But evidently, in addition to the carbon at the steps, the clusters on the iridium terraces have changed into graphene also. To obtain quantitative insight in the evolution of all the carbon clusters present, the STM data was processed by the island-extract algorithm described in Appendix D. The resulting ‘image mask’ was used to obtain the radius and the average height of each island. As all islands have different, complicated shapes, the radius is calculated by first measuring the island area, A , and applying the relation $A = \pi r^2$ (the islands are treated like perfect circles). In this way a ‘nominal’ radius can be estimated. Figure 6.8 presents the average heights of the islands as a function of their radius and a histogram of the island radii, for all three STM images shown in Figure 6.6. The vertical dashed lines indicate the average island radii.

The statistical analysis of the island evolution quantifies the increase in average island size and provides useful additional insight, for example via the statistical variance of the measured heights. The distributions in Figure 6.8 confirm the qualitative observation of the increase in island size with temperature. This is evident from the increase in average island size (note the vertical dashed lines). It is also reflected in the histograms that show a reduction in the number of small islands combined with an increase in the number of larger islands at higher temperatures (995 and 1001 K). Both aspects are a direct consequence of the ripening mechanism that is at work. This will be discussed in Chapter 8.

Let us now turn to the statistical variance in the observed heights of

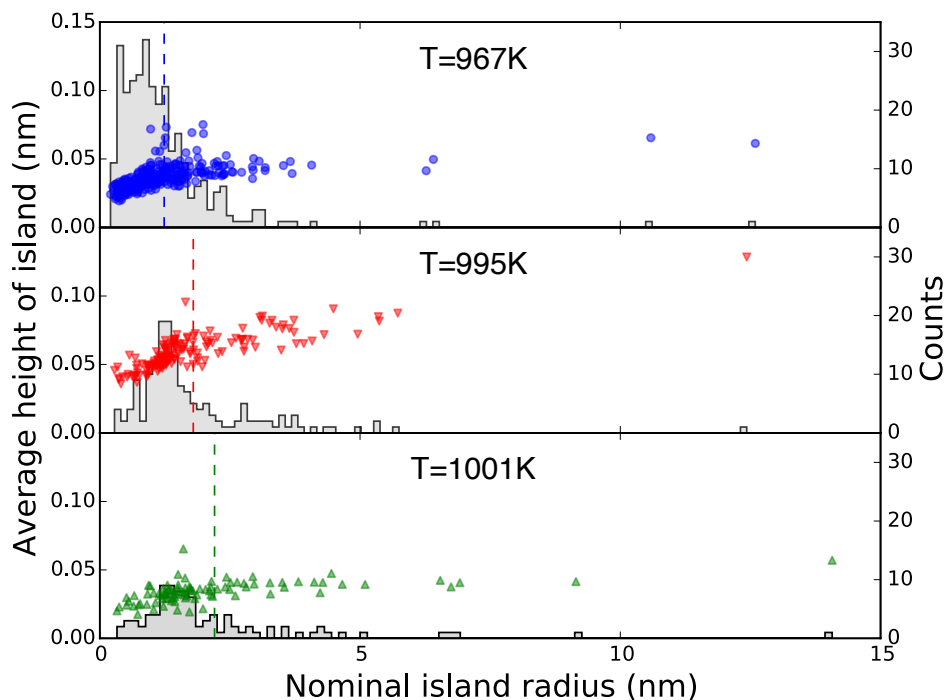


Figure 6.8: Observed distribution of nominal radii (histograms) and heights (symbols) of the islands in the STM images of Figure 6.6 at 967 K (top panel), 995 K (middle panel) and 1001 K (bottom panel). At each temperature, the dashed vertical line indicates the average island radius. The nominal radius of each island was obtained from the island’s area, assuming a perfectly circular shape. The island area was obtained by use of the island-extraction algorithm, described in Appendix D.

the islands. In Figure 6.8, we see that the measured height values exhibit significantly less statistical scatter at a temperature of 995 K than at 967 K. The scatter is reduced even further at 1001 K. At each of these temperatures, the scatter in the observed heights is well beyond the accuracy of 0.005 nm, with which the island heights are determined from the STM images. The reduction in the height variance suggests that the islands increasingly adopt a single, well-defined structure as the temperature is raised. A straightforward interpretation is that at 1001 K all patches have converted into graphene: as the graphene nanolayer on top of iridium has a well-defined corrugation, the average height of all larger islands should be identical and no scatter should be present. This is precisely what we find in Figure 6.8. Additionally, this interpretation is corroborated by the transformation in the STM images over the temperature range up to 1001 K of all islands into highly uniformly shaped structures. For, as can be observed in Figure 6.8, both the shapes and the corrugations of all island present are identical. Also the changes observed in the high-temperature XPS spectra of Reference [49] that have been interpreted in terms of a significant transition of the character of the carbon-carbon bonds into that of graphene, are supportive of our conclusion.

The analysis of the islands, presented in Figure 6.8 does not only show an increase of the average island size as function of temperature, but also a remarkable levelling of the average height of the larger islands at 1001 K. This behaviour is visible in the green curve of Figure 6.7, where the emergence of a separate peak belonging to the clusters indicates that they exhibit a uniform height of 0.045 ± 0.005 nm. The distribution in Figure 6.8 shows that at a temperature of 1001 K the islands with an island radius larger than 1.5 nm have adopted this height.

6.5.2 Discussion

At $T = 1001$ K, the average height of all islands reaches its maximum value only at an island radius of approximately 1.5 nm, i.e. somewhat beyond the radius of 1.3 nm of the unit cell of the moiré pattern. The smaller islands, with radii between 1.0 and 2.0 nm, are on average lower and exhibit more scatter in their height values than larger islands. The origin of this scatter is revealed, when we look in more detail at islands with sizes of approximately one moiré unit; see e.g. Figure 6.9. In this image, units are visible that have similar, triangular shapes. Also larger structures appear that consist of two such triangular units, that appear to act as the building units of the graphene islands.

The triangular shape and the size regime of many of the smaller is-

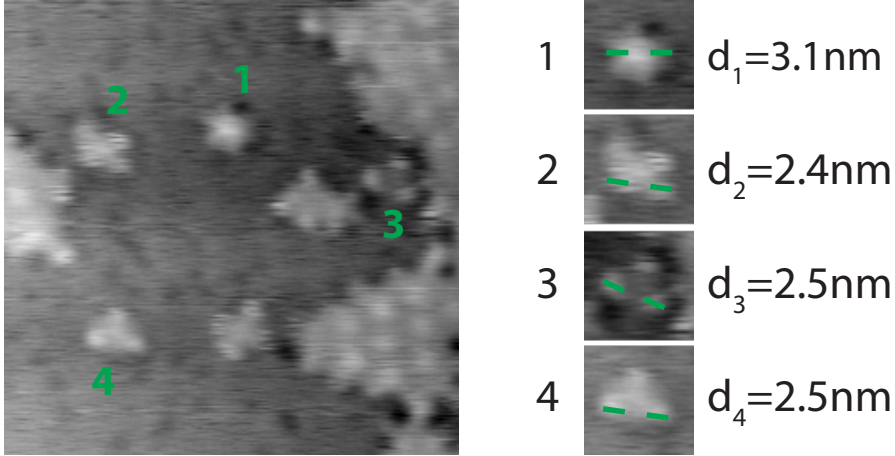


Figure 6.9: STM image of the iridium surface covered with graphene islands, recorded at 1014 K. Some islands are magnified to bring out the differences in orientation with respect to the substrate. Each orientation results in a specific apparent height of the graphene island and in a specific shape of the smallest stable unit of graphene. Image size $30 \times 30 \text{ nm}^2$, z-scale 0.13 nm, sample voltage 2.73 V, tunnelling current 0.1 nA.

lands suggest that they are related to the moiré pattern of graphene on iridium(111). Figure 6.9 supports this with measurements of the distances between the corner protrusions of these islands. The corners of islands 2 and 4 in Figure 6.9 are aligned nearly perfectly with the iridium substrate lattice and their distances are $2.5 \pm 0.1 \text{ nm}$, in good agreement with the period of the moiré pattern of 2.46 nm. The distances of the corners of island 3 are in agreement with the period of the moiré pattern as well. The shape of island 2 is a rhomb, which is identical to the unit cell of the moiré pattern. Looking at the triangular shape of islands 3 and 4, we suggest that these triangular units are half moiré units and are the smallest stable building blocks of the graphene islands with this orientation. This behaviour is understood better when the registry of graphene on iridium is taken into account. As the influence of the registry is more pronounced during graphene growth, it is discussed in Chapter 7 in more detail. Here, we leave the discussion after noting that the triangular sub-units of the moiré unit cell are assumed to be the part of the unit cell in which the carbon atoms of the graphene align best on the iridium substrate. Island 1 is different. It has a hexagonal shape, has a different orientation and has less pronounced corner protrusions, which makes that its size is more difficult to measure accurately.

As discussed in Section 5.3.5, the orientation and period of the moiré pattern between the graphene overlayer and the iridium substrate depends sensitively on the precise relative orientation of the two lattices. This naturally explains the small differences between the islands in Figure 6.9. For example, islands 2 and 4 are perfectly aligned with the iridium, while island 3 seems to be rotated by 18.5 ± 1.5 degree. We interpret the observed rotation of island 3 as the rotation of its moiré pattern, since the rotation is read off from the positions of the corner maxima, which we associate directly with the moiré pattern. Calculating back from Equation 5.2, a rotation of the moiré pattern by 18.5 degrees should correspond to a physical rotation of the island by 2 degrees. Using Equation 5.3, we find that the period of the moiré pattern should be still almost at its maximum value of 2.46 nm, which is consistent with the distance between the corner maxima of island 3 in Figure 6.9. Island 3 also has a somewhat different apparent height, 20 ± 5 pm instead of 60 ± 10 pm, which fits the description given above. We find that the aligned configuration is the most occurring orientation, which indicates that this is the energetically most favourable orientation, as was observed also in refs [75, 76]. The hexagonal shape of island 1 and its deviating internal structure indicate that the orientation of this island is far from that of islands 2, 3 and 4. We have not observed smaller islands of this orientation, which indicates that the hexagonal structure is the smallest stable structure for this island orientation. It is remarkable that the energy landscape belonging to this other orientation has a dramatic impact on the shape of the smallest, moiré unit sized island.

It might be valuable to note here that the higher parts at the edges of the graphene patches do not have to be those maxima, which are visible in the moiré structure in large graphene islands. The higher parts seem more likely to be electronic edge structures that are related with the growth behaviour of graphene. As mentioned in Section 5.3.4, the non-uniform LDOS affect the height values in our STM data. However, both the shape of the islands and the moiré pattern are still genuine parameters for analysing the islands. Also the analysis of the height data as presented in Figure 6.8 is not deteriorated as this analysis focusses on a relative behaviour of the island height distributions. Further, although the edges of the graphene islands are affected by local changes in the LDOS, these edges still do reflect the moiré periodicity and they can be used to characterize the islands. This will be discussed in more detail in Chapter 7, where the edge behaviour is studied in the light of graphene growth.

The results presented here have remarkable parallels with the work reported by Lacovig and Lizzit [49, 73]. They calculated by DFT, based on

high-resolution XPS data, that the transformation from carbon to larger graphene units follows a particular route with intermediate dome-shaped phases with different heights caused by the binding of the graphene to the iridium only at the perimeter. The height of these dome-shaped graphene islands reaches the graphene height of full-coverage graphene already at dome-radii half of the moiré unit radius. Their work fully supports both our observations and our analysis.

Summarizing we conclude that hydrocarbons deposited on Ir(111) at room temperature, start to convert to graphene at 967 K at iridium steps. During this process the carbon concentration at the iridium step increases. Based on the absence of a depleted zone, close to the steps, we conclude that this process is not diffusion limited. At a temperature of 1001 K all carbon clusters both at steps and on the iridium terraces have converted into graphene. The graphene islands show different sizes and rotations on the iridium substrate, however, one orientation is dominating. The minimum size of the islands is, depending on its orientation, half a moiré unit (a triangle) or one complete moiré unit.

6.6 Summarizing conclusions

During the annealing of an iridium (111) surface, after a room temperature exposure to ethylene, we observed several structural rearrangements, before the adsorbate layer is finally converted into graphene at a temperature of 967 K. The real-time observation of the surface with our variable-temperature STM shows that mobile adsorbate clusters formed around 400 K transform into carbon clusters with an extremely low mobility at temperatures up to 967 K. At that temperature, clusters exhibiting moiré patterns appear at iridium steps, indicating the first nucleation of graphene. In spite of the preference of nucleating at steps, no depletion of carbon at the iridium terrace close to the step is observed, indicating that the carbon transport is not diffusion limited. Further annealing to 1001 K leads to an iridium surface only decorated with moiré-pattern containing structures of uniform height, from which we conclude that all carbon has converted into graphene. The increase in temperature also leads to an increase in average island size the graphene clusters. The moiré patterns present in the islands indicate that, at 1001 K, most graphene islands are perfectly aligned with the substrate. Based on the typical shapes of these islands, it can be stated that half moiré units of graphene are the smallest stable configuration of graphene at a temperature close to its nucleation temperature.

Chapter 7

Graphene growth

The growth of graphene is followed at the sub-moiré-unit level, using our variable-temperature STM. At a temperature of 1180 K the growth of graphene on Ir(111) was followed in real time by looking at one graphene island for approximately 1000 sec. The resulting data gives new insight in how new units of graphene are added to the existing island and shows which growth mechanisms are preferred. The alignment and local interaction of graphene with the iridium surface appear to play a decisive role during graphene growth.

7.1 Experimental observation of graphene island evolution

In order to investigate the mechanism of graphene growth on Ir(111) *in situ*, we required a small amount of carbon on the surface. Rather than to deposit this amount explicitly, we made use of the small, residual carbon coverage, below 0.05 ML, that was remaining at the surface after a small number (4) of sputter cleaning and annealing cycles. Subsequently the temperature was raised and, starting from a temperature of 1000 K, the surface was followed by STM continuously while the substrate was slowly heated up to 1300 K with a ramp of approximately 0.05 K/sec. The background pressure in the vacuum chamber remained below 1×10^{-10} mbar at a substrate temperature of 1000 K and increased up to 1×10^{-9} mbar at 1300 K. During the experiment, no gas was introduced in the vacuum chamber.

A sequence of observations capturing the growth process is presented in Figure 7.1. During this sequence, a graphene patch was followed for approximately 1000 sec at a temperature of 1180 K. The temperature was kept constant for this period of time. As no carbon was added during

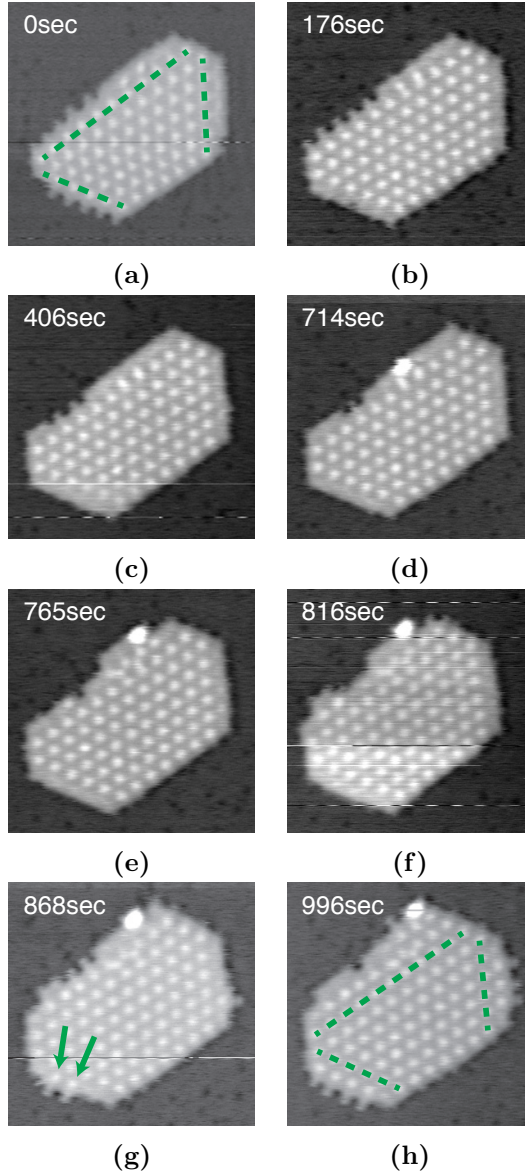


Figure 7.1: Image sequence of a graphene island recorded at 1180K, showing the mechanism of graphene growth. The elapsed time relative to the first image is indicated in the top left corner of each image. At the moment these images were recorded, the background pressure was below 1×10^{-10} mbar. Any carbon that attaches to the graphene island is coming either from the residual gas, or from the substrate, or from other graphene islands present at the iridium surface. Image size $36 \times 36 \text{ nm}^2$, z-scale 0.25 nm, sample voltage 3.50 V, tunnelling current 0.1 nA.

this experiment deliberately, all growth observed here must be due either to ripening of the ensemble of graphene patches on the surface or to the attachment of residual carbon, segregating from the interior of the iridium or arriving from the residual gas. This lets the graphene island grow slowly and allows us to investigate the graphene growth mode in detail.

7.1.1 Active edges

A remarkable, first observation from Figure 7.1 is that only 3 out of the 6 edges of the graphene island exhibit growth. These three edges are indicated by dashed, green lines in panels (a) and (h) of Figure 7.1. This results in a reduction of symmetry from the 6-fold symmetry of graphene to a 3-fold symmetric system. The breaking of this symmetry is discussed further in the next section.

The final growth shape of a 3-fold symmetric island should be a triangle. This triangular shape is almost never observed, which suggests that the difference in activation energy for adding graphene is minimal for the two sets of edges. In typical experiments, this small difference in energy will not be observed as the graphene growth is performed relatively fast. Both the details of the growth of the active edges and the graphene registry and edge energies are discussed in the following paragraphs.

7.1.2 Growth mode

The image sequence in Figure 7.1 reveals a non-trivial mechanism of graphene growth. Instead of the growth by kink-creation and -advancement observed in the graphene-rhodium system[77], graphene on iridium seems to grow by first creating ‘fingers’ at the active edge. Subsequently, a stage follows in which the space between these fingers is filled up to finally form a new row of graphene, having the width of one moiré unit.

This growth process is most clearly visible at the lower left edge of the graphene island in Figure 7.1. In the first panel (Figure 7.1a) the entire edge is decorated with ‘fingers’. In the next image, recorded 176 sec later, almost all space between the ‘fingers’ is filled up. However, no moiré pattern is visible in the added graphene. This situation is a rather stable stage, as it takes more than 600 sec before further growth is observed by the appearance of new ‘fingers’. Note, that in the graphene rim at the active edge, the corrugation of the moiré pattern is observed only at the locations where the new ‘fingers’ are present, as indicated by the arrows in Figure 7.1g. On further inspection, we see that the two new maxima of the moiré pattern are already present vaguely in Figure 7.1f, i.e. directly

prior to the introduction of the two new ‘fingers’ from there. So, first the moiré pattern is established in the newly added graphene rim, and then the ‘fingers’ appear where the moiré pattern is complete.

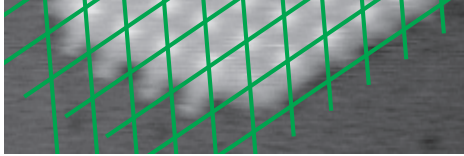
7.2 A geometrical interpretation

The origin of the growth mode and the appearance of the ‘fingers’ is hinted by the precise location where they form. To demonstrate this, a part of the edge of Figure 7.1h is reproduced in Figure 7.2a. The green mash represents the moiré lattice. A quick view at the continuation of this pattern shows that the finger-like protrusions observed during the graphene growth are positioned at specific locations within the moiré unit cell.

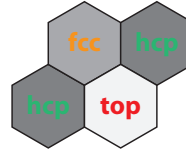
Detailed investigation of the behaviour of a graphene layer on iridium has revealed that graphene is physisorbed with a chemical modulation[70], which is a result of the lattice mismatch between graphene and iridium. This mismatch leads to a corrugation that has a maximum distance between graphene and iridium of 0.362 nm at the so-called top locations in the moiré unit cell. A minimum distance of 0.327 nm and hence the strongest interaction between graphene and iridium is realized at the hcp-locations and an intermediate distance of 0.329 nm is found at the fcc-regions. These specific sites are indicated schematically in the moiré unit cell shown in Figure 7.2b.

When we apply this insight to our observed island edges, Figure 7.2a is translated into the schematic picture shown in Figure 7.2c. After this translation, we recognize that all graphene edges are configured such that they are dominated by sites in which the graphene binds most favourably to the iridium substrate. One possible explanation for the specific ‘finger’ configuration is that it enables the edge to maximally postpone the introduction of expensive top-site regions in the graphene. The price that is paid for this is in the extra edge length, which is apparently still lower than the high price that the top-site regions would cost. On the other hand, the mere fact that the top-site regions are not remaining empty within a full graphene overlayer on Ir(111) shows that the edge energy of the complete circumference of a top-site region is energetically more costly than the top-site region itself. An additional contribution to the energy balance could originate from the energetics of hcp- (and fcc-) edges with respect to top-site edges. We speculate that the differences in coordination to the substrate could lead to differences in rebonding of the dangling bonds of carbon atoms at the graphene periphery to nearby substrate atoms.

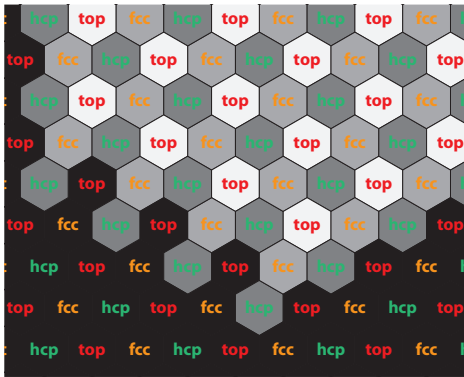
The STM images presented in Figure 7.1 indicate that after the for-



(a)



(b)



(c)

Figure 7.2: (a) A part of the image of the graphene edge shown in Figure 7.1h. The green mesh is superimposed to emphasise the extension of the moiré pattern at its edges. Image size $27 \times 9 \text{ nm}^2$. (b) A schematic representation of a moiré unit cell of graphene on Ir(111). The alignment of the carbon atoms with respect to the iridium lattice is indicated via the ‘top’-, ‘fcc’- and ‘hcp’-labels (see [69] for more details on the labelling). The color of the labels indicates the binding of the graphene with the substrate: the green color stands for a strong binding, the red color for a relatively weak binding and the orange for intermediate binding. (c) A translation of the graphene patch of panel (a) and its edges into the schematic representation presented in panel (b). The preference to have a good alignment and strong interaction at the graphene edge is clearly visible by the presence of ‘hcp’-sites at the graphene island edge.

mation of the ‘fingers’ at an active edge, the growth of graphene continues there by filling up the space between the ‘fingers’. The observation of the filled-up configuration for extended periods of time suggests that this configuration is energetically stable or, at least, metastable. Interestingly, in this configuration, the corrugation that is characteristic for the moiré pattern is not yet developed in the section that the filling-up has added to the graphene layer, even though that section seems to be complete and it has the width of a full moiré unit. We speculate that the graphene in the ‘unfavourable’ regions between the locations where the ‘fingers’ were, exploits its own, lateral deformability, to adjust better to the substrate and thereby locally avoid having carbon atoms in top sites. In this process, it is essential that also the edge of the filled-up region is free to deform. It is precisely this freedom that is necessarily sacrificed when that region protrudes to form the next ‘finger’, thus forcing the now enclosed region to reduce its deformation and tolerate a number of carbon atoms in top sites. These are the high carbon atoms that stand out and together form the protrusions in the moiré pattern.

Finally, the schematical representations in Figures 7.2b and 7.2c clarify why the 6-fold symmetric system of one-atomic layers of both graphene and iridium has broken into a 3-fold symmetric system. The two types of edges at the graphene perimeter, characterised by a difference in edge energy, leads to a breaking of the 6-fold symmetry and to a different growth behaviour of these types of edges. In principle, a similar scenario could be envisioned also for the other three edges, with ‘fingers’ growing out and the space in between being filled up in the next stage. But the fcc- and hcp-regions would have to switch roles from one edge type to the other, which, apparently raises the energy barriers for the other edges sufficiently that they don’t exhibit any growth or ‘finger’ formation on the time scale of our experiments.

7.3 Conclusions

We have presented the first observation of the high-temperature growth of graphene in real time at the sub-moiré-unit level. The monitoring of a graphene island by the STM at a temperature of 1180 K, growing from a low flux of carbon atoms, probably originating from segregation of dissolved carbon, enabled us to follow the growth of this island ‘in slow motion’. From the observations it can be concluded that the growth only takes place at three of the six edges of the graphene island, which indicates that the iridium-graphene system exhibits a 3-fold symmetry. The growth is char-

acterised by a two-step process: first the edge is covered with finger-like structures that appear on specific positions with respect to the moiré unit cell. Only at the moment, at which such a ‘finger’ starts forming at the edge, the corrugation of the moiré structure becomes visible in the moiré unit, to which the finger is attached. In the next step, the space between the fingers is filled up with graphene, however, no moiré corrugation is visible in this new row of graphene units just added.

The observed growth mechanism is explained by the alignment of the graphene lattice with respect to the underlying Ir(111) surface. The local interaction between graphene and the iridium surface atoms plays a decisive role in the growth of graphene. Both the formation of the ‘fingers’ and the filling up of the regions between them with a graphene layer that initially exhibits no corrugation, are demonstrations of the dominant tendency of the Ir(111)/graphene system to avoid the unfavourable configurations with carbon atoms in top sites with respect to the Ir substrate. This results in peculiar growth dynamics and makes the growth of the two types of graphene edges on Ir(111) strongly non-equivalent.

Chapter 8

Graphene ripening: Ostwald beats Smoluchowski

In order to improve the understanding of the growth process of graphene and to control the nucleation density, we studied the ripening of graphene on iridium *in situ*. We investigated the ripening by imaging it with STM, while heating the surface after exposing it to ethylene at room temperature. In this chapter we concentrate on the surface evolution during a slow temperature ramp between 1000 and 1036 K. In this temperature window, we were able to observe the ripening process and to reveal the underlying mechanisms. These mechanisms are expected to have an influence on the final quality of the graphene nanolayer.

8.1 The live observation of graphene ripening by STM

After exposing the surface to 3 L of ethylene at room temperature, the substrate was heated up in vacuum to a temperature of 1000 K at a rate of 7 K/min. Before further ramping the temperature, the system was allowed to equilibrate at 1000 K for a total time of 20 min. Subsequently, a certain surface area was followed by STM for a long period of 1 hour 54 minutes and 24 seconds, while the temperature was increased to 1036 K. The background pressure remained below 1×10^{-10} mbar during the STM imaging. The measured temperature and pressure are presented in Figure 8.1.

The entire STM image sequence recorded during the experiment can be found as a movie in the electronic Supplementary Material (Movie 1). Two representative frames (frames 42 and 223) are presented in Figure 8.2. During the entire image sequence, an iridium step was kept in view while

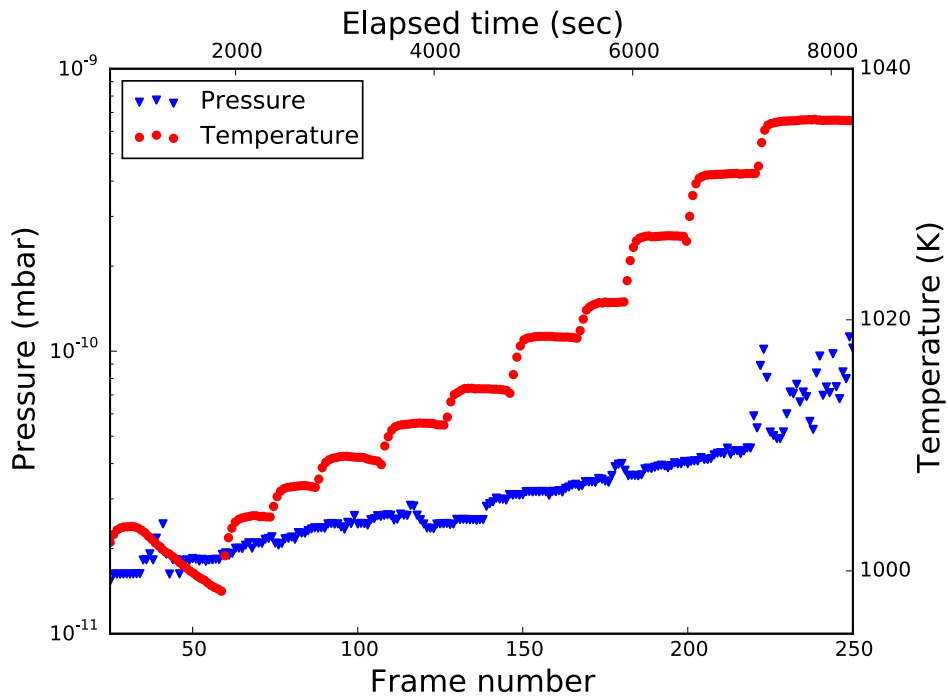


Figure 8.1: Measured pressure and temperature during the experiment. The reader is reminded that the pressure is not corrected and the temperature is measured via a thermocouple welded on the substrate surface. For clarity, both the elapsed time and the STM frame number are shown on the x-axes.

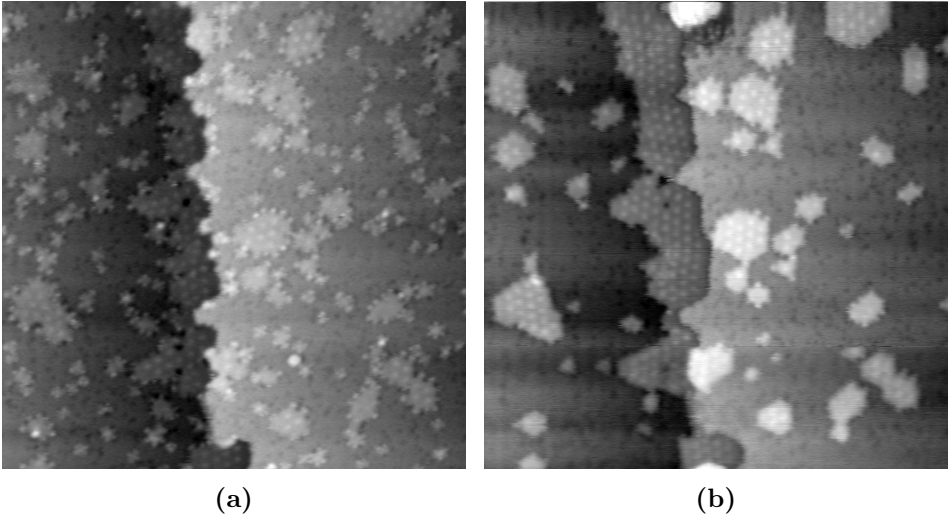


Figure 8.2: Two frames (frames 42 and 223) from an image sequence recorded by STM in which the evolution of graphene islands on Ir(111) was followed while the temperature was increased from 1000 to 1036 K. The images presented here are recorded at a temperature of 1001 and 1036 K respectively. The background pressure remained below 1×10^{-10} mbar during the entire experiment (see Figure 8.1). Image size $106 \times 107 \text{ nm}^2$, z-scale 0.26 nm, sample voltage 2.73 V, tunnelling current 0.1 nA.

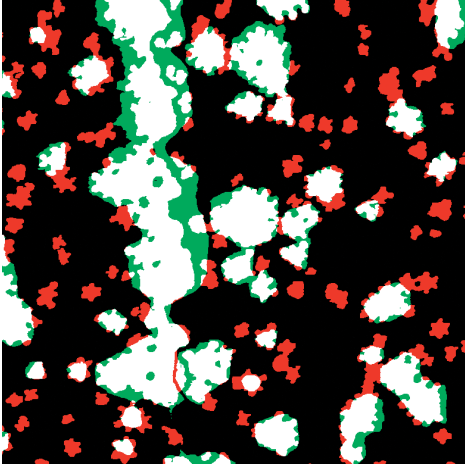


Figure 8.3: Result of subtraction of two frames taken from the STM sequence, frames 50 and 240. For this subtraction, the individual images were first processed to extract the graphene islands and subsequently to convert each of them into a black-and-white image (see Appendix D for details). The white colour in the subtracted image, shown here, presents graphene that was present in both frames; the red colour indicates graphene that was removed between frames 50 and 240; the green colour indicates graphene that was added between frames 50 and 240; the black area indicates iridium that was uncovered in both frames. Image information: The two frames were recorded at temperatures of 1000 K and 1036 K respectively. The time elapsed between the recording of the images was 6303 sec. Image size $71 \times 71 \text{ nm}^2$, sample voltage 2.73 V, tunnelling current 0.1 nA.

the temperature was increased slowly.

To illustrate the evolution of the surface during this experiment, two STM images recorded at the beginning (Frame 50) and at the end of the experiment (Frame 240) were thresholded, aligned and subtracted from each other (see Appendix D for the island extraction algorithm). The result is shown in Figure 8.3. In this image, the red areas depict the graphene that has disappeared and the green areas the graphene that has appeared during the observation. The graphene coverages in these images are 31 ± 1 and 29 ± 1 % respectively, showing that within the error margin the amount of carbon has not changed during the experiment.

8.2 Discussion

Smallest islands disappear At first glance the effect of the slow temperature rise is most evident: all small graphene islands that were present at a temperature of 1000 K are no longer on the surface at 1036 K. Apparently, the smallest graphene nuclei observed at 1000 K are approximately the size of the smallest stable graphene island size at that temperature. At 1036 K, this smallest stable island size has increased and hence the smallest islands present at the lower temperature have become unstable and have disappeared. As a consequence, the average graphene island radius has increased from 1.9 to 3.1 nm. This observation, in combination with an approximately constant graphene coverage, proves that we indeed are in a ripening scenario.

Unstable islands shrink The increase of the smallest stable island size of graphene islands implies that at every stage islands should be present that shrink and eventually disappear. Several occurrences of this mechanism are observed in our experiment, as can be seen in Movie 1. These unstable islands produce a net flux of departing carbon. In addition to this shrinking, the larger islands receive a net flux of arriving carbon, leading to a growth of these islands. Both fluxes are balanced, as the graphene coverage remained constant during the experiment. The process of ripening we observed, is known as Ostwald ripening: the smaller, unstable islands decay and the larger, stable islands grow[74, 78, 79].

No coalescence, no Smoluchowsky ripening When following the entire image sequence (Movie 1) one observes no mobility of any graphene island. The difference-image presented in Figure 8.3 leads to the same observation: even the smallest graphene islands that have remained on the iridium surface have not moved. From this direct observation it can be concluded that the ripening does not take place via Smoluchowsky ripening, i.e. via the coalescence of entire graphene islands.

This conclusion is in contrast to what is suggested in the graphene growth literature. Based on STM observations performed at room temperature after temperature-programmed growth of graphene on iridium, it was suggested in Reference [47] that the ripening should be of the Smoluchowski type. Our direct observations are incompatible with some of the arguments present in Reference [47], which were based on an indirect measurement of the evolution of graphene islands on the Ir(111) substrate.

In the following paragraphs, the precise ripening mechanism and a detailed energy picture will be constructed based on our STM observations.

Diffusion of growth units is not limiting The microscope image presented in Figure 8.2b shows several small graphene islands that have not disappeared yet. As those islands are unstable and hence will shrink, the vicinity of those islands can tell us whether the configuration of the direct surroundings influences these islands. Namely, the local concentration of growth units on the iridium substrate depends a.o. on the curvature of nearby islands and on the competition between the diffusion of growth units over the substrate and the attachment of these units to graphene islands. A relatively low diffusion coefficient results in spatial variations in the concentration of mobile growth units. In such a scenario, a large island (with a large curvature) results in a low local concentration of growth units, hence a small island located close to it will be less stable. On the other hand, similarly, small islands far away from large graphene islands should be more stable.

Inspecting our STM observations with these considerations in mind, we recognise that the smallest islands that are visible in Figure 8.2b are randomly distributed, at locations both close to and far away from the large graphene islands. Apparently, there is no noticeable influence of the presence of large islands and hence we can conclude that the concentration of growth units on the iridium substrate must be nearly uniform, irrespective of the local environment.

In addition to this, when we have a look at the analysis presented in Figure 8.3, we see that the smallest islands that have disappeared (the red-coloured islands) also do not have characteristic surroundings: they are present both close to larger graphene islands and in more dilute areas. All evidence suggests that no direct communication exists between the islands, which leads to the conclusion that the density of the graphene growth units on the bare iridium surface is constant. This insensitivity to the local environment implies that the ripening of graphene is attachment-limited, rather than diffusion-limited. This means that the energy barrier for the attachment of a growth unit to a graphene island is higher than that for the diffusion of the growth unit over the substrate. The attachment being the more difficult step in the ripening process, the two-dimensional ‘gas’ of growth units evens out to a constant background density, from which growth takes place[74, 78, 79]. We can conclude that graphene on iridium evolves via attachment-limited Ostwald ripening.

Ostwald growth and the influence of an iridium step We inspect Figure 8.3 in more detail in order to distinguish how the ripening has changed the island landscape. First of all, most of the small islands, with

diameters up to 2.5 nm are shown in red, indicating that they have disappeared. Islands that were somewhat larger, up to 4 nm diameter, have survived, but with a reduction in size, as indicated by their edges that have more red than green. Islands larger than 4 nm have grown on average, as their mostly green edges tell. These qualitative observations are in accordance with the Ostwald scenario, which should be accompanied by a well-defined hierarchy of dissolution and growth rates of islands as a function of their sizes, with the radii of the smaller ones shrinking and the radii of the larger ones increasing.

The largest island in the images of Figure 8.2 and in the difference image of Figure 8.3 seems to play a somewhat special role. It does not have a compact shape but is stretched out, so that its radius of curvature is very large. As expected for Ostwald ripening, this island has accumulated the largest quantity of graphene over the duration of the temperature ramp experiment. In addition, this island finds itself in a special location, namely attached to a step on the iridium surface. Figure 8.3 shows that the growth of this island has taken place for a large part on one side, namely the side of the graphene island that faces the iridium step. This is supported by Movie 1. A similar observation of enhanced growth of graphene at a metal step has been reported before, during cooling on graphene on Rh(111)[46], where the incorporation mechanism of the graphene involved fluctuations in position of the metal step. We suggest that the energy barrier for incorporating graphene at a metal step is lower than that at a free graphene edge on the iridium substrate.

Island size distributions: no diffusion- but attachment-limited ripening Additional characterization of the ripening of graphene on iridium can be performed using the island size distribution. Island radius distributions extracted from the STM images recorded at different instances (frames 40, 140 and 240) during the ripening experiment are presented in Figure 8.4. At each temperature, in addition to the dashed vertical line that indicates the average island radius, a solid line is shown, which is a guide to the eye for the island radius distribution. This figure shows an overall decrease of the number of islands and an increase of the average island radius as function of temperature; please note that the graphene coverage stayed almost constant during the experiment. More importantly, the island distributions exhibit a significant ‘tail’ to large radii, which might seem more pronounced than expected for Ostwald ripening and might seem to be more fitting for Smoluchowski ripening[80]. However, the distributions that we obtained, can be explained within the framework of Ostwald

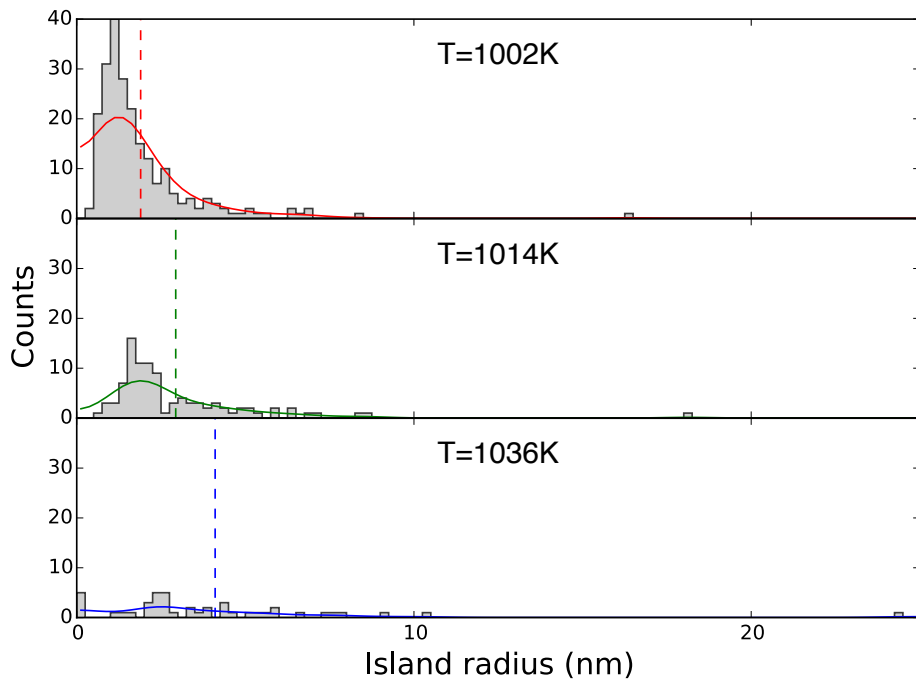


Figure 8.4: Graphene island radius distributions of STM Frames 40, 140 and 240 (top to bottom) recorded at temperatures of 1002, 1014 and 1036 K respectively. The solid lines are guides to the eye for the distributions and the dashed lines indicate the average island radius.

ripening, when we take into account that the shape of the island size distribution is sensitive to both the coverage of the islands and the detailed growth mechanism. First of all, larger coverages, such as e.g. 10%, are known to result in a tail to larger island sizes[80]. The high graphene coverage in our experiment of approximately 30% should therefore result in a significant tail to larger sizes.

In addition, the distribution of island sizes is influenced by the precise growth mechanism. In case of diffusion-limited growth, less islands with larger island sizes will be observed[80]. Consequently, the island size distribution will exhibit a steep drop just above the most frequently occurring island size. In case of attachment-limited growth, the distribution will fall significantly less rapidly. Our distributions and the analysis based on the direct observation of the ripening both are completely in line with the latter picture that describes an attachment-limited ripening scenario.

8.3 Summary and conclusions

The real-time observation of the ripening process of graphene on Ir(111) yielded no signs of any mobility of entire graphene islands. Instead, we observed degradation of smaller islands until they disappeared and growth of larger islands. Our STM observations show that the graphene edges that are directly connected to iridium terrace edges, are preferred growth sites. The spatial distribution of islands on the iridium surface indicates that the density of small, mobile growth units for graphene, is nearly constant over the iridium surface. These findings, in combination with our analysis of the island size distributions at different temperatures, bring us to the conclusion that graphene on iridium ripens via the attachment-limited Ostwald ripening mechanism. We extrapolate our findings by stating that this ripening picture means that, during further growth of graphene by additional carbon deposition at temperatures above 1000 K, nucleation of new graphene islands should not take place.

Chapter 9

Graphene film closure: strain and boundary defects

An important stage of the graphene synthesis process that has a significant impact on the final graphene quality is the closure of the graphene overlayer. In this stage, the individual, still growing graphene domains increasingly touch each other and connect. Depending on their relative alignment, neighbouring domains either merge or domain boundaries are formed between them. Those boundaries can influence the macroscopic properties of the graphene nanolayer, such as charge carrier mobility, yield strength, chemical inertness, etcetera[81, 82]. Here we report a study of graphene film closure, performed using our variable-temperature STM. An Ir(111) surface that was partially pre-covered with graphene was studied while the graphene film was closing. A clear preference of domains to connect to each other in ways that avoid the formation of local defects was observed. In case graphene domains were misaligned with respect to each other, they adjusted themselves by introducing internal deformation. This behaviour was observed through the deformation of the moiré patterns. For the first time, the build-up of strain in graphene was observed.

9.1 Observation of graphene film closure

The findings reported here are originating from two experiments in which we prepared the substrate slightly differently. The general procedure in both experiments was the same. The cleaned Ir(111) substrate was first pre-exposed to ethylene at room temperature. Then, the substrate was heated up in ultrahigh vacuum to a temperature at which practically all carbon had formed graphene. At this temperature, the surface was imaged

by STM while it was further exposed to a low pressure of ethylene. The differences between the two experiments were the amount of ethylene the surface was pre-exposed to at room temperature (0.5 and 3 L) and the precise temperature at which the film-closure experiment was conducted (1067 and 1107 K respectively). Our experiments show that the precise temperature during the experiment did not seem to have a significant influence on the observations. The high-temperature exposure started at a partial pressure of ethylene of approximately 1×10^{-10} mbar. As the graphene growth speed reduced over time, the ethylene pressure was slowly increased to approximately 7×10^{-8} mbar. The temperature was not changed during the experiment and the gas exposure was stopped after the surface was entirely covered with graphene.

Three images extracted from the high-temperature STM observations are shown in Figure 9.1. These images were taken from Movie 2, which can be found in the electronic Supplementary Material. In these images, the orientations of two graphene domains are indicated by the dashed lines. The moiré patterns of the domains have a 4° difference in rotation angle with respect to each other. In combination with the observed lattice distances of the moiré patterns, we can conclude that the two graphene domains are rotated with respect to each other by 0.6° . The two domains are positioned on two adjacent iridium terraces; one iridium step is situated in between the domains. It should be noted that, although the graphene domains look like depressions with respect to the iridium surface, they are actually situated on top of the iridium. The electronic structure of the Ir(111)/graphene system, in combination with the energy dependent LDOS of the STM tip and the applied sample bias voltage, reduces the tunnelling current via the graphene so much that it looks as if the graphene is positioned inside the iridium terraces rather than on top. A close look at other locations on the iridium surface and the application of several sample voltages revealed that the graphene was situated on top of the iridium surface.

The images in Figure 9.1 show how the two slightly misoriented graphene domains grow together to form one closed sheet of graphene. After the two domains have merged, no trace is left of the connection. Imperfections in the connection between the graphene lattices would have shown up in two ways, namely as noticeable imperfections in the moiré pattern and as strong ‘protrusions’ in the STM image due to the electronic structure of the local defects in the graphene lattice[83]. An example of a domain boundary that contains several defects is highlighted by the green arrow in Figure 9.1b.

A second observation that indicates that the graphene lattice does not

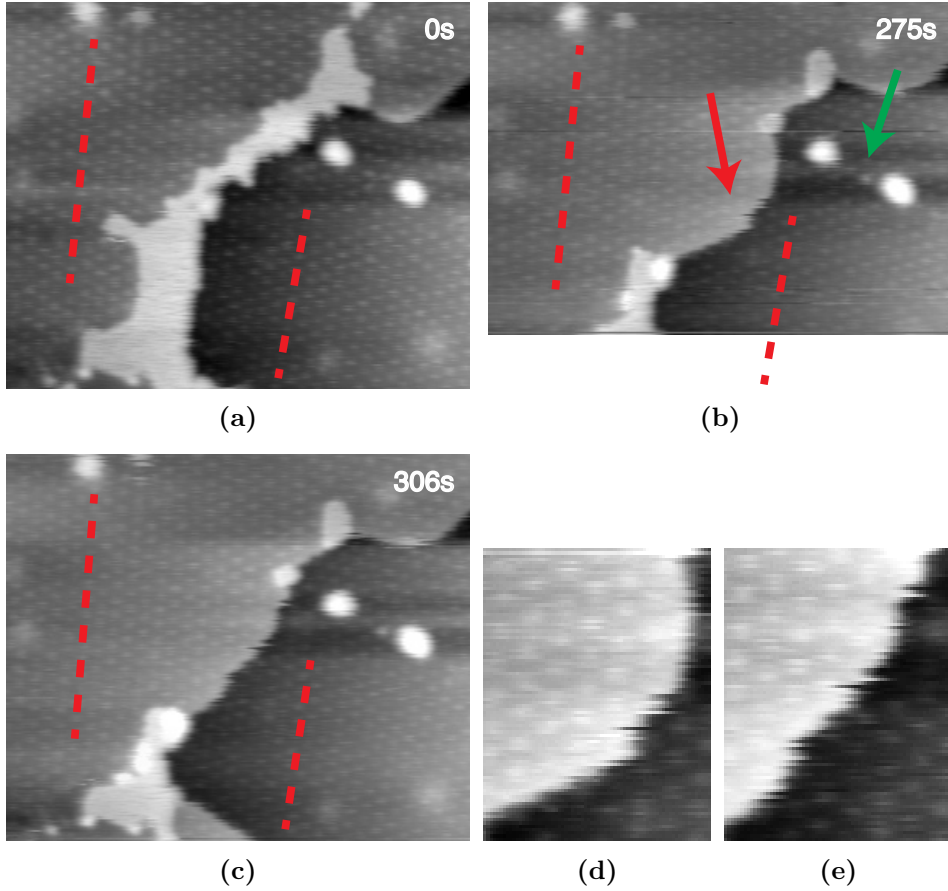


Figure 9.1: (a)-(c) Three frames from an image sequence (frames 213, 219 and 220) in which the closure of the graphene overlayer on top of Ir(111) was followed by STM. The images were recorded at a temperature of 1067 K, while the surface was exposed to an ethylene partial pressure of 7×10^{-8} mbar. The orientation of the moiré pattern in two graphene domains is highlighted by the dashed lines. The red arrow in panel (b) indicates the absence of a domain boundary between the two rotated graphene domains. The green arrow points at the domain boundary between two rotated graphene domains. The elapsed time is indicated in the top right corner of each image. Panels (d) and (e) are close-ups of the same area imaged in panels (b) and (c) and highlight the mobility of the iridium step underneath the graphene, also at the location where the two domains grew together. At the position of the seam between the domains (indicated by the red arrow), no domain boundary can be distinguished. Image size $73 \times 61 \text{ nm}^2$, z-scale 0.27 nm (for Figures (a)-(c)), sample voltage 3.1 V, tunnelling current 0.1 nA

contain defects along the line where the two domains merged, is that of the mobility of the iridium step underneath the graphene. This unhindered mobility suggests the absence of strong, local bonds from the overlayer to the iridium substrate. Such bonds would result in local pinning sites of the iridium to the graphene that reduce the mobility of the iridium surface layer locally. This effect is not observed. An additional advantage of the step mobility is that the line along which the graphene domains have merged, at or close to the step in the iridium substrate, can be inspected in several of the STM images with the step at some distance, thus enabling to view the seam without the complicating influence of the step.

When the orientations of two domains are sufficiently different, they can only connect by introducing a high-angle domain boundary that includes defects in the topology in the form of pentagons and heptagons[83]. The density of these defects along the domain boundary is dependent on the precise mismatch of the domains. An example of such a high-angle domain boundary with defects is indicated in Figure 9.1b by the green arrow.

9.2 Graphene domains locally align by strain

The only way for the differently oriented domains in Figure 9.1 to merge without the introduction of defects in the graphene topology is by tolerating changes in precise bond distances and bond angles, i.e. by introducing strain in the domains. The presence of such long-range deformations is illustrated clearly in Figure 9.2, which displays two STM images of graphene on Ir(111) recorded before and after film closure. For clarity, the individual graphene domains in the two images have been numbered. The temperature of this experiment was 1107 K, higher than that of the experiment of Figure 9.1, but this small difference is expected not to have significant impact on our findings.

The graphene sheet that is shown in Figure 9.2b exhibits moiré patterns that are clearly curved. When we look at the domains before film closure (Figure 9.2a) we can see that they all have different orientations. We find that when the domains come into contact with each other, not only defects are created at certain positions on the domain boundary, but also the graphene domains deform internally, such that the lattices match best with each other. This behaviour can be observed best by following the curving moiré patterns over multiple domains. The red lines in Figure 9.2c show how the internal distortions enable two domains to connect with a minimum of topology errors.

The curved moiré lattices indicate the presence of strain in the graphene.

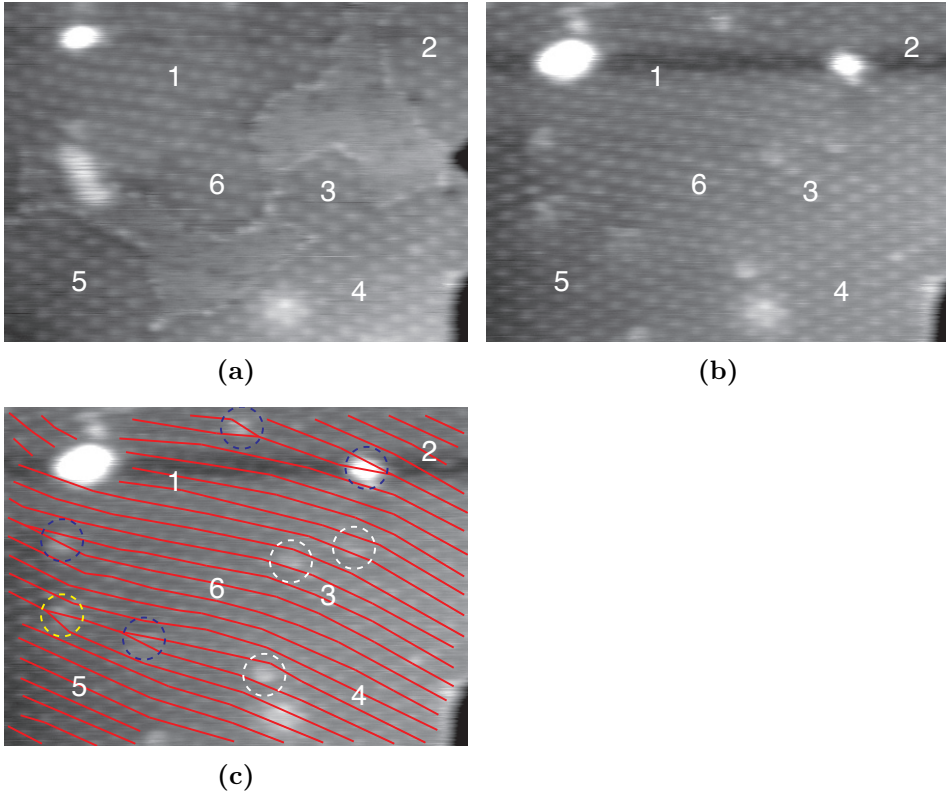


Figure 9.2: (a) and (b) Two STM frames from a movie (frames 139 and 166) in which the closure of the graphene overlayer on Ir(111) was followed by STM. The images were recorded at temperatures of 1099 and 1107 K respectively, while a partial pressure of approximately 7×10^{-8} mbar of ethylene was present. (c) Same image as shown in panel (b), with red lines connecting the maxima in the graphene domains across the image. Here, we have chosen one of the three principal directions of the moiré pattern. Similar sets of lines can be constructed along the other two. The dashed circles indicate point defects in the moiré pattern and are related to point defects in the graphene lattice, as discussed in the main text. Image size $59 \times 43 \text{ nm}^2$, z-scale 0.16 nm, sample voltage 3.4 V, tunnelling current 0.1 nA, time between images: 780 sec.

A close look at the graphene deformation visible in Figures 9.2b and 9.2c shows that some lines are curved such that over a length of 5 moiré units, the lattice has curved over 1 moiré unit. The apparent shift of the moiré pattern over 1 unit means that the graphene lattice has deformed with an amount of 1 graphene lattice constant. Or, over a distance of 5×10 graphene lattice units, the graphene has deformed over 1 lattice unit. This means that a nominal strain of 0.02 was realized in the graphene bonds, which resulted in a deformation of approximately 0.003 nm of each carbon-carbon bond. These values are one order of magnitude lower than experimental and theoretical estimates of the maximum strain graphene can handle, which are in the range of 0.2 – 0.3[84].

The build-up of strain in graphene costs energy. In case the amount of strain needed to align two domains, costs too much energy, the creation of local lattice defects will be more favourable than strain. These defects are observed in Figure 9.2b. The red lines in 9.2c make it easy to follow the moiré maxima over several domains along one of the three principal symmetry axes, and thus recognize the defects in the topology. Every defect, e.g. a pentagon-heptagon pair, in the graphene lattice leads to a single defect in the moiré pattern. In case two adjacent lines merge, a point defect appears. Each point defect is situated at a location where at least in two out of the three symmetry axes, lines merge. All defects are characterised by coloured, dashed circles. The colour of the circle denotes the kind of defect: the yellow colour means the defect shows up in all 3 symmetry directions (1 occurrence), the blue colour indicates the defect shows up in the symmetry direction highlighted by the red lines and another symmetry direction (4 occurrences). The white colour indicates that the defect shows up in the two other symmetry directions that are not highlighted by the red lines (3 occurrences). Our analysis has analogies with the work presented in Reference [83]. In that work, the defects that are labelled in our work by white and blue circles, are studied at the atomic scale. The defects are entitled as edge dislocations containing pentagon-heptagon carbon atom rings. This publication supports our findings. The only defect type that has not been reported before is the yellow-coded defect, which has impact on all three symmetry directions. We suggest that defect is actually a combination of two defects close to each other. As expected, point defects are inevitable in case domains with a significant misalignment merge.

9.3 Conclusions

Summarizing, we conclude that graphene domains growing together on iridium at high temperatures try to avoid the formation of defects in the form of domain boundaries. Most of the relative misalignment of the graphene domains is compensated by the introduction of long-range strain inside the graphene domains. Defects in the graphene lattice are known to influence the properties of graphene, such as the charge carrier mobility and other electronic properties[81, 85]. We expect that the introduction of strain instead of defects has much less impact on these properties, as the graphene lattice is not affected significantly. Also the mechanical strength and the chemical inertness of the graphene may be expected to be more favourable for the strained graphene than for defected graphene. Hence, the process of strain incorporation suppresses the impact of initially misaligned domains on the final quality of the graphene nanolayer.

Chapter 10

High-temperature behaviour of graphene-covered iridium

In the preceding chapters, the nucleation and growth of graphene on the (111) surface of iridium was studied. The results have provided us with detailed insight in graphene synthesis on this substrate. In the present chapter, we continue by focussing on the behaviour of the iridium underneath the graphene at elevated temperatures. We pay special attention to the terrace edges of the iridium surface by, in the first place, looking at the growth of graphene over iridium steps. Second, we focus on the behaviour of iridium steps that are completely covered by graphene. The observations show a dominant role of the moiré pattern that is present in the graphene-iridium system. Third, small fluctuations of the iridium steps were followed. Our findings show that iridium is very mobile underneath the graphene. The iridium steps serve as channels for the transportation of iridium atoms underneath the graphene overlayer.

10.1 Graphene growth over iridium steps

The cleaned Ir(111) substrate was first pre-exposed to 0.5L ethylene at room temperature. Then, the substrate was heated up to a temperature of 1064K. At this temperature the STM imaging was started and one graphene island was kept in view. The system was exposed to a partial pressure of 2×10^{-9} mbar of ethylene while the scanning was continued.

Part of the movie of a growing graphene island on the Ir(111) surface is shown in Figure 10.1, the original movie can be found in the electronic Supplementary Material, Movie 3. In the image sequence shown here, we zoomed in on that part of the island that was growing over an iridium step.

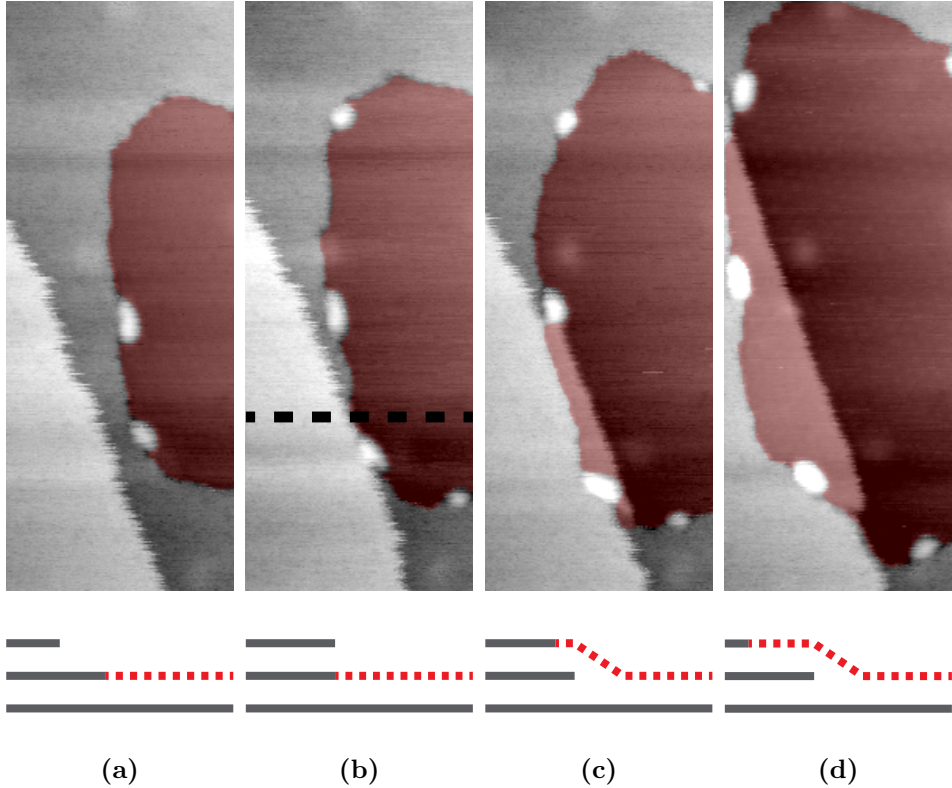


Figure 10.1: Four STM frames from an image sequence (frames 64, 68, 73 and 86) showing the growth of a graphene island on top of Ir(111), followed by STM. The images were recorded at a temperature of 1064 K, while the surface was exposed to an ethylene partial pressure of 2×10^{-9} mbar. Frames (b), (c) and (d) were recorded at times of 62, 155 and 553 sec, relative to frame (a). The red colour highlights the graphene island. For clarity a schematical cross section of the imaged surface is shown below each image. The place where the cross section is taken, is indicated by the dashed line in panel (b). Image size $33 \times 87 \text{ nm}^2$, z-scale 0.30 nm, sample voltage 2.2 V, tunnelling current 0.1 nA.

For clarity, the graphene island is highlighted with a red colour. Based on the full-sized STM images (which can be found in Movie 3), we can state that in this image the graphene is growing inside an iridium terrace. A schematic surface cross section is shown below each of the STM images in Figure 10.1. What the image sequence in Figure 10.1 shows, is that the growth of the graphene proceeds into the iridium terraces by the expulsion of iridium edge atoms. At the same time, the iridium edge underneath the graphene island advances, which indicates that a net transport of atoms from the graphene-iridium interface to other areas on the iridium surface is taking place. The latter observation will be discussed in more detail in Section 10.2.

Here, we first focus on the growth of the graphene over the iridium step. In the specific case that is presented here, graphene is growing ‘upwards’, i.e. graphene climbs on top of the iridium terrace that it was originally level with (see transition from (b) to (c) in Figure 10.1). The process of graphene growing of steps has been reported numerous times in the literature, but in most cases, the growth of the graphene islands over the surface steps is ‘downhill’[83, 86–89]. Here, we observe the opposite direction of growth: from a lower iridium terrace to a higher one, ‘uphill’.

In addition to the observation of graphene over-growing iridium in the ‘uphill’ direction, also the timing of the transition to the next iridium terrace is special. As Figure 10.1 illustrates, it is precisely when the graphene has pushed the iridium terrace edge backward so far that it runs against the next step on the iridium surface (panel (b)), that the graphene continues by growing upwards and ‘invading’ the next iridium terrace level. Apparently, the energy required to deform a double-height step on the iridium exceeds the energy investment required for the graphene to cross the step and the chemical potential of the carbon that is provided by the low pressure of ethylene is sufficient for the latter energy investment.

The growth behaviour of graphene that is presented here, is observed systematically. At this stage, we have not investigated the influence of temperature and pressure on the various growth mechanisms of graphene on iridium. Our findings show that already at a relatively low growth temperature of 1064 K graphene can grow over iridium steps. Apparently, the iridium steps are not limiting the sizes of the graphene islands, which would otherwise have been a concern for large-scale graphene production.

One might wonder about the presence of several ‘particles’ that show up as very high in the images of Figure 10.1. In our experiments, these particles appeared during the growth of graphene, only at places where graphene was growing inside the iridium terrace. The height of these par-

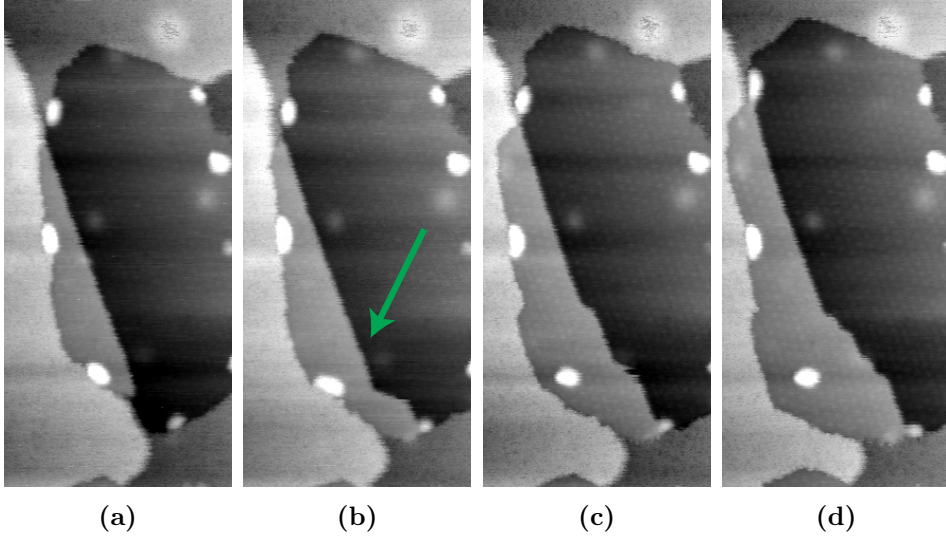


Figure 10.2: Four frames from the same STM sequence as in Figure 10.1 (frames 86, 89, 92 and 96) showing the iridium step mobility underneath graphene. The fluctuating step is indicated by the green arrow in panel (b). The images were recorded at a temperature of 1064 K, while the surface was exposed to an ethylene partial pressure of 2×10^{-9} mbar. Frames (b), (c) and (d) were acquired at times of 91, 183 and 305 sec relative to frame (a). Image size 49×105 nm², z-scale 0.30 nm, sample voltage 2.2 V, tunnelling current 0.1 nA.

ticles is not identical, but they exhibit values comparable to the height (or sometimes twice the height) of an iridium terrace. As long as those particles are situated at a boundary between equally levelled graphene and iridium surfaces, they are mobile, can grow, shrink, merge and disappear. Also, they typically move along with the moving graphene-iridium boundary interface. We observed that sometimes, these particles got trapped inside the graphene, as can be seen clearly in the lower part of the images shown in Figure 10.2. From the behaviour of those particles, we assume that they mainly consist of iridium atoms. We did not observe a significant effect of the presence of those particles on the growth process of the graphene islands.

10.2 Iridium step mobility underneath graphene

The free iridium step on the left side of panel (a) in Figure 10.1 shows a frizzy appearance. This frizziness is characteristic of the rapid step fluctuations that take place on clean metal surfaces. Such fluctuations are due to transport of metal atoms either along the steps or between the steps and the neighbouring terraces [90–93]. Interestingly, when the step is overgrown by graphene, such as is the case for part of the step in panels (c) and 10.1d of Figure 10.1, the frizziness is reduced nearly to zero. In the STM images it looks as if the iridium step that is directly in contact with an edge of the growing graphene island shows no fluctuations at all. Here we concentrate further on the overgrown step in Figure 10.1, which we follow in Figure 10.2 for a total of 305 extra seconds. The images in Figure 10.2 reveal that at 1064 K the iridium underneath the graphene is still mobile: the iridium step that is indicated by the green arrow in Figure 10.2b is changing shape during the experiment. Actually, the step is advancing, which means that over time, iridium is being added to that area of the step.

The images indicate, in particular panels (c) and (d) of Figure 10.2, that the step advancement is initiated from the location where the edge of the graphene island crosses the step on the iridium surface. This part of the step advances most rapidly, while other parts of the step follow with some delay. From a geometrical point of view, it is indeed to be expected that such crossing points provide the locations where iridium atoms can slip in and be incorporated under the graphene most easily. Subsequently, these atoms diffuse along the iridium step underneath the graphene overlayer, possibly with some hindrance by the graphene, until they get incorporated more permanently in the next row of iridium atoms. That even the straight sections of the buried iridium steps are not completely immobile can be seen from the modest, residual frizziness of these edges, visible in Figures 10.1 and 10.2.

Another remarkable observation is that the shape of the advancing iridium step is not straight, but contains ‘macro-kinks’ with a width corresponding to a full unit of the moiré pattern of the graphene overlayer. The movement of these macro-kinks results in the advancement of the buried step. A zoom-in of a location at the step at which multiple macro-kinks are present, is shown in Figure 10.3. In this figure, the contrast has been increased in order to emphasise the relation of the macro-kinks to the moiré pattern. From the zoom-in, we can conclude that the size of each macro-kink is precisely the size of the moiré lattice parameter.

There are two further observations to be taken from Figure 10.3. First, the buried iridium step still exhibits fluctuations in its position, with an

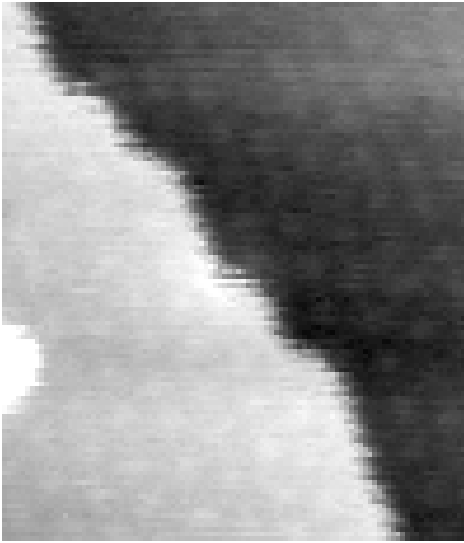


Figure 10.3: A zoom-in of the image presented in Figure 10.2d of a graphene-covered iridium step at 1064 K. The moiré units in the graphene overlayer can be distinguished, as well as the shape of the iridium step beneath the graphene that is roughly following the moiré pattern. Note, that the step also exhibits sub-moiré-unit fluctuations and that the moiré-unit-sized macro-kinks are typically spread out along the step over a distance in the order of a moiré unit. Image size $23 \times 26 \text{ nm}^2$.

amplitude well below the moiré lattice parameter (and also well below the amplitude for the free iridium step). Second, the macro-kinks are not sharp. Instead, each macro-kink is distributed along the length direction of the step over a distance in the order of a full moiré unit. The small-amplitude step fluctuations are also present in the macro-kink portions of the buried step.

The observation that the iridium step tends to follow the moiré lattice tells us that the interaction between the iridium and the graphene is significant under the experimental conditions we exposed our substrate to. Clusters of iridium atoms that are smaller than the moiré unit size appear to be unstable. From this we can conclude that approximately 9×9 iridium atoms have to be added to an existing macro-kink in order to add a new moiré sized iridium unit to that step. Of course, the 81 iridium atoms, required for the addition of a complete moiré unit, cannot be expected to arrive all at once. Intermediate configurations that are less favourable must necessarily be formed first. Our observations that nevertheless, the moiré pattern has a dominant influence on the shape of the buried iridium steps, indicates that the intermediate configurations have significantly higher formation energies. In addition, we remark that it might be that due to the continued ‘supply’ of iridium atoms to the buried step, the concentration of mobile iridium ‘adatoms’ attached to the iridium step is slowly increasing over time and at a well-defined concentration the barrier is overcome for the successful formation of an additional moiré unit to the advancing iridium macro-kink.

The advancement of a buried iridium step in units of the moiré pattern has a strong analogy with the advancement that we have encountered in Chapter 7 of the edges of growing graphene islands. Also for graphene growth, the moiré pattern has a dominating influence, forcing the graphene to grow in units of the moiré lattice. Of course, the energy differences that are at play in both cases are the same. However, an element that brings in a significant difference is the freedom of the graphene to distort significantly at its edges, which leads to the sub-moiré-unit growth ‘strategy’ that we identified for the advancing graphene edges in Chapter 7, for which we find no counterpart here.

One of the remaining questions concerns the origin of the iridium atoms that contribute to the advancement of the steps underneath the graphene. Where do these iridium atoms come from? Why is there net transport of iridium atoms to the buried steps? The answer to these questions is related to the growth of graphene islands into iridium terraces, as observed in Figures 10.1 and 10.2. As we have recognized already, this growth proceeds

by the combination of the advancement of graphene edges and the simultaneous retraction of the iridium steps that they are in direct contact with. This results in a supply of expelled iridium atoms that only ends when the graphene layer is complete. The expelled atoms cannot leave the surface. Nor do we observe their accumulation in iridium adatom islands. Instead, these iridium atoms find their way to the buried iridium steps, which they force to advance in the progress.

10.3 Fluctuations of graphene-covered iridium steps

In the previous section, we reported the observation of mobility of the iridium steps that are covered with graphene. In order to understand the dynamics of the iridium underneath graphene, we studied the high-temperature behaviour of iridium underneath graphene in more detail. Our results are reminiscent of fluctuations of terrace edges on surfaces, recorded at much lower temperature[90–95]. However, in our study, the fluctuations do not take place on the atomic scale, but are characterized by the moiré unit cell, which contains 81 iridium atoms. Apparently, transport of hundreds of mobile iridium atoms takes place underneath the graphene overlayer. Furthermore, we present additional evidence for the nature of the fluctuation as discussed by our group before[95, 96].

10.3.1 Experimental approach

After cleaning and annealing of the iridium surface, graphene was grown by the following method: the iridium substrate was heated up to 1200 K and kept at that temperature for approximately 6000 sec. The background pressure remained below 1×10^{-9} mbar. In this manner, carbon that was remaining in the substrate from previous experiments was used as the main source for the graphene. This procedure resulted in a partial coverage of large (> 100 nm in diameter) graphene flakes. At this high temperature, the substrate was followed by the STM continuously until graphene grew into the field of view of the STM. Subsequently, the focus was set to iridium steps underneath the graphene while the temperature was kept between 1160 and 1210 K. Several scan rotations were applied to characterise the nature of the iridium step fluctuations.

As, in this particular study of fluctuations, the timing of the STM data acquisition is very relevant, we briefly discuss the applied image acquisition procedure. Figure 10.4 indicates the path of the STM tip during the acqui-

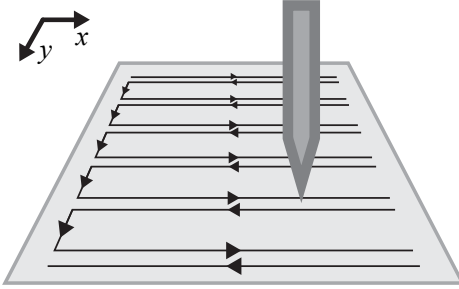


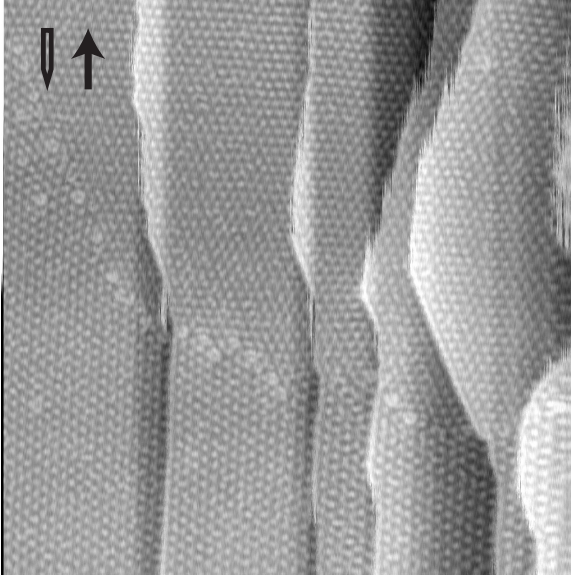
Figure 10.4: Schematics explaining how the STM-tip moves, while the STM-data is recorded. A forward and a backward trace in the x-direction are performed first, then the tip is moved one pixel in the y-direction to record a new line in the x-direction. Both datasets of the forward and backward traces are immediately displayed during the experiment and are stored for later analysis. The fast scan direction is realised by applying a voltage sequence with a triangular wave form to the x-piezo.

sition of one frame. Each such a frame consists of two images: a left-to-right and a right-to-left image. The data for those images are recorded during the forward and backward traces of the STM tip. In the configuration shown in Figure 10.4, the forward-backward direction (typically denoted by the ‘fast scan direction’) is the x-direction and the ‘slow scan direction’ corresponds to the y-direction. The fast scan direction is realised by applying a voltage sequence with a triangular wave form to the x-piezo.

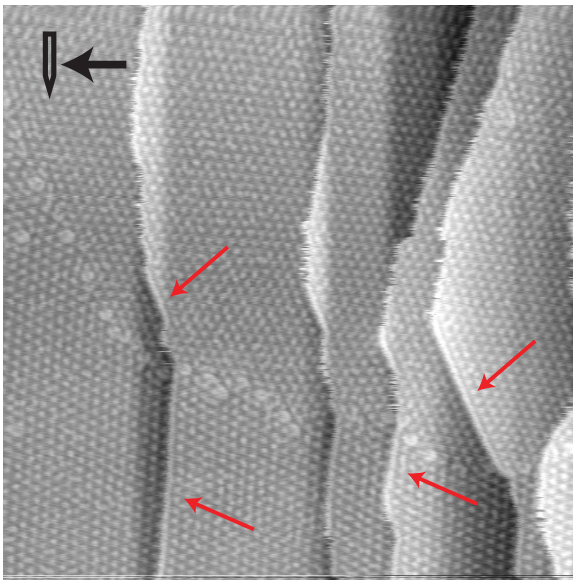
The timing of the STM was as such that the frequency of the triangular wave was 20 Hz. The pixel grid of the recorded image contained 1024×1024 pixels and the acquisition time of one frame was 51.2 sec. These timing settings mean that the time delay between two pixels placed next to each other in the slow scan direction is 50 ms in contrast to $24 \mu\text{s}$ in the fast scan direction.

10.3.2 Orientation dependence of fluctuations of buried iridium steps

A typical STM observation is shown in the two images presented in Figure 10.5. This data shows the same graphene covered iridium surface area, imaged with two different fast scan directions: bottom-to-top (Figure 10.5a) and right-to-left (Figure 10.5b). In these images, a line of defects is visible, which indicates the presence of a domain boundary between two differently oriented graphene domains. Also the moiré patterns indicate that the graphene domain at the top part of the image has a different orientation than



(a)



(b)

Figure 10.5: Two STM images of graphene on Ir(111) recorded successively at 1184K. In Figure (b), the red arrows highlight buried iridium steps that do not exhibit any mobility. The fast scan direction of the images is bottom-to-top for panel (a) and right-to-left for panel (b). Image size $117 \times 117 \text{ nm}^2$, z-scale 0.39 nm, sample voltage 4.5 V, tunnelling current 0.1 nA.

the graphene observed at the lower part of the image.

In both images presented in Figure 10.5 we can see that the mobility of the iridium steps underneath the graphene varies from one location to the other. Some parts of steps are affected by fluctuations, whereas other parts show up completely straight and static. When we compare Figures 10.5a and 10.5b, we see that straight, static parts of iridium steps show up similarly in both images. A few of these step sections are highlighted with red arrows in Figure 10.5b. In contrast, step sections that exhibit fluctuations in the upper panel, exhibit fluctuations in the lower panel as well. The different appearance of these fluctuations is discussed later in this section.

Here, we first focus on the distinction between the static, straight sections and the fluctuating parts of the buried iridium steps. As recognised before, we find that the straight step sections do not align with the lattice directions of the iridium substrate or the graphene overlayer. Instead, they follow directions of the moiré pattern. For all other orientations, the steps exhibit fluctuations. The large difference in fluctuation amplitude between the aligned and misaligned step sections can be understood easily. A misaligned step section necessarily contains macro-kinks, as can be seen in Figure 10.3. For such a step section to fluctuate, it only has to advance or recede the precise locations these existing macro-kinks. On the other hand, the only way for an aligned step section to fluctuate, is to first create new pairs of macro-kinks, which may be expected to require the investment of a sizeable formation energy.

The effect discussed here of the orientation of the buried step with respect to the moiré pattern comes in addition to the reduction in mobility that is introduced by the presence of the graphene overlayer. The latter reduction effect is clearly visible in Figure 10.1, which shows the large fluctuations of the free parts of the iridium step and the strongly reduced fluctuations of the buried step sections.

10.3.3 The ‘width’ of fluctuations

Figure 10.6 displays an STM image of a fluctuating iridium step underneath graphene, at a temperature of 1204 K. The red dashed lines in this figure are guides to the eye that are aligned to the moiré pattern, in order to indicate the size of the fluctuations. This analysis shows that the excursions the steps make in the direction perpendicular to the iridium step, have a typical size equal to size of the moiré unit cell. Again, we see that the influence of the moiré pattern on the behaviour of the iridium underneath the graphene is significant. Apparently, the local variations in interaction

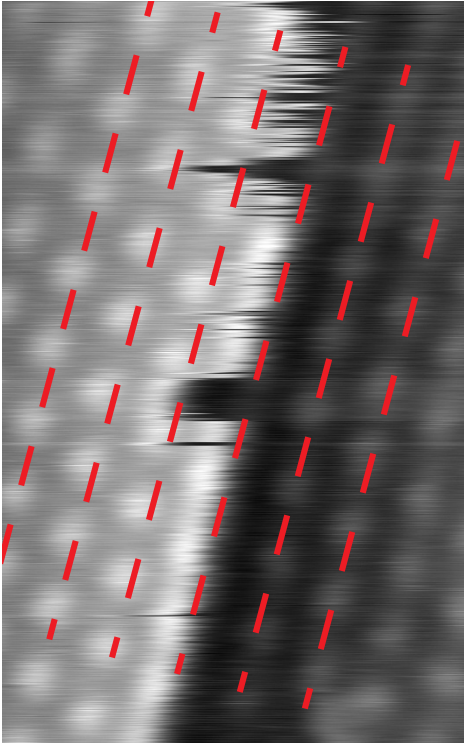


Figure 10.6: Fluctuations of an iridium step underneath graphene, observed by STM at a temperature of 1204 K. The red dashed lines run along the maxima of the moiré pattern (on the lower terrace). Image size $16 \times 26 \text{ nm}^2$, z-scale 0.17 nm, sample voltage 3.9 V, tunnelling current 0.1 nA.

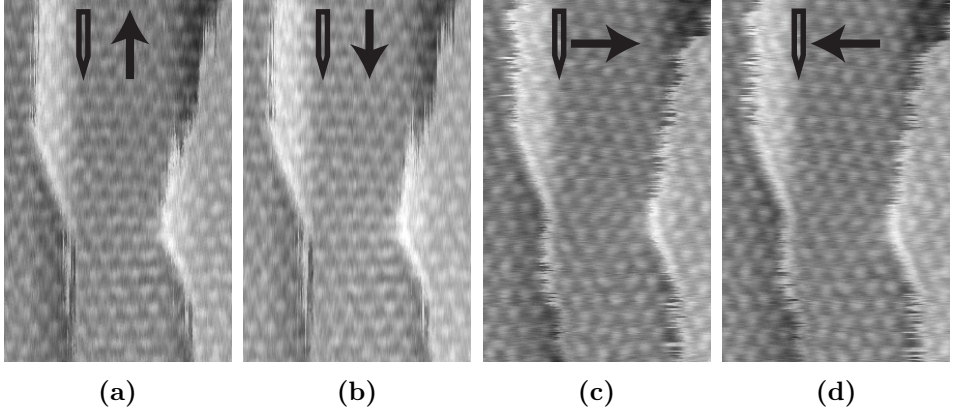


Figure 10.7: Four zoom-ins of STM observations at 1184K of two graphene-covered iridium steps, partially based on the images in Figure 10.5. The fast scan direction is indicated by the arrows. Panels (a) and (b) are composed of the forward (a) and backward (b) traces acquired nearly simultaneously on a subsection of the area also displayed in Figure 10.5a. Similarly, panels (c) and (d) are the forward and reverse traces, corresponding to the same section of Figure 10.5b. Taking into account the timing of the pixels, we see that the macro-kinks can travel readily over distances of 10 nm in 25 ms. Image size $27 \times 43 \text{ nm}^2$, z-scale 0.17 nm, sample voltage 4.5 V, tunnelling current 0.1 nA.

of graphene with the substrate make the iridium fluctuate in between the most stable states, which are a moiré lattice distance apart.

What Figure 10.6 also shows is that in addition to the large units of fluctuation, equal to the full size of a moiré unit cell, the iridium steps also perform rapid fluctuations with a small amplitude. This demonstrates that the preference is not absolute for the step to reside in the positions that are energetically optimal with respect to the moiré pattern; the step is seen to explore small excursions from the optimal positions that are dictated by the moiré pattern. We associate these more frequent, smaller-scale fluctuations with the more typical, atomic-scale step dynamics that is also responsible for the mobility of the uncovered parts of the step.

10.3.4 The ‘length’ of the fluctuations: rapid macro-kink motion

In Section 10.3.2 we have concluded from the orientation dependence of the mobility of graphene-covered steps that this mobility largely reflects

the random-walk motion of existing macro-kinks along the steps. In this section we will use the STM to inspect this motion more directly. Our first step is to compare the STM images in Figure 10.7. In these images, first the bottom-to-top and top-to-bottom traces of one recorded STM frame are shown. The right two panels show the observation made in the subsequently recorded frame. In that frame, the scan direction was rotated 90° , which effectively swaps the fast and slow scan directions. As the triangle frequency used for the fast scan direction was set to 20 Hz, the time between a forward and the subsequent backward trace is 25 ms, the acquisition time between two pixels next to each other in the slow scan direction is 50 ms and the acquisition time between two pixels next to each other in the fast scan direction is $24 \mu\text{s}$.

We first point out that in all four panels of Figure 10.7, two parts of the iridium steps do not exhibit any mobility. From this observation we can conclude that at the timescale of 50 sec (approximately the frame acquisition time) there is no mobility of these part of the iridium steps.

In Figures 10.7c and 10.7d, the mobile sections of the buried iridium steps show up very noisy. Although the noise in panels (c) and (d) is highly correlated, subtle differences can be distinguished already between the forward and reverse scan lines. Between subsequent scan lines within the same panel, the differences are already substantial and excursions over a distance of a full moiré unit can appear or disappear. From this we can conclude that the fluctuations over moiré-unit distances take place on a timescale less than 25 ms

Information on the magnitude, or ‘length’, of the fluctuations can be obtained from the observations shown panels (a) and (b) of Figure 10.7. In these images, the fluctuations appear different from those in panels (c) and (d): they show up as long stripes along the fast scan direction. The length of the stripes can be as large as 10 nm. Most of these stripes are connected at one side to the upper iridium terrace. This behaviour can only be explained by the mechanism in which only individual macro-kinks are moving along the step. The step motion is not caused by the creation of pairs of a macro-kink and an anti-macro-kink. The images in Figure 10.7 indicate that the diffusing macro-kinks can readily traverse distances of 10 nm in 25 ms.

For a macro-kink to move along the step over the minimum distance of a single moiré unit, 81 iridium atoms have to be relocated over significant distances, e.g. over the distance to the next kink[96]. The observed large fluctuations in macro-kink position, of e.g. 10 nm on the timescale of the scan lines of 25 ms, imply an impressive mobility of these iridium atoms

along the graphene-covered steps.

We notice that the fluctuation behaviour of the graphene-covered iridium steps at high temperature is very reminiscent of the fluctuations of steps reported previously for a variety of vicinal metal surfaces at much lower temperatures, such as Cu(1 1 1) and Au(110) [90, 94, 95]. In that work, the atomic-scale mechanisms underlying these fluctuations were derived from the scaling of the step's mean square displacement versus time. In the present study, we have not attempted to quantify the time exponent of the mean square displacement, because it was more difficult than in the clean-surface studies to identify a sufficiently large number of long, fully unpinned step sections and because the extremely high temperatures made it unpractical to reach the low drift rates, required for obtaining meaningful values for the time-dependent step displacements. However, we should expect that the intimate contact between the graphene overlayer and the iridium terraces effectively only leaves a narrow region at the step, where iridium atoms can be mobile. This means that even when iridium atoms on a clean surface would have the possibility to detach from the step and diffuse over the terraces, the presence of the graphene overlayer would force them to return more or less immediately to the step, which would render their diffusion effectively to a one-dimensional random walk along the steps. In such cases, the time exponent of the step fluctuations should naturally adopt a value of $1/4$ [97]. There has been discussion about the nature of short-time correlations in the step motion [94, 96]. The combination of scan directions, across and along the steps, illustrated in Figures 10.5 and 10.7, provides direct evidence for the interpretation advocated in Reference [96] that the short-time correlations originate from rapid back-and-forth motion of existing kinks (in this case macro-kinks) along the steps.

10.4 Summary

We have performed STM studies of the system of graphene on an Ir(111) surface at the high temperatures that are typical for CVD growth of graphene on this substrate. The observations shine new light on the behaviour of the graphene and iridium at temperatures above 1000 K. First, we observe how graphene grows into iridium terraces and we understand how it is forced to 'climb' upwards one iridium plane when the progressing graphene has pushed iridium steps into contact with each other. We find that the iridium steps leave no noticeable signature in the graphene overlayer, which means that the steps have no lasting impact on the graphene quality.

Second, we studied the behaviour of iridium steps underneath graphene.

Advancement of iridium terrace edges underneath graphene is observed during graphene growth. The iridium atoms that add to these buried steps originate from the iridium steps that are forced to recede by the advancing graphene edges. Our images suggest that these iridium atoms can easily slip under the graphene at locations where an edge of a graphene island is draped over an iridium step. The observed mobility revealed a dominating influence of the moiré pattern: the shapes of the mobile iridium steps underneath graphene are strongly dominated by the moiré lattice. This goes not only for the preferred orientations of the steps, but also for the preferred locations, which results in macro-kinks with a width of the full moiré unit cell.

In case an iridium step was not aligned with the moiré lattice, strong fluctuations of the step, underneath the graphene, were observed. Our STM images show that they are caused by the rapid motion along the steps of individual, pre-existing macro-kinks. The macro-kinks easily travel over 10 nm in 25 ms, which involves the relocation of hundreds of iridium atoms over several nanometers within milliseconds.

Our high-temperature STM observations have enabled us to acquire direct insight in the complex dynamics of the system of graphene on a metal substrate. These findings help us to develop new and improved recipes for the synthesis of high-quality graphene by chemical vapor deposition.

Appendix C

Image-subtraction procedure

This appendix explains how the difference between two STM images was calculated. The result of this image-subtraction procedure is presented in Figures 6.2, 6.3 and 6.5 A special focus is put on the STM-image alignment. The kind of image alignment that was necessary to obtain a proper subtraction varied between sets of images. This variation was caused by conditions such as imaging stability, that were different in the various experiments.

The procedure was performed such that the pixel-values in the resulting image could be directly related to absolute distances in the z-direction.

C.1 Subtraction procedure used in Figures 6.2 and 6.5

The input for the subtraction procedure was the raw STM-data of two images from one image sequence. The z-values in this STM data were acquired from the 16-bit analog-to-digital converter of the z-channel of the STM.

The following steps were performed subsequently, the software used to perform these steps is indicated between parentheses.

1. Transform the STM data to a 16-bit tif-image. (Python script)
2. Blow-up the colour scale of the images to simplify the image alignment. The change in colour scale was identical for both STM images. (ImageJ)
3. Save the images as 8-bit tif-files. (ImageJ)
4. Align the images (Adobe Photoshop):

- Adjust image position (x,y) and rescale the y-size for Figure 6.2
 - Adjust image position (x,y), rescale the x- and y-size and apply a horizontal stretch for Figure 6.5
5. Save the images as 8-bit tif-files. (Adobe Photoshop)
 6. Crop the images to obtain images with similar dimensions. (ImageJ)
 7. Subtract the images. (ImageJ)
 8. Save the images as 32-bit tif-files. (ImageJ)
 9. Set the colour scale to 255 and apply a blue-to-red colour table. (ImageJ)
 10. Save the image as an 8-bit bmp-file. (ImageJ)

C.2 Subtraction procedure used in Figure 6.3

The image subtraction for Figure 6.3 was slightly different as the STM data contained some noise. This noise was characterised by a single, high frequency. For this reason, FFT-filtering was applied in the WSxM software. First, the STM data was exported to WSxM using the export function that is available in the STM software (LPM Camera software). After this export, the following steps were performed:

1. Apply a global plane subtraction. (WSxM)
2. Apply FFT-filtering of a small region in k-space to remove the noise. (WSxM)
3. Apply a greyscale colour table with proper z-scale. (WSxM)
4. Save the image as an 8-bit bmp. (WSxM)
5. Align the images by adjusting the image position. (Adobe Photoshop)
6. Crop the images to obtain images with similar dimensions. (Adobe Photoshop)
7. Save the images as 8-bit bmp-files
8. Subtract the images. (ImageJ)
9. Save the images as 32-bit tif-files. (ImageJ)

10. Set the colour scale to 156 and apply a blue-to-red colour table. (ImageJ)
11. Save the image as an 8-bit bmp-file. (ImageJ)

Appendix D

Island-extraction algorithm

Some of the analysis reported in this thesis was done using a routine to identify and extract graphene islands from STM data. This appendix describes this procedure.

In most of the images that were analysed, several iridium terraces were present. To optimise the island extraction, these images were analyzed terrace by terrace. The following procedure was applied to every individual terrace, the software used to perform these steps is indicated between parentheses.

1. Export the STM data to WSxM using the export function that is available in the STM software. The image resolution is 1024×1024 pixels. (LPM Camera software)
2. Apply line-by-line flattening. (WSxM)
3. Perform a local plane correction on the iridium terrace. (WSxM)
4. Save the image as bitmap. (WSxM)
5. Blur the image with a blur radius of 2 pixels. (Adobe Photoshop)
6. Adjust the image levels to achieve maximum contrast between graphene islands and the iridium terraces. (Adobe Photoshop)
7. Select the graphene islands using the 'Magic Wand' tool with the non-contiguous-selection setting. (Adobe Photoshop)
8. Colour the selected islands white, colour other iridium terraces in the image black. (Adobe Photoshop)
9. Deselect the islands. (Adobe Photoshop)

10. Reselect the islands by a non-contiguous selection of the bright pixels. (Adobe Photoshop)
11. Invert the selection and colour all selected pixels black. (Adobe Photoshop)
12. Apply a colour threshold at level 128 to obtain a black-and-white image. (Adobe Photoshop)
13. Save image as bitmap. (Adobe Photoshop)

This procedure was repeated for every terrace in the image. The resulting images were added together, which resulted in a black-and-white image with all the graphene islands being white and all the uncovered iridium being black. This image was used as a mask for further graphene island analysis. For example, the graphene coverage and the average height of the islands were calculated via Python scripts that coupled the mask with the original STM data.

Bibliography

- [1] M. Dienwiebel, G. S. Verhoeven, N. Pradeep and J. W. M. Frenken. “Superlubricity of Graphite”. *Physical Review Letters* **92**: (2004). DOI: 10.1103/PhysRevLett.92.126101.
- [2] D. Downson. *History of tribology*. London: Longman, 2nd edition, 1998. ISBN: 978-1-86058-070-3.
- [3] F. Bowden and D. Tabor. “The area of contact between stationary and between moving surfaces”. *Proceedings of the Royal Society of London. Series A* **169**: (1939), pp. 391–413. DOI: <http://dx.doi.org/10.1098/rspa.1939.0005>.
- [4] C. M. Mate, G. M. McClelland, R. Erlandsson and S. Chiang. “Atomic-Scale Friction of a Tungsten Tip on a Graphite Surface”. *Physical Review Letters* **59**: (1987), pp. 1942–1946. DOI: 10.1103/PhysRevLett.59.1942.
- [5] M. Dienwiebel, E. de Kuyper, L. Crama, J. W. M. Frenken, J. Heimberg, D.-J. Spaanderman, D. Glastra van Loon, T. Zijlstra and E. van der Drift. “Design and performance of a high-resolution frictional force microscope with quantitative three-dimensional force sensitivity”. *Review of Scientific Instruments* **76**: (2005). ISSN: 00346748. DOI: 10.1063/1.1889233.
- [6] A. Schirmeisen, L. Jansen and H. Fuchs. “Tip-jump statistics of stick-slip friction”. *Physical Review B* **71**: (2005). ISSN: 1098-0121. DOI: 10.1103/PhysRevB.71.245403.
- [7] J. Sokoloff. “Theory of energy dissipation in sliding crystal surfaces”. *Physical Review B* **42**: (1990), pp. 760–765. DOI: 10.1103/PhysRevB.42.760. arXiv: mat.
- [8] J. Pendry. “Shearing the Vacuum - Quantum Friction”. *Journal of Physics. Condensed Matter* **9**: (1997), pp. 10301–10320. ISSN: 0953-8984. DOI: 10.1088/0953-8984/9/47/001. arXiv: 9707190 [cond-mat].

- [9] L. Prandtl. “Ein Gedankenmodell zur kinetischen Theorie der festen Körper”. *Z. Angew. Math. Mech.* **8**: (1928), pp. 85–106.
- [10] G. Tomlinson. “A molecular theory of friction”. *Philos. Mag.* **7**: (1929), pp. 905–939. DOI: 10.1080/14786440608564819.
- [11] Y. Sang, M. Dubé and M. Grant. “Thermal Effects on Atomic Friction”. *Physical Review Letters* **87**: (2001), pp. 1–4. ISSN: 0031-9007. DOI: 10.1103/PhysRevLett.87.174301.
- [12] P. Steiner, R. Roth, E. Gnecco, A. Baratoff, S. Maier, T. Glatzel and E. Meyer. “Two-dimensional simulation of superlubricity on NaCl and highly oriented pyrolytic graphite”. *Physical Review B* **79**: (2009), pp. 1–9. ISSN: 1098-0121. DOI: 10.1103/PhysRevB.79.045414.
- [13] C. Garrod. *Statistical Mechanics and Thermodynamics*. New York: Oxford University Press, 1995. ISBN: 9780195085235. DOI: 10.1007/BF02189242.
- [14] A. Socoliuc, R. Bennewitz, E. Gnecco and E. Meyer. “Transition from Stick-Slip to Continuous Sliding in Atomic Friction: Entering a New Regime of Ultralow Friction”. *Physical Review Letters* **92**: (2004). DOI: 10.1103/PhysRevLett.92.134301.
- [15] S. Maier, Y. Sang, T. Filleter, M. Grant, R. Bennewitz, E. Gnecco and E. Meyer. “Fluctuations and jump dynamics in atomic friction experiments”. *Physical Review B* **72**: (2005), pp. 1–9. ISSN: 1098-0121. DOI: 10.1103/PhysRevB.72.245418.
- [16] D. Abel, S. Y. Krylov and J. W. M. Frenken. “Evidence for Contact Delocalization in Atomic Scale Friction”. *Physical Review Letters* **99**: (2007). ISSN: 0031-9007. DOI: 10.1103/PhysRevLett.99.166102.
- [17] S. Y. Krylov and J. W. M. Frenken. “Thermal contact delocalization in atomic scale friction: a multitude of friction regimes”. *New Journal of Physics* **9**: (2007), pp. 1–26. DOI: 10.1088/1367-2630/9/10/398.
- [18] M. Hirano, S. Kazumasa, R. Kaneko and Y. Murata. “Observation of Superlubricity by Scanning Tunneling Microscopy”. *Physical Review Letters* **78**: (1997), pp. 1448–1451. DOI: 10.1103/PhysRevLett.78.1448. arXiv: ssoko.
- [19] M. Hirano, K. Shinjo, R. Kaneko and Y. Murata. “Anisotropy of Frictional Forces in Muscovite Mica”. *Physical Review Letters* **67**: (1991), pp. 2642–2646. DOI: 10.1103/PhysRevLett.67.2642.

- [20] S. Y. Krylov, K. Jinesh, H. Valk, M. Dienwiebel and J. W. M. Frenken. “Thermally induced suppression of friction at the atomic scale”. *Physical Review E* **71**: (2005), pp. 1–4. ISSN: 1539-3755. DOI: 10.1103/PhysRevE.71.065101.
- [21] C. Wieferink, P. Krüger and J. Pollmann. “Simulations of friction force microscopy on the KBr(001) surface based on ab initio calculated tip-sample forces”. *Physical Review B* **83**: (2011). ISSN: 1098-0121. DOI: 10.1103/PhysRevB.83.235328.
- [22] B. Persson. “Surface resistivity: theory and applications”. *Surface Science* **269-270**: (1992), pp. 103–112. ISSN: 00396028. DOI: 10.1016/0039-6028(92)91234-3.
- [23] D. C. Senft and G. Ehrlich. “Long Jumps in Surface Diffusion: One-Dimensional Migration of Isolated Adatoms”. *Physical Review Letters* **74**: (1995), pp. 294–297. DOI: 10.1103/PhysRevLett.74.294.
- [24] T. Ala-Nissila and S. Ying. “Universality in diffusion of classical adatoms on surfaces”. *Modern Physics Letters B* **4**: (1990), pp. 1369–1372. DOI: 10.1142/S0217984990001719.
- [25] N. Lorente and H. Ueba. “CO dynamics induced by tunneling electrons: differences on Cu(110) and Ag(110)”. *The European Physical Journal D* **35**: (2005), pp. 341–348. ISSN: 1434-6060. DOI: 10.1140/epjd/e2005-00214-6.
- [26] F. Giessibl and G. Binnig. “Investigation of the (001) cleavage plane of potassium bromide with an atomic force microscope at 4.2 K in ultra-high vacuum”. *Ultramicroscopy* **42-44**: (1992), pp. 281–289. DOI: 10.1016/0304-3991(92)90280-W.
- [27] T. Schimmel, T. Koch, J. Küppers and M. Lux-Steiner. “True atomic resolution under ambient conditions obtained by atomic force microscopy in the contact mode”. *Applied Physics A* **68**: (1999), pp. 399–402. DOI: 10.1007/s003399900943.
- [28] P. Steiner, E. Gnecco, T. Filleter, N. N. Gosvami, S. Maier, E. Meyer and R. Bennewitz. “Atomic Friction Investigations on Ordered Superstructures”. *Tribology Letters* **39**: (2010), pp. 321–327. ISSN: 1023-8883. DOI: 10.1007/s11249-010-9677-2.
- [29] R. Bennewitz. “Friction force microscopy”. *Materials Today* **8**: (2005), pp. 42–48. ISSN: 1369-7021. DOI: 10.1016/S1369-7021(05)00845-X.

- [30] G. S. Verhoeven, M. Dienwiebel and J. W. M. Frenken. “Model calculations of superlubricity of graphite”. *Physical Review B* **70**: (2004). DOI: 10.1103/PhysRevB.70.165418.
- [31] J. W. J. Kerssemakers. *Concept of interactions in local probe microscopy*. PhD thesis, University of Groningen, 1997. ISBN: 903670815X.
- [32] G. Box and M. Muller. “Note on the Generation of Random Normal Deviates”. *The Annals of Mathematical Statistics* **29**: (1958), pp. 610–611.
- [33] K. S. Novoselov, A. K. Geim, S. Mozorov, D. Jiang, Y. Zhang, S. Dubonos, I. Grigorieva and A. Firsov. “Electric Field Effect in Atomically Thin Carbon Films”. *Science* **306**: (2004), pp. 666–669.
- [34] S. Chen, L. Brown, M. Levendorf, W. Cai, S.-Y. Ju, J. Edgeworth, X. Li, C. W. Magnuson, A. Velamakanni, R. D. Piner, J. Kang, J. Park and R. S. Ruoff. “Oxidation Resistance of Graphene-Coated Cu and Cu/Ni Alloy”. *ACS nano* **5**: (2011), pp. 1321–1327. DOI: 10.1021/nm103028d.
- [35] K. S. Novoselov, V. I. Falko, L. Colombo, P. R. Gellert, M. G. Schwab and K. Kim. “A roadmap for graphene”. *Nature* **490**: (2012), pp. 192–200. ISSN: 0028-0836. DOI: 10.1038/nature11458.
- [36] Y. Wu, Y.-m. Lin, A. A. Bol, K. A. Jenkins, F. Xia, D. B. Farmer, Y. Zhu and P. Avouris. “High-frequency, scaled graphene transistors on diamond-like carbon.” *Nature* **472**: (2011), pp. 74–78. ISSN: 1476-4687. DOI: 10.1038/nature09979.
- [37] S.-J. Han, A. V. Garcia, S. Oida, K. A. Jenkins and W. Haensch. “Graphene radio frequency receiver integrated circuit.” *Nature communications* **5**: (2014). ISSN: 2041-1723. DOI: 10.1038/ncomms4086.
- [38] K. S. Novoselov, D Jiang, F Schedin, T. J. Booth, V. V. Khotkevich, S. V. Morozov and A. K. Geim. “Two-dimensional atomic crystals”. *PNAS* **102**: (2005), pp. 10451–10453. DOI: 10.1073/pnas.0502848102.
- [39] L. Tao, J. Lee, M. Holt, H. Chou, S. J. McDonnell, D. A. Ferrer, M. G. Babenco, R. M. Wallace, S. K. Banerjee, R. S. Ruoff and D. Akinwande. “Uniform Wafer-Scale Chemical Vapor Deposition of Graphene on Evaporated Cu (111) Film with Quality Comparable to Exfoliated Monolayer”. *The Journal of Physical Chemistry C* **116**: (2012), pp. 24068–24074. ISSN: 1932-7447. DOI: 10.1021/jp3068848.

- [40] N. Petrone, C. R. Dean, I. Meric, A. M. van der Zande, P. Y. Huang, L. Wang, D. Muller, K. L. Shepard and J. Hone. “Chemical Vapor Deposition-Derived Graphene with Electrical Performance of Exfoliated Graphene”. *Nano letters* **12**: (2012), pp. 2751–2756. ISSN: 1530-6992. DOI: 10.1021/nl204481s.
- [41] Q. Yu, Z. Liu, D. Pandey, D. Wei, T. F. Chung and P. Peng. “Control and characterization of individual grains and grains boundaries in graphene grown by chemical vapour deposition”. *Nature Materials* (2011), pp. 1–7. DOI: 10.1038/NMAT3010.
- [42] W. Regan, S. Aloni, . V. Altoe, . N. Alem, B. Geng, L. Maserati, M. Crommie, F. Wang and A Zettl. “Transfer-Free Batch Fabrication of Large- Area Suspended Graphene Membranes”. *ACS nano* **4**: (2010), pp. 4762–4768. DOI: 10.1021/nn100459u.
- [43] V. E. Calado, G. F. Schneider, A. M. M. G. Theulings, C Dekker, L. M. K. Vandersypen, V. E. Calado, G. F. Schneider, A. M. M. G. Theulings, C Dekker and L. M. K. Vandersypen. “Formation and control of wrinkles in graphene by the wedging transfer method”. *Applied Physics Letters* **101**: (2012). DOI: 10.1063/1.4751982.
- [44] R. E. Honig. *Vapor pressure data for solid and liquid elements*. Vol. 23. RCA Review. RCA Laboratories, 1962.
- [45] L. Kuipers, M. Hoogeman and J. W. M. Frenken. “Jump to contact and neck formation between Pb surfaces and a STM tip”. *Surface Science* **340**: (1995), pp. 231–244. DOI: 10.1016/0039-6028(95)00702-4. arXiv: [reg](https://arxiv.org/abs/1908.07244).
- [46] G. C. Dong, D. W. van Baarle, M. J. Rost and J. W. M. Frenken. “Graphene formation on metal surfaces investigated by in-situ scanning tunneling microscopy”. *New Journal of Physics* **14**: (2012). ISSN: 1367-2630. DOI: 10.1088/1367-2630/14/5/053033.
- [47] J. Coraux, A. T. N’Diaye, M. Engler, C. Busse, D. Wall, N. Buckanie, F.-J. Meyer zu Heringdorf, R. van Gastel, B. Poelsema and T. Michely. “Growth of graphene on Ir(111)”. *New Journal of Physics* **11**: (2009). ISSN: 1367-2630. DOI: 10.1088/1367-2630/11/2/023006.
- [48] E. Loginova, S. Nie, K. Thürmer, N. Bartelt and K. McCarty. “Defects of graphene on Ir(111): Rotational domains and ridges”. *Physical Review B* **80**: (2009). ISSN: 1098-0121. DOI: 10.1103/PhysRevB.80.085430.

- [49] S. Lizzit and A. Baraldi. “High-resolution fast X-ray photoelectron spectroscopy study of ethylene interaction with Ir(111): From chemisorption to dissociation and graphene formation”. *Catalysis Today* **154**: (2010), pp. 68–74. ISSN: 09205861. DOI: 10.1016/j.cattod.2010.05.028.
- [50] M. Hoogeman, D. Glastra Van Loon, R. Loos, H. Ficke, E. de Haas, J. van der Linden, H. Zeijlemaker, L. Kuipers, M. Chang, M. Klik and J. W. M. Frenken. “Design and performance of a programmable-temperature scanning tunneling microscope”. *Review of Scientific Instruments* **69**: (1998), pp. 2072–2080. DOI: 10.1063/1.1148901.
- [51] M. J. Rost. *Energetics of the Au(110)-surface, one reason for many structures*. PhD thesis, Leiden University, 2001. ISBN: 9077017224.
- [52] Newport. <https://www.newport.com>. Visited: 2016-03-28.
- [53] Pfeiffer Vacuum. <https://www.pfeiffer-vacuum.com/en/>. Visited: 2016-03-28.
- [54] Eurotherm by Schneider Electric. <http://www.eurotherm.com>. Visited: 2016-03-28.
- [55] Riber. <http://www.riber.com>. Visited: 2016-03-28.
- [56] Agilent Technologies. <http://www.agilent.com/home>. Visited: 2016-03-28.
- [57] Specs Surface Nano Analysis. <http://www.specs.de/>. Visited: 2016-03-28.
- [58] Sigma Aldrich. <http://www.sigmaaldrich.com/>. Visited: 2016-04-02.
- [59] Messer. <http://www.specialtygases.de>. Visited: 2016-04-02.
- [60] M. Rost, L. Crama, P. Schakel, E. van Tol, C. Overgaw, H. Horst, H. Dekker, B. Okhuijsen, M. Seynen, A. Vijftigschild, P. Han, A. Katan, K. Schoots, R. Schumm, W. van Loo, T. Oosterkamp and J. W. M. Frenken. “Scanning probe microscopes go video rate and beyond”. *Review of Scientific Instruments* **76**: (2005). DOI: 10.1063/1.1915288.
- [61] W. J. Arnoult and R. B. McLellan. “The Solubility of Carbon in Rhodium, Ruthenium, Iridium and Rhenium”. *Scripta Metallurgica* **6**: (1972), pp. 1013–1018.

- [62] K. F. McCarty, P. J. Feibelman, E. Loginova and N. C. Bartelt. “Kinetics and thermodynamics of carbon segregation and graphene growth on Ru (0001)”. *Carbon* **47**: (2009), pp. 1806–1813. ISSN: 0008-6223. DOI: 10.1016/j.carbon.2009.03.004.
- [63] *Surface Preparation Laboratory*. <http://www.sp1.eu>. Visited: 2015-09-22.
- [64] M. Asadian, F. Hajiesmaeilbaigi, N. Mirzaei, H. Saeedi, Y. Khodaei and S. Enayati. “Composition and dissociation processes analysis in crystal growth of Nd:GGG by the Czochralski method”. *Journal of Crystal Growth* **312**: (2010), pp. 1645–1650. ISSN: 00220248. DOI: 10.1016/j.jcrysgro.2010.01.044.
- [65] K. Jacobs, D. Schulz, D. Klimm and S. Ganschow. “Melt growth of ZnO bulk crystals in Ir crucibles”. *Solid State Sciences* **12**: (2010), pp. 307–310. ISSN: 12932558. DOI: 10.1016/j.solidstatesciences.2009.05.015.
- [66] M. Asadian. “The Influence of Atmosphere on Oxides Crystal Growth”. *Modern aspects of bulk crystal and thin film preparation*. Ed. by N. Kolesnikov and E. Barisenko. Rijeka: InTech, 2012. Chap. 6, pp. 123–140. ISBN: 978-953-307-610-2. DOI: 10.5772/1348.
- [67] M. Gsell, P. Jakob and D. Menzel. “Effect of Substrate Strain on Adsorption”. *Science* **280**: (1998), pp. 717–720. DOI: 10.1126/science.280.5364.717.
- [68] A. Janssen and J. Jones. “The sharpening of field emitter tips by ion sputtering”. *Journal of Physics D: Applied Physics* **4**: (1971), pp. 118–123. ISSN: 00223727. DOI: 10.1088/0022-3727/4/1/316.
- [69] A. T. N’Diaye, J. Coraux, T. N. Plasa, C. Busse and T. Michely. “Structure of epitaxial graphene on Ir(111)”. *New Journal of Physics* **10**: (2008). ISSN: 1367-2630. DOI: 10.1088/1367-2630/10/4/043033.
- [70] C. Busse, P. Lazić, R. Djemour, J. Coraux, T. Gerber, N. Atodiresei, V. Caciuc, R. Brako, A. T. N’Diaye, S. Blügel, J. Zegenhagen and T. Michely. “Graphene on Ir(111): Physisorption with Chemical Modulation”. *Physical Review Letters* **107**: (2011). ISSN: 0031-9007. DOI: 10.1103/PhysRevLett.107.036101.
- [71] G. Dong. *Formation of graphene and hexagonal boron nitride on Rh(111) studied by in-situ scanning tunneling microscopy*. PhD thesis, Casimir PhD series, 2012. ISBN: 9789085931386.

- [72] B. Nieuwenhuys, D. Hagen, G. Rovida and G. Somorjai. “LEED, AES and Thermal desorption studies of chemisorbed hydrogen and hydrocarbons on the (111) and stepped [6(111)x(100)] iridium crystal surfaces; comparison with platinum”. *Surface Science* **59**: (1976), pp. 155–176. DOI: 10.1016/0039-6028(76)90298-3.
- [73] P. Lacovig, M. Pozzo, D. Alfè, P. Vilmercati, A. Baraldi and S. Lizzit. “Growth of dome-shaped carbon nanoislands on Ir(111): The intermediate between carbidic clusters and quasi-free-standing graphene”. *Physical Review Letters* **103**: (2009), pp. 14–17. ISSN: 00319007. DOI: 10.1103/PhysRevLett.103.166101.
- [74] M. Zinke-Allmang, L. C. Feldman and M. H. Grabow. “Clustering on surfaces”. *Surface Science Reports* **16**: (1992), pp. 377–463. ISSN: 01675729. DOI: 10.1016/0167-5729(92)90006-w.
- [75] H. Hattab, A. N’Diaye, D. Wall, G. Jnawali, J. Coraux, C. Busse, R. van Gastel, B. Poelsema, T. Michely, F.-J. Meyer zu Heringdorf and M. Horn-von Hoegen. “Growth temperature dependent graphene alignment on Ir(111)”. *Applied Physics Letters* **98**: (2011). ISSN: 00036951. DOI: 10.1063/1.3548546.
- [76] R. van Gastel, A. T. N’Diaye, D. Wall, J. Coraux, C. Busse, N. M. Buckanie, F.-J. Meyer zu Heringdorf, M. Horn von Hoegen, T. Michely and B. Poelsema. “Selecting a single orientation for millimeter sized graphene sheets”. *Applied Physics Letters* **95**: (2009). ISSN: 00036951. DOI: 10.1063/1.3225554.
- [77] G. Dong and J. W. M. Frenken. “Kinetics of graphene formation on Rh(111) investigated by in situ scanning tunneling microscopy.” *ACS nano* **7**: (2013), pp. 7028–7033. ISSN: 1936-086X. DOI: 10.1021/nn402229t.
- [78] W. Ostwald. *Zeitschrift für Physikalische Chemie* **34**: (1900), pp. 495–503.
- [79] G. Rosenfeld, K. Morgenstern, I. Beckmann, W. Wulfhekel, E. Lægsgaard, F. Besenbacher and G. Comsa. “Stability of two-dimensional clusters on crystal surfaces: from Ostwald ripening to single-cluster decay”. *Surface Science* **402-404**: (1998), pp. 401–408. DOI: 10.1016/S0039-6028(98)00024-7.
- [80] M. Zinke-Allmang. “Phase separation on solid surfaces: nucleation, coarsening and coalescence kinetics”. *Thin Solid Films* **346**: (1999), pp. 1–68. ISSN: 00406090. DOI: 10.1016/S0040-6090(98)01479-5.

- [81] A. W. Tsen, L. Brown, M. P. Levendorf, F. Ghahari, P. Y. Huang, R. W. Havener, C. S. Ruiz-Vargas, D. A. Muller, P. Kim and J. Park. “Tailoring Electrical Transport Across Grain Boundaries in Polycrystalline Graphene”. *Science* **336**: (2012), pp. 1143–1146. ISSN: 1095-9203. DOI: 10.1126/science.1218948.
- [82] Z. Fei, A. S. Rodin, W. Gannett, S. Dai, W. Regan, M. Wagner, M. K. Liu, A. S. Mcleod, G. Dominguez, M. Thiemens, A. H. C. Neto, F. Keilmann, A. Zettl, R. Hillenbrand, M. M. Fogler and D. N. Basov. “Electronic and plasmonic phenomena at graphene grain boundaries”. *Nature Nanotechnology* **8**: (2013), pp. 821–825. DOI: 10.1038/NNANO.2013.197.
- [83] J. Coraux, A. T. N’Diaye, C. Busse and T. Michely. “Structural coherency of graphene on Ir(111).” *Nano letters* **8**: (2008), pp. 565–570. ISSN: 1530-6984. DOI: 10.1021/nl10728874.
- [84] G. Cao. “Atomistic Studies of Mechanical Properties of Graphene”. *Polymers* **6**: (2014), pp. 2404–2432. DOI: 10.3390/polym6092404.
- [85] F. Banhart, J. Kotakoski and A. V. Krasheninnikov. “Structural Defects in Graphene”. *ACS nano* **5**: (2011), pp. 26–41. DOI: 10.1021/nn102598m.
- [86] P. W. Sutter, J.-I. Flege and E. a. Sutter. “Epitaxial graphene on ruthenium.” *Nature materials* **7**: (2008), pp. 406–411. ISSN: 1476-1122. DOI: 10.1038/nmat2166.
- [87] X. Li. “Large-Area Synthesis of High-Quality and Uniform Graphene Films on Copper Foils”. *Science* **324**: (2009). DOI: 10.1126/science.1171245.
- [88] H. I. Rasool, E. B. Song, M. Mecklenburg, B. C. Regan, K. L. Wang, B. H. Weiller and J. K. Gimzewski. “Atomic-scale characterization of graphene grown on copper (100) single crystals.” *Journal of the American Chemical Society* **133**: (2011), pp. 12536–43. ISSN: 1520-5126. DOI: 10.1021/ja200245p.
- [89] S. Nie, A. L. Walter, N. C. Bartelt, E. Starodub, A. Bostwick, E. Rotenberg and K. F. McCarty. “Growth from below: graphene bilayers on Ir(111).” *ACS nano* **5**: (2011), pp. 2298–2306. ISSN: 1936-086X. DOI: 10.1021/nn103582g.
- [90] L. Kuipers, M. Hoogeman and J. W. M. Frenken. “Step dynamics on Au(110) studied with a high-temperature, high-speed scanning tunneling microscope”. *Physical Review Letters* **71**: (1993), pp. 3517–3520. DOI: 10.1103/PhysRevLett.71.3517.

- [91] L. Kuipers, M. Hoogeman, J. W. M. Frenken and H. van Beijeren. “Step and kink dynamics on Au(110) and Pb(111) studied with a high-speed STM”. *Physical Review B* **52**: (1995), pp. 11387–11397. DOI: 10.1103/PhysRevB.52.11387.
- [92] M. Giesen and G. S. Icking-Konert. “Equilibrium fluctuations and decay of step bumps on vicinal Cu(111) surfaces”. *Surface Science* **412/413**: (1998), pp. 645–656. DOI: 10.1016/S0039-6028(98)00499-3.
- [93] M. Giesen, G. S. Icking-Konert, D. Stapel and H. Ibach. “Step fluctuations on Pt(111) surfaces”. *Surface Science* **366**: (1996), pp. 229–238. DOI: 10.1016/0039-6028(96)00823-0.
- [94] M. Giesen-Seibert and H. Ibach. “On the time structure of tunneling images of steps”. *Surface Science* **316**: (1994), pp. 205–222. DOI: 10.1016/0039-6028(94)91141-X.
- [95] M. S. Hoogeman, L. Kuipers, D. C. Schlösser and J. W. M. Frenken. “Direct observation and analysis of kink dynamics”. *Surface Review and Letters* **447**: (2000), pp. 25–38. DOI: 10.1016/S0039-6028(99)01175-9.
- [96] G. S. Verhoeven and J. W. M. Frenken. “The return of the kink”. *Surface Science* **601**: (2007), pp. 13–23. ISSN: 00396028. DOI: 10.1016/j.susc.2006.09.001.
- [97] N. Bartelt, J. Goldberg, T. Einstein and E. D. Williams. “The equilibration of terrace width distributions on stepped surfaces”. *Surface Science* **273**: (1992), pp. 252–260. ISSN: 00396028. DOI: 10.1016/0039-6028(92)90290-M.

Summary

On the origins of friction

The friction behaviour of an interface between two macroscopic bodies that are pressed against each other, is determined by the collective behaviour of all the individual micro- and nanocontacts that together define the physical contact between the two bodies. A popular method to study the friction of such a nanocontact experimentally, is the use of a Friction Force Microscope (FFM). The conventional interpretation of the FFM-data relies on a sophisticated version of the Prandtl-Tomlinson model. This classical model is very successful in reproducing many features of atomic-scale friction experiments. However, the one thing that it cannot do is to provide a true physical understanding of the origin of the friction force as it simply assumes instantaneous loss of the excess potential energy in every slip event. More sophisticated models, based on a Langevin equation, introduce an energy dissipation rate, but this quantity is usually employed as a mere fitting parameter, again revealing nothing about the microscopic energy loss mechanisms at play.

In the work described in this PhD thesis, an atomistic approach was taken, starting from an estimate of the dissipation rate that should be expected from a single atom. This estimate, in combination with reasonable assumptions concerning the scaling of dissipation at the nanoscale, allowed us to calculate the friction force experienced by a tip that is moving over a substrate at a certain velocity. Our estimates showed that typical dissipation rates are in the order of 10^{-12} kg/sec. Comparison with values in literature that are obtained by taking the dissipation rate as a fitting parameter in the Langevin equations, yielded a discrepancy as large as six orders of magnitude. The origin of this discrepancy was found to hide in the choice for the mass of the tip apex that is deformed significantly during the stick phase of the characteristic stick-slip motion that results in a friction force. We argued that this mass corresponds to a very modest number of atoms that is associated with the very end of the tip apex, twelve orders

of magnitude smaller than the mass of the entire tip plus cantilever that may follow the motion of the apex, but always with a significant delay. The experimentally found value for the effective spring constant agrees with our picture of a very small, flexible and dynamic mass. Due to this small mass, the tip apex acquires extremely high velocities, which enables the tip apex to dissipate the released slip energies with extreme efficiency. Our findings are in agreement with the observed atomic-scale stick-slip behaviour in many experiments, that can only be described by an approximately critically damped motion.

In order to test the validity of our arguments, we constructed a two-mass-two-spring model as a more refined description of the FFM experiment with a flexible tip, dragged over an atomically corrugated surface. In accordance with the ideas summarized above, we associated a very small dynamic mass with the tip apex. The numerical calculations resulted in friction force maps that showed a surprisingly limited regime of tip configurations for which atomic periodicities were observed clearly. This regime was characterised by a specific ratio between the number of atoms present in the tip-surface contact and the number of atoms in the dynamic mass. Based on this ratio, the situations of critically damped, underdamped and overdamped motion could be coupled directly to the tip apex geometry. Additionally, the numerical model allowed us to study various aspects of the experiments done with the FFM. Typical observations of the lateral deflection of the cantilever and determined Q-factors could be reproduced and explained, which should be regarded as new insight into the origin of friction, introduced by our approach.

Based on our theoretical model of a friction contact and on the calculation results, a friction ‘phase’ diagram was constructed. We conclude that most tips used in AFM- and FFM-experiments have geometries that make the tip apex naturally critically damped, which explains why regular stick-slip motion is readily observed. Deliberate construction of asperities with a geometry that would lead to low-friction contacts, may provide a way to even tune the friction of macroscopic surfaces.

Graphene growth on Ir(111)

To improve the quality of synthesized graphene, and to improve our understanding of nanolayer growth, the growth of graphene on Ir(111) was studied in real time by a Scanning Tunneling Microscope (STM). As the synthesis of graphene on Ir(111) requires a substrate temperature of more than 950 K, a variable temperature STM (VT-STM) was used. With this

apparatus, the nucleation, ripening and growth of graphene could be studied while the temperature was being changed deliberately.

First, the evolution of the Ir(111) surface was studied after exposure to ethylene. While the temperature was increased from room temperature up to approximately 1000 K, the substrate was followed by the STM. Several structural rearrangements were observed, after which the adsorbate layer finally converted into graphene at a temperature of 967 K. Further annealing to approximately 1000 K led to an iridium surface only decorated with structures containing moiré-patterns. The moiré patterns indicated that, at 1000 K, most graphene islands were perfectly aligned with the substrate, and that half moiré units of graphene were the smallest stable configuration of graphene at a temperature close to its nucleation temperature.

In addition, the growth of graphene at a temperature of 1180 K was studied at sub-moiré-unit level by the STM. The observations showed that the growth of graphene islands on iridium is characterised by a two-step process: first, the graphene edge is decorated with finger-like structures with the length of an entire moiré unit cell. Second, the space between the fingers is filled up with graphene, at which point the edge has acquired an extra row of moiré unit cells. This growth behaviour showed that the local interaction between graphene and the iridium surface atoms plays a decisive role in the graphene growth process. As a consequence, the two edge types of graphene islands on Ir(111) evolve non-equivalently.

We have also addressed the ripening process of graphene on Ir(111), a subject that had not been reported before in the literature. For this, we have studied the evolution of small graphene islands during a slow temperature ramp between 1000 and 1036 K. Although the average size of the graphene islands increased and the total graphene coverage was constant, no mobility of entire graphene islands was observed. The spatial distribution of graphene islands, in combination with the island size distributions showed that graphene on iridium ripens via the attachment-limited Ostwald ripening mechanism.

When individual islands in the graphene overlayer merge, the risk of the formation of defects at the resulting domain boundaries is very high, especially when islands are misaligned. To investigate this effect for the graphene-Ir(111) system, we studied the closure of the graphene film on iridium at temperatures between 1067 and 1107 K while the surface was exposed to an ethylene partial pressure of 7×10^{-8} mbar. At the point where graphene domains grew together, graphene was found to avoid the formation of boundary defects by the introduction of long-range strain inside the graphene domains. We expect that the introduction of strain has

much less impact on the physical and chemical properties of the graphene layer than series of point defects, such as dangling bonds, 5-rings or 7-rings. Hence, this effect should be regarded as beneficial to the quality of synthesized graphene.

Finally, the behaviour of iridium underneath graphene was studied, again at high temperature. In this context, we observed the growth of graphene over iridium step edges, typically climbing upwards from the lower to the higher terrace. No loss of quality of the graphene layer was observed. We also studied the fluctuations of the iridium steps underneath a graphene overlayer. Advancement of iridium steps buried by graphene was observed, in a way that suggested that iridium atoms can easily slip under the graphene at specific locations. The shape of the mobile iridium steps was strongly dominated by the moiré lattice, as macro-kinks with a width of the full moiré unit cell were observed. In case the iridium was not aligned with the moiré lattice, strong fluctuations of the iridium steps were observed, which involved the relocation of hundreds of iridium atoms over several nanometers within milliseconds.

Samenvatting

Achtergrond

Het werk dat in dit proefschrift staat beschreven, is uitgevoerd in de onderzoeksgroep ‘Grensvlakfysica’ van de Universiteit Leiden. De naam van deze onderzoeksgroep duidt op het studieonderwerp van de grenzen tussen twee media, een vaste stof en vacuüm of een vaste stof en een gas of zelfs een vaste stof en een andere vaste stof. In dit proefschrift is aan deze naam nog een extra dimensie toegevoegd. Schijnbaar staan er twee afzonderlijke onderzoeken beschreven in dit proefschrift: een theoretisch onderzoek naar de oorsprong van wrijving en een experimenteel onderzoek naar de groei van het materiaal grafeen. Echter, het hogere doel van deze onderzoeken is het mogelijk maken van een ontwikkeling op het grensvlak tussen deze twee gebieden: het controleren van wrijving tussen oppervlakken door middel van de toepassing van het materiaal grafeen. Op kleine, haast atomaire schaal is dit experiment al enige jaren geleden succesvol uitgevoerd binnen dezelfde onderzoeksgroep. De uitdaging is om dit experiment te herhalen op de veel grotere schaal van wrijving in de alledaagse praktijk. Hiervoor is het nodig om te onderzoeken hoe wrijving ontstaat en of de wrijvingswetten schaalbaar zijn. Daarnaast is het nodig dat we op grote schaal kwalitatief hoogstaand grafeen kunnen produceren. Kwalitatief hoogwaardig grafeen is daarnaast ook interessant voor een keur aan andere potentiële toepassingen, bijvoorbeeld als materiaal voor elektronische toepassingen, in mikro-elektromechanische systemen (MEMS) of als coating. In het verdere van deze samenvatting worden de twee onderzoeken die in dit proefschrift staan kort verwoord.

Over de oorsprong van wrijving

Als twee objecten over elkaar heen schuiven, vindt de wrijving hiertussen niet plaats over het gehele oppervlak. Het werkelijke contact tussen

deze oppervlakken wordt gevormd door lokale uitsteeksels die het tegenoverliggende object raken, zie Figuur 1.1. Onze onderzoeksstrategie is nu om het gedrag van één zo'n uitsteeksel te onderzoeken. Als we dit gedrag eenmaal kennen, kan in een volgend stadium geprobeerd worden om het gezamenlijke gedrag van een groot aantal uitsteeksels te beschrijven, en langs die weg wrijving zo goed te begrijpen dat we het verschijnsel in de toekomst zelfs kwantitatief kunnen voorspellen. Het gedrag van een individueel uitsteeksel wordt in onze experimenten tot op zekere hoogte nagebootst door middel van een FFM: een wrijvingskrachtmicroscoop. In dit apparaat wordt wrijving onderzocht door een uiterst scherpe naald met een wel gedefinieerde aandrukkracht over een oppervlak te trekken. Als dit wordt gedaan op een schoon kristaloppervlak, blijft het naaldje telkens even steken in de 'kuiltjes' tussen atomen, totdat de trekkracht te groot wordt. Daarna schiet het naaldje, over een atoom heen, naar het volgende dalletje tussen twee atomen. Dit is te zien in Figuur 1.2c, waar het blauwe naaldje over de rode atomen wordt getrokken. Het 'stick-slip' gedrag dat dan ontstaat kan gevolgd worden door de zijdelingse beweging van het licht flexibele naaldje te meten door middel van de reflectie van laserstralen. Zo kan de vervorming en de wrijvingskracht van het naaldje ten opzichte van het kristal gemeten worden. Resultaten van deze experimenten zijn bekend en de interpretatie ervan wordt vaak gedaan in termen van een massa-veersysteem, een standaardsysteem in de natuurkunde. Een dergelijk systeem kan theoretisch beschreven worden door gekoppelde krachtsvergelijkingen, zogenaamde Langevin-vergelijkingen. De afgelopen decennia heeft men hiermee veel experimentele waarnemingen kunnen verklaren, maar zeker niet alle.

In dit onderzoek wordt de huidige interpretatie van het massa-veersysteem op de schop genomen. Door middel van een atomistische aanpak (de afremming die een afzonderlijk atoom ervaart als dat over een oppervlak hobbelt) en enkele eenvoudige aannames over schaling, wordt aangetoond dat de huidige interpretatie van wrijving op atomaire schaal een intrinsieke tegenstelling bevat, waardoor je eigenlijk een wrijvingskracht zou moeten verwachten die wel een miljoen keer zo laag is als de wrijving die we voelen. Dit extreme verschil kan niet weggepoetst worden door aannames aan te passen of 'op te rekken'. Als uitweg uit dit probleem hebben we een nieuw type massa-veersysteem bedacht. Consequent doorredeneren laat zien dat het uiteinde van het naaldje zeer klein is en extreem kleine, snelle bewegingen maakt over de ondergrond. Door zijn superhoge snelheid, kan het wrijvingscontact tussen het puntje van de naald en de ondergrond relatief veel energie (beter gezegd: impuls) dissiperen, hetgeen de wrijvings-

kracht sterk kan verhogen.

Dit model wordt vervolgens uitgebreid gesimuleerd door middel van numerieke berekeningen. Experimentele resultaten kunnen met grote nauwkeurigheid worden gereproduceerd en experimentele waarnemingen die eerst nog moeilijk te verklaren waren, zoals de lengte en duur van slip-bewegingen, zijn nu eenvoudig te duiden.

De wrijvingsinterpretatie en het theoretisch model dat uit dit onderzoek is voortgekomen, maakt het mogelijk om aan de hand van de vorm van het puntje van de naald te voorspellen wat het wrijvingsgedrag van de hele naald is. Hiermee lijkt het nu in principe mogelijk om een oppervlak van tevoren zodanig te ontwerpen, dat het specifiek macroscopisch wrijvingsgedrag vertoont: wrijving of glibberigheid op maat. Ons model geeft ook mogelijke richtingen aan van combinaties van oppervlakken waarbij de onderlinge wrijving volledig zou moeten verdwijnen: wrijvingsloosheid tussen oppervlakken op grote schaal. Het wachten is nu op experimenten die dit kunnen aantonen.

Groei van grafeen op Ir(111)

Grafeen bestaat uit louter koolstofatomen, die in een kippengaasstructuur geordend zijn. De structuur kan ook worden beschouwd als een oneindig netwerk van aan elkaar geschakelde benzeenringen. Dit maakt het materiaal tot een bijzonder systeem: het is een tweedimensionaal kristal.

Na de eerste succesvolle isolatie van dit materiaal en de demonstratie van zijn bijzondere eigenschappen in 2004 door de latere Nobelprijswinnaar Andre Geim, heeft dit materiaal een ware hype veroorzaakt. Grafeen lijkt een waar wondermateriaal te zijn met een groot aantal bijzondere eigenschappen in uiteenlopende richtingen, bijvoorbeeld op elektronisch, mechanisch en chemisch vlak. Toepassingen lijken daarom niet uit te kunnen blijven. De beschikbaarheid van dit materiaal is echter een groot probleem: grafiet kan dienen als bron van grafeen, maar levert uitsluitend kleine stukjes van het materiaal op. Synthetisch geproduceerd grafeen is momenteel nog niet van voldoende kwaliteit om betrouwbaar toegepast te worden. De synthese van grafeen kan alleen ingrijpend worden verbeterd als er veel meer kennis is van de atomaire processen die bij de vorming van grafeen betrokken zijn.

Een populaire manier om grafeen te produceren is de zogenaamde CVD-methode (Chemical Vapor Deposition): een substraat wordt blootgesteld aan een koolstofhoudend gas. Onder de juiste condities (gasdruk, temperatuur) ontleedt het gas op het oppervlak en wordt er grafeen gevormd.

In mijn onderzoek is de groei van grafeen onderzocht op een iridium oppervlak. Om de groei te onderzoeken op atomaire schaal, is er gebruik gemaakt van een STM. Een STM, of rastertunnelmicroscoop, tast een oppervlak op atomaire schaal af met een scherp naaldje en maakt zo een uiterst nauwkeurige, driedimensionale afbeelding van het oppervlak. Omdat het CVD-proces bij grafeen een hoge temperatuur vereist, moet de STM in staat zijn om afbeeldingen te maken op hete oppervlakken. Dit vereist een extreme stabiliteit van de STM met betrekking tot temperatuurveranderingen van het preparaat dat wordt afgebeeld. Het is enkele jaren geleden in Leiden gelukt om zo'n variabele-temperatuur STM (VT-STM) te ontwikkelen. Dit unieke apparaat is in mijn onderzoek gebruikt om de groei van grafeen op iridium 'live' op atomaire schaal te bestuderen.

Als eerste is onderzocht wat de laagste temperatuur is waarop grafeen zich vormt. Dit is gedaan door op kamertemperatuur ethyleenmoleculen te deponeren op het iridium. Tijdens de verhitting van het iridiumsubstraat is het oppervlak gevolgd met de STM tot grafeen zich vormde bij een temperatuur van 967 K. Hierna is de groei van het grafeen op hoge temperatuur (1180 K) bestudeerd. Hierbij is met name gelet op de evolutie van de omtrek van een grafeeneiland en op de superstructuur die in het grafeen zichtbaar is, het zogenaamde moirépatroon. Met de analyse van deze twee eigenschappen zijn de verschillen in de lokale interactie tussen het iridiumsubstraat en de koolstofatomen in het grafeen zichtbaar gemaakt.

Als derde is de rijping van grafeen onderzocht. Wanneer de temperatuur verhoogd wordt van het iridiumoppervlak, terwijl dit oppervlak bedekt is met een groot aantal kleine grafeeneilanden, worden de kleinste eilanden instabiel en verwijnen ze van het oppervlak. Gemiddeld neemt de grootte van de overgebleven grafeeneilanden dan toe, zodat de totale bedekking van het grafeen constant blijft. Dit opgaan van de kleinste eilanden in grote, stabiele eilanden, kan grofweg op twee manieren: óf via samensmelting, óf via het uiteenvallen van de kleinste eilanden in heel kleine eenheden en het aangroeien van deze kleine eenheden aan de grote eilanden. Het eerste fenomeen wordt ook wel Smoluchowski-rijping genoemd en is te herkennen aan mobiliteit van de kleinste eilanden als geheel. Het tweede fenomeen wordt Ostwald-rijping genoemd. In tegenstelling tot conclusies in de literatuur die gebaseerd waren op indirecte bewijzen, is er in ons onderzoek direct bewijs verkregen dat de rijping niet plaats vindt via samensmelting, maar via (zogenaamde aanhechtings-gelimiteerde) Ostwald-rijping.

Wanneer de groei van de grafeenlaag bijna voltooid is, beginnen afzonderlijke grafeeneilanden elkaar te raken. In het geval dat de eilanden niet goed uitglijnd zijn ten opzichte van elkaar, ontstaan er korrelgrenzen.

Onze STM-waarnemingen laten zien dat grafeeneilanden die eigenlijk niet goed met elkaar zijn uitgelijnd, in het proces van samengroeien spontaan vervormen, waardoor het ontstaan van dergelijke korrelgrenzen grotendeels voorkomen wordt. Deze vervorming introduceert uiteraard spanning in de afzonderlijke eilanden. Blijkbaar is het introduceren van deze spanning energetisch voordeliger dan het creëren van korrelgrenzen met roosterdefecten daarin. Alleen bij grotere uitlijnproblemen ontstaan er defecten in de korrelgrenzen.

Als laatste is onderzocht hoe, bij de groeitemperatuur van grafeen, het iridium zich onder het grafeen gedraagt, met name op plekken waar er iridiumstappen aanwezig zijn. Aan de ene kant is waargenomen dat tijdens grafeengroei, het grafeen over stappen heen kan groeien. Voor het eerst laten we op de schaal van de moiré-eenheden zien hoe grafeen een iridiumstap ‘opklimt’. Dit proces veroorzaakt geen defecten in de grafeenlaag, hetgeen gunstig is voor de kwaliteit van het grafeen. Aan de andere kant is waargenomen dat het iridium onder het grafeen mobiel is. Met name op de plek van iridiumstappen onder het grafeen, is te zien dat er transport plaatsvindt van honderden iridiumatomen over afstanden van verscheidene nanometers in enkele milliseconden. Het moirépatroon dat zichtbaar is in het grafeen, heeft een belangrijke invloed op de mobiliteit van het iridium onder het grafeen. Dit geeft opnieuw aan dat de interactie tussen het grafeen en het iridium significant is waardoor de activeringsenergie voor de diffusie van iridiumatomen tussen het iridiumoppervlak en de grafeenlaag duidelijk verhoogd wordt ten opzicht van die voor iridiumatomen over een grafeenvrij iridiumoppervlak.

Al deze waarnemingen geven inzicht in de dynamiek en de relevante energieën die van belang zijn bij de groei van grafeen op iridium. Het hier gepubliceerde onderzoek geeft richtingen aan voor de ontwikkeling van een groeiproces dat zal resulteren in grafeenlagen van superieure kwaliteit.

Acknowledgements

A most remarkable aspect of both research projects that are presented in this thesis, is that the results are the outcome of teamwork. For both projects, I was part of a group of enthusiastic people. All those people had specific qualities that all together made it possible to achieve the results reported here.

A key person in this is my professor: Joost Frenken. Without his inspiring contribution and his creative solutions, the results would have never been like they are. Another person who popped up in about all the activities of my PhD research is Jan Verhoeven. Jan, thank you for the great time you gave me. Your enormous amount of knowledge and experience was invaluable and your presence was always a guarantee for enjoyable moments.

Concerning the research on friction, I'm thankful to Sergey Krylov for his enormous contribution and for the vivid discussions we had. I would like to thank Stefan Beck as the work he did for his Bachelor thesis was of very high quality.

The experimental work on graphene growth was done together with quite a team. First, I am grateful to Guocai Dong, who instructed me patiently on how to operate the variable-temperature STM. Second, the work done together with Richard van Rijn, Gijs Hijmans, Natasja Jovanovic, José Luis Sambricio and Alea Toughza was very inspiring. Third, I will never forget the great help of our fine-mechanical department, the electronic department, the company Leiden Probe Microscopy BV (especially Gertjan van Baarle) and the support by Marcel Hesselberth and Federica Galli.

For the short period I was involved in the experiments on friction, I would like to thank Pavel Antonov and Martin de Wit. I wish them all the best in finishing their PhD.

Ellie, thank you very much for all the administrative work, such as booking flights and hotels.

Als laatste wil ik mijn familie en vooral mijn vriendin hartelijk bedanken

voor alles waarmee ze mij geholpen hebben. Zeker tijdens het schrijven van mijn proefschrift en de afronding van het promotietraject heb jij, Aline, me fantastisch geholpen en veel geduld gehad. Dank je wel!

Curriculum vitae

Dirk van Baarle is geboren in Ridderkerk op 15 april 1986. In 2004 ontving hij zijn gymnasiumdiploma op het Wartburg College, locatie Guido de Brès in Rotterdam. Tijdens zijn gymnasiumopleiding volgde hij het profiel Natuur en Techniek, met als extra vakken Latijn en Biologie. Hierna begon hij met de studie Natuurkunde aan de Universiteit Leiden, alwaar hij afstudeerde in 2011 op het gebied van de experimentele natuurkunde. Zijn bacheloronderzoek vond plaats onder supervisie van prof. dr. ir. T.H. Oosterkamp en resulteerde in een scriptie met als titel ‘Manipulating carbon nanotubes’. In zijn master ‘Experimental Physics’ werden twee onderzoeken uitgevoerd: het eerste had als onderwerp ‘Atomic Crowd Control, investigation of the growth process of graphene and h-BN on Ni(111)’ en werd uitgevoerd onder supervisie van prof. dr. J.W.M. Frenken. Dit onderzoek had als doel om met behulp van een variabele-temperatuur rastertunnelmicroscop (VT-STM) het groeiproces van grafeen en van hexagonaal boron-nitride op nikkel te optimaliseren. Het tweede onderzoek in zijn masterstudie werd uitgevoerd in de onderzoeksgroep van prof. dr. J. Aarts en richtte zich op het overbrengen van grafeen op een elektrisch isolerend oppervlak, om daarna de elektrische eigenschappen van het grafeen te onderzoeken onder invloed van elektromagnetische straling. De scriptie over dit onderzoek heeft als titel ‘Graphene on Strontium Titanate, towards magnetotransport measurements of graphene on SrTiO₃’.

Na zijn afstuderen begon Dirk van Baarle in 2011 zijn promotieonderzoek in de vakgroep Interface Physics van de Universiteit Leiden. Dit onderzoek werd uitgevoerd in het Huygens-Kamerlingh Onnes Laboratorium. Zijn promotor was prof. dr. J.W.M. Frenken. Een groot deel van het onderzoek dat hij in deze periode heeft verricht staat beschreven in dit proefschrift. Tijdens de afronding van zijn promotieonderzoek heeft hij gewerkt op het Advanced Research Center for Nanolithography (ARCNL) in Amsterdam. Aansluitend hierop is hij als Security Analyst gaan werken bij het bedrijf Underwriters Laboratories.

ISBN: 978-90-8593-277-3
Casimir PhD series 2016-33